Synthesis and characterization of ruthenium and rhodium sulfide thin films and nanoparticles

Ndabenhle Mercury Sosibo

Department Of Chemistry

University Of Zululand

Private Bag X1001

KwaDlangezwa

3886

November 2004

Synthesis and characterization of ruthenium and rhodium sulfide thin films and nanoparticles

A dissertation submitted by

Ndabenhle Mercury Sosibo

to the Faculty of Science and Agriculture in fulfilment of the requirements for the award of the degree of

Master of Science

in the Department of Chemistry

University of Zululand

Supervisor: Prof. N. Revaprasadu

Co-supervisor: Dr. D. Compton

November 2004

Declaration

"I declare that ***Synthesis and characterization of ruthenium and rhodium sulfide thin films and nanoparticles*** is my own work, which was conducted in the Department of Chemistry at the University of Zululand and in the Department of Chemistry at the University of Manchester. I declare that all the sources used or quoted have been indicated and acknowledged by means of complete references"

Sosibo, Ndabenhle Mercury

.....

Abstract

The reaction of the metal salt ($MCl_3 \cdot nH_2O$) with the solution mixture of carbon disulfide (CS_2), dialkylamine (R_2NH) and sodium hydroxide (NaOH) yields a dithiocarbamate complex of formulation $[M(S_2CNR_2)_n]$, (M = Ru and Rh; R = alkyl group; n = 2 or 3). In this work, these complexes were synthesized and characterized, using such techniques as thermogravimetric analysis (TGA), infrared (IR), nuclear magnetic resonance (NMR), mass spectroscopy (MS) and elemental analysis.

The complexes were then used as single-source molecular precursors for the synthesis of metal chalcogenide thin films and nanoparticles. The deposition of Rh_2S_3 and RuS_2 thin films was achieved by the decomposition of $[Rh(S_2CNEt_2)_2]$ and $[Ru(S_2CNEt_2)_3]$ dissolved in toluene using aerosol assisted chemical vapour deposition (AACVD) technique.

The precursors gave good yields of high quality materials and pyrolyze cleanly to give the required films at reasonably high growth rates. Shiny, adherent thin films were deposited on glass substrates at 350-450 °C. The thin films were characterized using X-ray diffraction (XRD), UV-Vis absorption, ellipsometry, scanning electron microscopy (SEM) and energy dispersive X-ray analysis (EDAX).

Metal chalcogenide nanoparticles were also synthesized using complexes $[Ru(S_2CNEt_2)_3]$ and $[Rh(S_2CNEt_2)_2]$ as single source molecular precursors. Both TOPO and HDA were used as capping agents for the nanoparticles. Materials of sizes up to 20 nm were

synthesized from the precursors. Characterization of the nanoparticles was done using UV-Vis absorption spectroscopy, TEM and photoluminescence (PL).

Contents

Chapter 2: Basic principles of instrumental techniques

Chapter 4: Synthesis of rhodium and ruthenium sulfide nanoparticles

Chapter 5: Experimental

List of tables

List of figures

Abbreviations and symbols

Chemicals

Et	ethyl group
PGM	platinum group metal
R	alkyl group
Me	methyl group
Hex	n-hexyl group
E	chalcogenide element (S or Se)
^{t}Bu	tert-butyl group
^{i}Pr	isopropyl group
M	transition metal
TOP	tri-*n*-octylphosphine
TOPO	tri-*n*-octylphosphine oxide
MeOH	methanol
EG	ethylene glycol

Techniques and methods

CVD	chemical vapour deposition
AACVD	aerosol assisted chemical vapour deposition
CVT	chemical vapour transport
UV-Vis	ultraviolet-visible
IR	infrared
SEM	scanning electron microscopy
EDAX	energy dispersive X-ray analysis
NMR	nuclear magnetic resonance
XRD	x-ray powder diffraction
TGA	thermogravimetric analysis
MOCVD	metal organic chemical vapour deposition
TEM	transmission electron microscopy

Symbols and constants

k	wave factor
a.u.	arbitrary units
d	diameter
R	radius/ reflectance
ε	dielectric coefficient
m*	effective mass (m_e*: electron; m_h*: hole)
T	temperature
E	energy
E_g	band gap energy
E_p	phonon energy
f	oscillator strength
h	Planck's constant
e	elementary charge
t	time
n	refractive index
N	complex index of reflection
k	coefficient of extinction
α	absorption coefficient
I	intensity
ν	frequency
rf	radiofrequency
λ	wavelength
Δ and Ψ	ellipsometric angles

Acknowledgements

First and foremost I would like to thank God, the Almighty for all his blessings. To Prof. Neerish Revaprasadu, thank you so much for your guidance and supervision of my work. Thank you for your encouragement and support through trying times and thank you for all your time you dedicated to my needs. To Dr. Daven Compton, thank you so much for all your support and your time. It has a been a wonderful pleasure calling on you every time I had a problem because I knew you would see me through, thank you very much Dr. Compton. I would like to thank Prof G.A. Kolawole for his assistance and his unparalleled support. Thank you Prof Kolawole for your invaluable advice and guidance throughout the years.

I would like to thank Prof Paul O'Brien for his invitation to work in his Laboratory in University Of Manchester. That was an eye opener and a great journey of discovery. I'd like to thank Dr. Azad Malik for his supervision of my work in the Lab; to all Prof O'Brien's group thank you guys for your warm hospitality. I would also like to thank Dr. M. Seki at JASCO International for the ellipsometry measurements and Keith Pell (QM) for the high quality SEM and TEM images.

My sincere words of gratitude go to Mintek for their financial support and making sure my stomach never went empty. I also thank the Royal Society/NRF programme for giving me the opportunity to go overseas and do some chemistry.

To mom and dad, Mr. M.E. and Mrs. B.M. Sosibo, thank you for your unequalled support, understanding and allowing me to reach for the stars! To my siblings Sambulo, Sphelele, Nokubonga, Sihle and Nomvume, thank you for your support and love, I will make it up to you someday. Thank you Mrs. B.S. Mohlaka for getting me started a few years back, if it wasn't for you I wouldn't be here today. Your support and motherly advice has kept me going for all these years. To Mrs N.G. Mkhize and family, your support is appreciated.

Thank you very much Justice for your help and proficient advice throughout the duration of my studies. To Phumudzo, my AACVD course master, thanks a lot for your assistance. Best of luck to all of you guys. And also to my goods friends Sibusiso, Kwazi, Xolani and everybody whose names might just take the whole page, thank you guys for keeping me sane over the periods of frustration. Sibusiso thanks for all your time you dedicated to my troubles and you know how much I appreciate that, thank you very much. And to my good friend Puleng, thank you very much for all your assistance during my studies. Thank you to all my colleagues in the department for their friendships and assistance.

This Dissertation Is Dedicated

To My Loving Parents

Mr. M.E. And Mrs. B.M. Sosibo

CHAPTER 1

GENERAL INTRODUCTION

1 Introduction

1.1. Ruthenium and Rhodium Chalcogenides

The platinum group metals (PGMs) are made up of platinum (Pt), palladium (Pd), ruthenium (Ru), rhodium (Rh) and osmium (Os). Of these, platinum and palladium have been mostly widely studied and are commercially very important because of their immediate applications. PGMs generally find applications in automotive, chemical and petroleum industries. Other useful applications have emerged through preparation of novel materials of these metals. These include applications in the electrical and electronic, dental and medical, and jewellery industries.

These metals form a variety of chalcogenides, which are compounds that primarily contain sulphur, selenium, oxygen, tellurium or polonium. Some of these chalcogenides occur naturally. These materials have been studied intensively of late due to their applicability in both materials science and catalysis.[1] Generally the PGMs form chalcogenides of the forms as illustrated below:

- Binary
- Pseudo-binary e.g. $Ru_{1-x}Os_x$ and Ni_xRu_{1-x}
- Ternary, such as spinnels: $M'M_2E_4$ (M' = Mn, Fe, Co; M= Ru, Ir and E=S, Se and Te) and $Tl_2Pt_4E_6$ (E= S, Se and Te); MoRuS and many others.

The metal chalcogenides have been considerably studied when prepared as bulk material and only recently has there been any interest in nanoparticles and thin films of these materials. Several methods have been used to prepare these materials as single crystals

and also as powders. Ruthenium forms dichalcogenides (RuE_2) where E= S, Se or Te and they are generally prepared by heating stochiometric quantities of the elements in evacuated sealed ampoules at elevated temperatures.[2] Bulk RuS_2 has been synthesized using chemical vapour transport (CVT)[3] using interhalogens as transporting agent and has also been prepared using tellurium flux. The use of CVT has been reported using Cl_2/ICl_3 as the transport agent.

RuE_2 have been studied extensively by powder[4] and single crystal[5] X-ray measurements. From these studies it was observed that they adopt pyrite-type (FeS_2) structures, and crystallize in a cubic system. Magnetic measurements show that they are diamagnetic. Optical absorption studies[6], electrical resistivity[7] and Hall Effect measurements[7] have shown that RuE_2 are direct band *n*-type semiconductors. Rhodium unlike ruthenium forms a variety of chalcogenides differing in stoichiometry and structural patterns. Four classes of chalcogenides can be identified RhE_2, Rh_2E_3, Rh_3E_4 and Rh_3E_8

Although these are the most primary compounds, chalcogenides of other stoichiometries have been isolated and they include $Rh_{17}S_{15}$, $RhSe_{2+x}$, RhTe and $RhTe_2$. Bulk materials of rhodium chalcogenides are prepared using CVT employing bromine as a transport agent[8] and also by tellurium flux. Rhodium chalcogenides are usually diamagnetic with a few exceptions, such as Rh_3S_4, which shows temperature-independent paramagnetism.[9] These materials exhibit metallic to semiconducting behaviour[6, 9, 10]. Their structures have been studied by X-ray methods and they exhibit diverse structural preferences. RhS_2 materials exhibit pyrite-type structure, Rh_2E_3 are isomorphous[8] and the metal atoms adopt

octahedral configuration. Rh_3E_8 exists in pyrite structure[11] and crystallizes with rhombohedral symmetry. Rh_3E_4 exits in NiAs structure; the structure of $Rh_{17}S_{15}$ has also been established[12] by single crystal x-ray diffraction method.

1.2. Introduction to nanoparticles

Nanometer-sized materials have received immense interest due to their unique physical and chemical properties. They have a potential to develop as important class of materials for the photonics, electronics and other industries in the 21st century.[13-19] These materials are often referred to as quantum dots, q-particles, nanocrystals or more commonly as nanoparticles. These materials have dimensions ranging between 1-100 nm, with those within 1-20 nm being of more interest. The nanosized materials fall in the intermediate state of matter between molecular and bulk and frequently exhibit unusual properties (both chemical and physical). It is due to this that they obey neither absolute quantum chemistry nor laws of classical physics and have properties that differ markedly from those expected. These materials find applications in various fields such as nano-electronic devices, [20] catalysis, [21] fuel cells, [22] gas storage systems[11] and in semiconductor technology.[13-16]

The unique properties in this size range are due to their high surface to volume ratio and to their reduced size in relation to the excitonic radius of the bulk material. As the particle size is reduced, the ratio of the surface atoms in relation to those in the crystal lattice increases, thereby increasing the significance of the surface in determining the properties of the material. The increase in the band gap of the nanocrystalline material with corresponding reduction in particle size is explained by the phenomenon described as the

"quantum size effect". This effect is as a consequence of the confinement of the charge carriers within the dimensions of the nanocrystals resulting in them being treated quantum mechanically as "particles in a box".

In a molecular solid, the intermolecular interactions are much weaker than the intramolecular bonding energies so the bulk properties of a molecular solid can usually be analyzed as the sum of the individual molecular contributions with small perturbations from the intramolecular forces. Due to the weakness of such interactions they rarely extend beyond their nearest neighbours and the electronic structures of a molecular crystal are usually independent of the size of the crystal.

In this novel state of matter the valence band and conduction band split giving rise to discrete energy levels rather than a continuous band as observed in the bulk material. The proximity of the 'electron and hole' pair in nanosized semiconductors has made it impossible to ignore the Coulombic interaction between the electron and hole and they consequently assume higher state of kinetic energy than the bulk material. Experimentally this increase in energy is observed in the optical spectra, where there is blue shift in the band gap as the particle size decreases. In nanocrystalline semiconductors such as CdSe the presence of an excitonic peak or shoulder is also taken as evidence of quantum confinement.

The size dependency of these materials is due to some factors i.e. (i) the particle size and dispersity; (ii) the structure of the particles; (iii) the surface of the particles; (iv) the shape of the particles and (v) the organization of the particles into nanomaterials.[14]

1.2.1. Optical properties of nanoparticles

1.2.1.1. Optical absorption

The optical absorption spectrum of the nanocrystals can be used to evaluate the quantum size effect (Figure 1.1.)

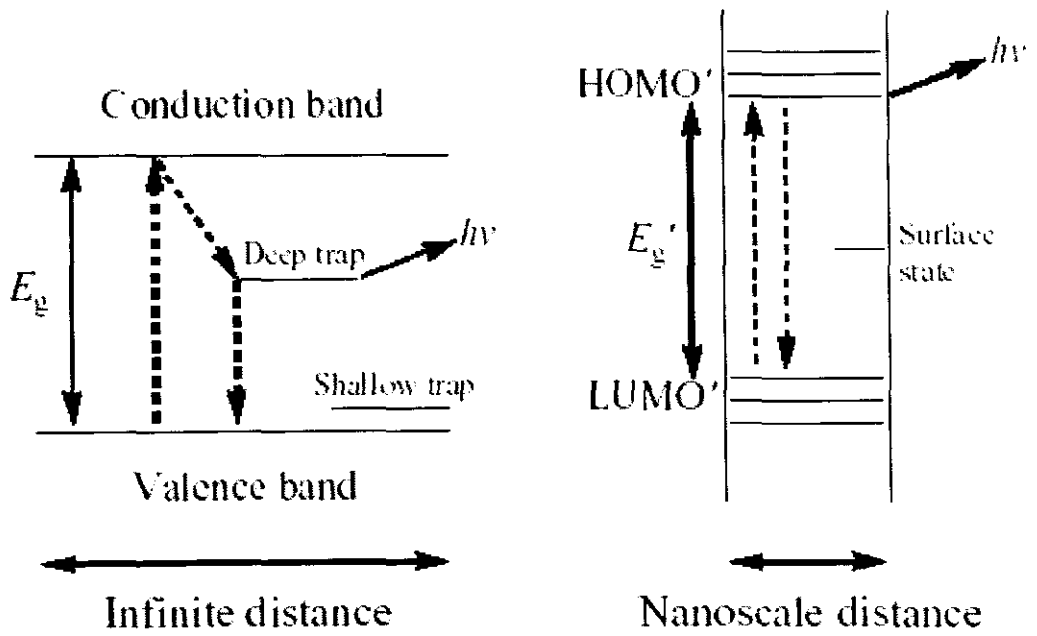

Figure 1.1 *The 'quantum size effect' increases in band gap with decreasing particle sizes.*

For crystalline materials the light absorption is limited to some selection rules. Normally for the excitation to occur, $h\nu \geq$ energy gap. In addition to this selection rule, the wave function, k, should be conserved i.e.

$$k_e + k_{photon} = k'_e \qquad \text{Equation 1.1}$$

k_{photon} is small in comparison with wave vectors of the electron before (k_e) and after excitation (k'_e), therefore equation 1.1 reduces to:

$$k_e = k'_e \qquad \text{Equation 1.2}$$

Nanocrystalline materials which conserve the wave function are called direct band gap materials. Those where the lowest electronic transition, between valence band and conduction band, is formally not allowed (forbidden) are said to be indirect band gap materials and their absorption coefficients are usually very small (Figure 1.2). Phonon assistance is thus required for the indirect band gap transition to occur across the minimum energy gap.

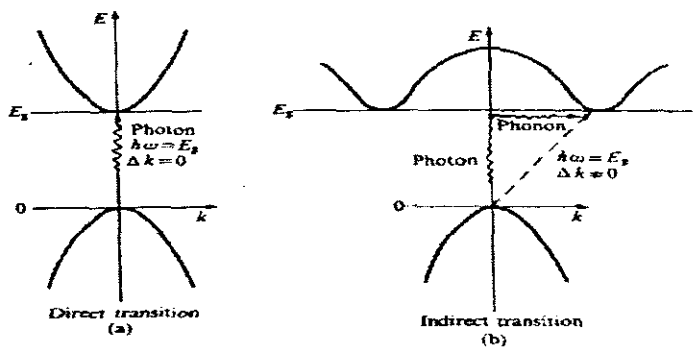

Figure 1.2 *Two types of band gaps (a) direct and (b) indirect transitions.*

The band gap observed for nanocrystalline materials is larger than that reported for the bulk material.[6] This is due to the quantum size effect. Brus, *et al.*[24] considered the Coulomb interactions and polarization terms to explain the energy levels of the first excited state. The approximation of size-dependency of shifts with regard to the bulk band gap is given by:

$$\Delta E = \frac{\eta^2\pi^2}{2R^2}\left[\frac{1}{m_e^*} + \frac{1}{m_h^*}\right] - \frac{1.8\,e^2}{\varepsilon} - \frac{1}{R} \qquad \text{Equation 1.3}$$

Where R = radius of the particles, ε = bulk optical dielectric coefficient, m_e^* = effective mass of the electron and m_h^* = effective mass of the hole. The effective dielectric constants and effective mass are those of macrocrystalline solids and thus could vary for smaller particles. From the approximation it is possible to see the reasons why the first electronic transition increases in energy with a decrease in particle size. Quantum size effects can be explained by many theoretical model calculations.[25-27]

1.2.1.2. Luminescence properties

Apart from a blue shift in the absorption edge, the presence of a peak, most often described as excitonic, begins to resemble a molecular spectrum with discrete energetic transitions rather than a solid with continuous band. Decreasing the size of the particles leads not only to a shift in excitonic peak to higher energy but also to an increase in the

molar absorption. The oscillator strength depends on the radius of the particles and a decrease in the radius of the particles leads to a higher oscillator strength (equation 1.4).

$f/f_{ex} = ¾(a_{ex}/R)^3$ Equation 1.4

where R= particle size, f_{ex} = oscillator strength in bulk material, f = oscillator strength of the particle and a_{ex} = Bohr excitonic radius.[28] These effects are demonstrated in a study of CdS, CdSe and CdTe nanocrystallites with different and well-defined size distributions.

The absorption of electromagnetic radiation by nanocrystalline materials is easy to understand, however the luminescence behaviour of these nanocrystals is somewhat complicated. The luminescence spectra of these materials show a red shift in the emission spectra. Models have been devised to explain this red shift in emission spectra. Brus[27] has explained the features expected in the luminescence spectra of quantum confined nanocrystalline semiconductors. Some focus on luminescence studies on nanodispersed materials have focused on CdS and CdSe.[29]

The sulfur deficiency in CdS is due to the $S^{2-}(V_s^+)$ defects. The V_s^+ is a deep trap and can exothermically extract an electron from the valence band. A hole is left behind by an electron, which localizes away from the V_s^+ site. It's energetically impossible for V_s^+ site to extract another electron from the valence band. The V_s^+ vacancy sets a deep (c. 0.007 eV) trap for a photo-generated electron in the conduction band, which combines forming the V_s^+ state.

Luminescence is attributed to the emission from recombination of a newly created minority carrier with pre-existing majority carrier. In the bulk, the minority carrier is a consequence of impurities or slight non-stoichiometry, and can be either an electron or a hole. In nanoparticles, the minority carrier tends to be the conduction band electron, resulting from a surface S^{2-} vacancy or a Cd^{2+} ad-atom or edge atom. The photo-generated electron is quickly trapped by the V_s^+ to form a V_s^0 site, which can then either be quenched by some surface species or recombine with the nearest pre-existing hole.[29]

1.2.2. Preparation methods for nanoparticles

There are a numerous methods of preparation of semiconductor nanoparticles reported in literature. Among these methods organometallic routes have received more attention[24,30-32]. A synthetic method of choice should offer reasonable control over the properties of the resultant nanostructured material. A brief review on these methods is presented next.

1.2.2.1. Single-source precursor method

This method involves the thermolysis of a single-source molecular precursor, which contains both the metal and the chalcogen of the material to be synthesized. There are a number of advantages of using this method over other precursor methods. The precursors used, which in this case are tris/bis(dithiocarbamato) metal complexes[33], are air stable for a long period of time, reasonably low temperatures are employed in the synthesis and also a single precursor is used which is much convenient compared with the use of two or more precursors. This method of nanoparticle synthesis involves the dispersion of the

single source precursor in TOP, followed by injection into hot TOPO (250 °C). The formation of the nanoparticles is consistent with the La Mer mechanism for colloids.[34] Decomposition of the precursor drives the formation of the nanoparticles with termination of growth occurring when the precursor supply is depleted. After the initial injection there is a rapid burst of nucleation, which is followed by controlled growth of the nuclei by Ostwald ripening. The resultant nanoparticles are passivated by TOPO, preventing agglomeration. The nanoparticles are isolated by a process whereby a non-solvent (methanol) is added to the reaction mixture increasing the average polarity of the solution and consequently decreasing the energy barriers to flocculation. The flocculant precipitate obtained is separated by centrifugation and redispersed in toluene to give an optically clear solution of TOPO capped nanoparticles. Decomposition temperatures, reaction duration and the capping agent all play important role in the final properties of the nanoparticles. Hexadecylamine (HDA), octadecylamine (ODA), alkanethiols and a few others have all been reported as capping agents for nanoparticles.

1.2.2.2. Colloidal route

This route involves controlled precipitation of dilute colloidal solutions. For this method, controlling nucleation and growth yields nanoparticles of reproducible dimensions. The growth process envisages the dissolution and recrystallization of the small (less stable), particles into more stable (larger) crystals. This phenomenon is in agreement with the process known as Ostwald ripening. The ideal mechanism[35] involves very fast nucleation and slow growth, which yields highly monodispersed particles. Solvents with low dielectric constants greatly improve the colloidal stability of the resulting nanoparticles.

Brus[25] reported the synthesis of CdS nanoparticles by the reaction of colloidal solutions of $CdSO_4$ and $(NH_4)_2S$. The size can be controlled by varying the pH, which alters the nucleation kinetics. This method is the most affordable, but comes with some constraints as there is annealing of amorphous particles which tends be a low temperature process producing poorly crystalline materials.

1.2.2.3. Synthesis in confined matrices

Materials which have distinctly defined cavities are employed in the deposition of nanoparticles. These matrices include zeolites,[36] micelles,[37] molecular sieves[37] and polymers.[38] The final properties of the nanoparticles are dependant on the matrix material. Growth of metal chalcogenide on the cavities of zeolites limits the growth, typically to less than 20 nm.

1.2.2.4. Sonochemical route

This method employs the use of ultrasound radiation. The effects of ultrasound radiation has been studied well on the acceleration of chemical reactions[39], and in the generation of materials with unusual properties.[40] High energy sonochemical reactions, without any molecular coupling of the ultrasound with the chemical species, are driven by the formation, growth and collapse of bubbles in a liquid. This acoustic cavitation involves a localized hot spot of temperatures of about 5000 K, pressure of about 800 MPa and cooling rates of about 10^9 K/s due to implosive collapse of bubbles in the liquid.[40] Metal sulfides[41] have been reported prepared this way. Ruthenium sulfide[42] nanoparticles have

been reported, and they were prepared from ruthenium (III) chloride and thiourea as sources.

1.2.2.5. Polyol reduction method

Metal nanoparticles have been largely reported by the use of reduction of their salts to yield nanosized metal powders. A solution of metal salts are reduced using ethylene glycol (EG), diethelene glycol (DEG) and triethylene glycol (TrEG) in a solution containing a stabilizer. In the preparation of Ru(0) nanoparticles[43] polyvinylpyrrolidone (PVP) was employed as the stabilizer.

1.2.3. Applications of nanoparticles

There are a very comprehensive number of applications for nanoparticles and nanotechnology. It is also expected that nanotechnology will be developed at several levels: nanomaterials, devices and systems. The most advanced level at present is nanomaterials level, both in scientific knowledge and in commercial applications. Most applications of these materials demonstrate an exciting area of research for developing new materials of immense technological, catalytic and biological importance.

1.2.3.1. Nanostructured coatings

Thermal spraying of nanomaterials on materials surface is a well defined industrial process. Nanoparticles are often very useful in this regard as they provide the required strength to the surface whilst allowing the surface to function unobstructed. Carbide materials such as M_2C and MC have been used to strengthen steel, which is then used for gears, bearings and shafts in gas turbine engines, because of their good resistance to tempering, wear and rolling fatigue. Nanostructured ceramics have also been used in this regard also due to their wear resistance, chemical resistance and chemical insulating properties.

1.2.3.2. Electronic, optical and magnetic applications

A large number of materials can be used for these purposes. Nanomaterials of insulators, semiconductors, superconductors, metal and alloys, optical and artificially structured materials are all inclusive in this function. Some other applications require the nanoparticles to be dispersed over surfaces, resembling thin films.

1.2.3.3. Microelectronic and optoelectronic applications

Nanoparticles have shown a great potential applicability in electronic systems where quantum size effects may be of advantage. Quantum confinement leads to higher energy level transitions compared with the bulk materials, which is at least a shorter wavelength optical edge. Nanoparticles have been used to produce light emitters of various colours by 'band gap tuning'. This uses the particle size effect rather than the tedious process of synthesizing compound semiconductors. Voltage-controlled, tuneable colour output,

high-conversion efficiency LEDs have been produced by the use the nanoparticles. GaAs and silicon are some of the materials which promise potential applications in fast optical switches and optical fibres on the nonlinear optical behaviour.

1.2.3.4. Gas sensors

There are quite a substantial number of techniques for this purpose and thin film materials have been at the fore front, as the materials of choice. Recent developments also indicate that nanoparticles are equally capable of serving the same purpose. The nanomaterials based gas sensor concept involves measuring the changes in the electrical resistance of a nanocrystalline material when exposed to the active gas, for example CO and H_2. Generally, semiconducting oxides such as SnO_2, ZnO and Fe_2O_3 are used in gas sensing methods. Pd nanoparticles (10-15 nm) have been used as a sensor for hydrogen gas. The response in the nanocrystalline Pd material is faster compared with Pd (micron size) particles, due to smaller diffusion distances. The sensitivity of gas sensors can be increased by doping, usually with platinum group metal catalysts such as Pt, Rh and Pd.

1.2.3.5. Resistors and varistors

Granular conducting nanoparticles embedded on glass exhibit great variability of the electrical conductivity. Varistors are voltage-dependent resistors, characterized by very low resistance at high voltages; they are used for protection of low-power circuits from high-voltage transients. A general method for their preparation involves sintering ceramic materials such as ZnO or SiC with some added minor constituents. Materials with the

sizes of 100 nm or less give good nonlinear electrical characteristics to the varistors and are a good choice thereof.

1.2.3.6. Capacitive materials

Due to the reduction in capacitance caused by the continuing scaling down of Dynamic Random Access Memories (DRAMs), dielectric elements based on nanometer structures have found some interest. These materials with high dielectric constants store more electrical charges in capacitors. One method for increasing the dielectric permittivity is by dispersing conductive particles in a dielectric matrix. Dielectric constants of up to 5 000 have been achieved by embedding elongated Au nanoparticles in a matrix of SiO_2.

There are many applications in the electronics sector, some of them are just listed; Power supply: fuel cells, solar cells, ceramic membranes in fuel cells and batteries; Chemical industry: fillers for varnish systems and impregnation of papers; Food and drink: package materials, storage life sensors and additives for better productions.

1.2.3.7. Medicinal and biological applications

There are a number of applications the nanoparticles have found in life sciences; nanobiotechnology is a special branch of life sciences that has developed due to this. In essence, living organisms are made of cells that are typically 10 μm across. Even smaller units such as proteins, which are about 5 nm, are comparable with the dimensions of the smallest man made nanoparticles. Nanoparticles therefore can be used as very small

probes that would be able to observe cellular processes without causing much strain into the system.[44]

1.2.3.8. Cancer therapy

Photodynamic therapy (PDT) encompasses the destruction of cancer cells by laser generated atomic oxygen, which is cytotoxic. Dyes, such as porphyrins, are used for this function but unfortunately the remaining dye molecules migrate to the skin and the eyes of the patient and make the patient sensitive to the daylight exposure for no less than six weeks. This side effect can be avoided by enclosing the hydrophobic dye inside a porous nanoparticle.[45] This does not temper with the oxygen generation ability of the dye, and the dye does not therefore travel to any other part of the body.

1.2.3.9. Multicolour optical coding for biological assays

Semiconductor single quantum dots have been successfully used to replace the organic dyes in various bio-tagging applications.[46] Combination of different sized nanoparticles, and hence having different fluorescent colours and then combining them with polymeric mirobeads, also furthers the capacity of this method.

More applications in medicine and biological sectors have been reported.[47] These include drug and gene delivery,[48] biodetection of pathogens,[49] probing of DNA structures,[50] tissue engineering[51] and MRI contrast enhancement.[52]

1.2.3.10. Cosmetics

Nanoparticles have also been employed as UV light protective additives in cosmetics. Doped nanoparticles offer effective absorption of harmful UV and then convert it into heat.

1.3. General introduction to thin films

Generally the term "thin film" refers to layers which have thicknesses of the order of microns or less (1 micron = 10^{-6} meters) and may be as thin as a few atomic layers. The properties of the film are largely affected by the properties of the underlying material (substrate) and can vary through thicknesses of the film. Although the substrate is the primary factor, other factors play in final properties of the film such as deposition temperature, carrier gas, flow rate and a few others depending on the deposition technique. The required property of the film can therefore be controlled through these properties.

There has been immense research into thin film materials due to their applications. Thin film optical devices underpin a multitude of applications since they provide the fundamental means of processing light by manipulation of its wavelength, amplitude and frequency.[53] Thin film devices can be found in ordinary lenses to the most complex satellite imaging systems. There are a large number of deposition techniques for these materials. Amorphous, single-crystalline, poly-crystalline thin films and coatings have all been deposited. Coatings generally refer to thicker films.

Many fields have benefited from the thin films such as semiconductors for microelectronics, optoelectronics, energy conversion devices, dielectrics for microelectronics and ceramic fibres and ceramic matrix composites.

1.3.1. Optical properties of thin films

The optical properties of thin films depend on the deposition parameters, microstructure, level of impurities and the growth technique.

1.3.1.1. Determination of optical constants

When light strikes the film it is either transmitted, reflected or lost to absorption or scattering. If the light beam incident on a homogeneous parallel-sided film is considered, the amplitude and polarization state of the light transmitted and reflected can be calculated in terms of the angle of incidence and optical constants of the materials involved[54] (incidence medium, film and substrate). As depicted in Figure 1.3, light from the incidence medium of refractive index N_0 passing through film material of index N_f, entering substrate of index N_s. The incident medium is often air and its refractive index is assumed to be equal to 1.0, the index of vacuum. Both film and substrate material can be transparent or absorbing in which the optical constant (or complex index of reflection), N, is given by:

$N = n - ik$ Equation 1.5

where n= refractive index and k= coefficient of extinction.

The refractive index can also be related to the dielectric constant of the material, $\varepsilon = n^2$, where ε is the dielectric constant of the material. The extinction coefficient is related to the absorption coefficient, α, by the expression

$\alpha = 4\pi k/\lambda$ Equation 1.6

α determines the intensity, I, transmitted through an absorbing medium by the exponential law of absorption[55]

$I = I_0 e^{-\alpha x}$ Equation 1.7

Fresnel constants can be conveniently used to express the reflectance and transmittance at the boundaries between these regions. If k is assumed to be zero, and that plane waves strike a plane boundary at normal incidence, the reflectance between two regions is given by

$$R = \left[\frac{n_0 - n_s}{n_0 + n_s}\right]^2$$ Equation 1.8

Regions expressed are transparent and only simplify into simple terms involving only n. When the regions are absorbing, these terms are large and cumbersome. Antireflection film materials operate on the principle of interference of the light reflected from the front and back of the surfaces of the films.

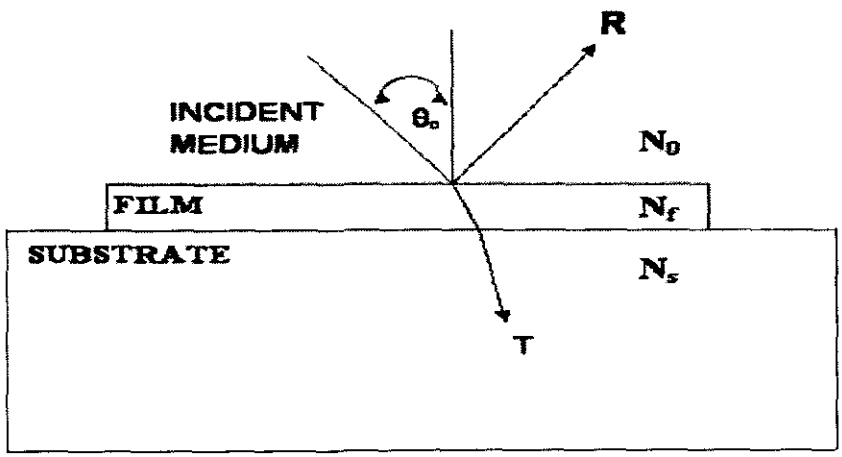

***Figure 1.3** A single thin film layer.*

The optical thickness of a thin film is defined as the index, n_f, times the physical thickness, d_f. The equation for calculating the reflectance of a single layer (in figure 1.3) at normal incidence for the wavelength of interest, λ_0, simplifies to:

$$R = \left[\frac{n_0 - \frac{n_f^2}{n_s}}{n_0 + \frac{n_f^2}{n_s}} \right]^2 \qquad \text{Equation 1.9}$$

This can be used to estimate how well a particular single layer coating will do. The film index needed for zero reflectance can be calculated at one wavelength as follows:

$n_f = (n_0\, n_s)^{1/2}$ Equation 1.10

Adding more layers gives advantage of being able to achieve a lower reflectance over much broader wavelength.

1.3.1.2. Band-gap determination

Generally transparent semiconducting materials are electrically conductive, and optically they act as a selective transmitting layer. At very large wavelengths, high reflection due to free electrons is observed, and for low wavelengths absorption due to the fundamental band-gap is observed. Therefore at low-wavelength region, the value of the band-gap can be estimated through standard relations.[56]

1.3.1.2.1. Direct band transitions

The variation of the imaginary part of the dielectric constant $\varepsilon_2(\varepsilon_2 = 2nk)$ with photon energy for direct band-to-band transition is given by

$(h\nu)^2\varepsilon_2 = \varepsilon_0\,(h\nu - \Delta E)^{1/2}$ $h\nu > \Delta E$ Equation 1.11

$\varepsilon_2 = 0$ $h\nu < \Delta E$ Equation 1.12

where $h\nu$ is photon energy, ε_0 is a constant independent of $h\nu$ and ΔE is the band gap. A plot of $(h^2\nu_2{}^2\varepsilon_2)^2$ versus $h\nu$ extrapolated to zero gives the value of ΔE.

1.3.1.2.2. Indirect band transition

For allowed indirect transitions for single phonon process, the imaginary part of the dielectric constant is given by

$$(h\nu)^2 \varepsilon_2^{a} = \frac{A'}{1-e^{Ep/kT}} (h\nu - Eg + Ep)^2 \qquad h\nu > (E_g - E_p)$$

Equation 1.13

$$\varepsilon_2^{a} = 0 \qquad h\nu < (E_g - E_p)$$

Equation 1.14

A' is a constant independent of the photon energy; E_p is the phonon energy and E_g is the indirect band-gap. The corresponding form of phonon emission is given by

$$(h\nu)\varepsilon_2^{(e)} = \frac{A'}{e^{Ep/kT} - 1} (h\nu - E_g - E_p)^2 \qquad h\nu > (E_g + E_p)$$

Eq. 1.15

$$\varepsilon_2^{(e)} = 0 \qquad h\nu < (E_g + E_p)$$

Eq. 1.16

If $h\nu > (E_g + E_p)$ the total value of ε_2 is given by

$$\varepsilon_2 = \varepsilon^{a} + \varepsilon_2^{e}$$

Eq. 1.17

The curve of $h\nu^{1/2}$ versus $h\nu$ extrapolated to low energies gives the value of $(E_g - E_p)$. A similar plot of $h\nu(\varepsilon_2 - \varepsilon_2^a)^{1/2}$, corresponding to the phonon emission term of equation (3), gives a photon energy intercept at $(E_g - E_p)$. Using these two intercept values of $(E_g - E_p)$ and $(E_g + E_p)$, the values of both E_p and E_g can be computed.

1.3.2. Thin film deposition methods

1.3.2.1. Chemical Vapour Deposition (CVD)

There are several methods of deposition technologies for thin film materials that have been reported.[57-60] Gas-phase chemical processes such as Chemical Vapour Deposition (CVD) have been identified as the major route in depositing materials of the nanometer to micrometer size range. This deposition method can provide highly pure materials with structural control of atomic to nanometer scale level.

The CVD method has long been in use. De Lodyguine in 1893 *et al*[57] first reported the deposition of W onto a carbon lamp filaments through reduction of WCl_6 by H_2. Of late, a more in-depth understanding of the process has led to wider applications of the CVD technique. CVD has been employed in coating technology, for producing functional semiconducting thin films, and coatings with improved surface properties such as protection against wear, corrosion, oxidation, chemical reaction, thermal shock and neutron adsorption. Materials that have been explored extensively include sulfides, nitrides, Si and III-V and II-VI materials.

CVD technology has expanded to include ceramics for manufacturing i.e. solar cells, ceramic fibres and turbine blades among others. CVD is also capable of being applied in many advanced products preparation including bulk materials, coatings as well as composites.

1.3.2.2. CVD system

CVD can either be done in a "closed" or "open" system. The "closed" system means both the reactants and products are recycled. This phenomenon occurs generally where reversible chemical reactions can occur with temperature difference. This phenomenon also occurs where there is difference in chemical activity in an isothermal system. The "open" system involves the removal of the reaction chemicals after deposition from the reactor, the recovery of the reactants can be done only if the expense justifies it. The CVD equipment is very variable. There is no single universal CVD equipment, but it is individually tailored for specific materials, and whether it is used for research and development or commercial production. Generally the CVD consists of three main components:

1.3.2.2.1. Chemical vapour precursor supply system

This component functions by generating the precursor vapour and then supplying it to the reactor chamber. The supply is designed with regard to the nature of the precursor. The precursor may either be a liquid, gas or a solid. Solid precursors are usually sublimed, whereas liquid sources use a bubbler to vaporise the reactants, and a carrier gas (H_2, N_2 or Ar) to transport the vapour into the reactor. The delivery of reactants depends on source

temperature, carrier gas flow rate and pressure over the source. The vapour precursor is then metered into the CVD reactor.

Carrier gases are delivered from high pressure gas cylinders via flow meters and control systems into the CVD reactor. These gases can be purified further to remove any oxygen, moisture or any other contaminants that might be picked in the gas transfer lines prior to entering the next phase. For binary and ternary component films, the precursors are often metered and mixed first in the mixing chamber before being fed into the reactor. Single source precursors have been widely used for the deposition of multicomponent film materials. Different precursors usually have different vaporisation rates and decomposition temperatures which gives rise non-stochiometric films.

1.3.2.2.2. CVD reactor

A reactor conventionally contains a loadlock for the transport and placement of the substrate in the chamber, a substrate holder, and a heating system with temperature control. The main purpose of the reactor is to heat the precursor to decomposition temperature. Two types of reactors are in use: (i) hot-wall and (ii) cold-wall reactor

Hot-wall reactor: substrate is housed into a heated furnace and heated indirectly. This system provides very precise temperature control and monitoring but the interior of the wall is also coated which results in maintenance problems and lower deposition efficiency. Another drawback is the depletion of gaseous reactants occurring along the reactor.

Cold-wall reactor: the substrate is heated directly either inductively or resistively whereas the wall of the reactor stays cold. The deposition will occur on the hot substrate and at least negligible deposition occurs on the wall. This fact is also supported by the fact that most CVD reactions are endothermic. This offers more control over the process, and minimises the deposition on the wall and the depletion of the precursor. There are various reactor configurations in use including horizontal, vertical, semi-pancake and multiple wafers.

1.3.2.2.3. The effluent gas handling system

The main purpose of this component is to remove hazardous by-products and unreacted precursor safely. Nitrogen trap can be used to trap unreacted precursor and corrosive by-products. Trapping of such material prevents them from entering the rotary or diffusion pump which can cause damage. Expensive unreacted precursor material may be collected at the output and recycled, but only if it is economical to do so. Deposition efficiency directly influences the degree of recycle and disposing procedures.

CVD products and reactants are often corrosive, toxic, oxidising and have high vapour pressure. This requires post deposition section of the reactor to be efficient to render these chemicals harmless before disposal. Toxic gas detectors are always recommended and special precautions should be observed at all times. Effluent gas handling system should be made to specifically cater for individual CVD system. This is due to the use of different precursor types for different CVD systems. There are various variants of CVD,

with modifications in all three components of the CVD setup. A few of these are discussed next.

1.3.2.3. Aerosol Assisted Chemical Vapour Deposition (AACVD)

This CVD method involves the use of an aerosol precursor and thus Aerosol-Assisted CVD. Several aerosol generation methods are in use, such as ultrasonic, electrostatic and electrospraying. They are used to generate the aerosol of the precursor into finely divided sub-micrometer liquid droplets (aerosol). The precursor can be prepared by dissolving a solid or liquid starting material into an organic solvent or a mixture of solvents to assist the evaporation of the chemicals and provide additional thermal energy for the decomposition or dissociation of the chemical precursor. The aerosol is transported into the heated zone, where the solvent rapidly evaporates or get combusted, and the precursor undergoes subsequent decomposition and/or chemical reaction near or on the surface of the substrate to deposit the desired film material.

1.3.2.3.1. Deposition mechanism and process principles

The precursor undergoes several steps during the AACVD reaction.[58] A stepwise presentation is given below with reference to Figure 1.4.

1) Gaseous reactant species generation.
2) The gaseous precursor is transported into the reaction chamber.
3) Phase reaction of the reactants occur forming intermediate species:
    a) At temperatures higher than the decomposition temperature of the intermediate species in the reactor, homogeneous gas phase reaction occurs. The decomposition/chemical reaction occurs forming powders and volatile by-

products in the gas phase. The powder collects on the substrate and the by-products transported away. Poor adhesion is always the main problem.

b) At temperatures below decomposition temperatures of the intermediate phase, diffusion/convection of the intermediate across the layer close to the substrate occurs. These species then subsequently undergo steps 4 to 7 below.

4) The gaseous reactants are absorbed onto the hot substrate; heterogeneous reactions occur at the gas-solid interface producing the film and by-products.

5) Diffusion of the heated deposit along the host substrate forms crystallization centers and growth of the film.

6) The by-products are then removed from the boundary layer through diffusion/convection.

7) The by-products and unreacted gaseous precursor are then transported away from the deposition chamber.

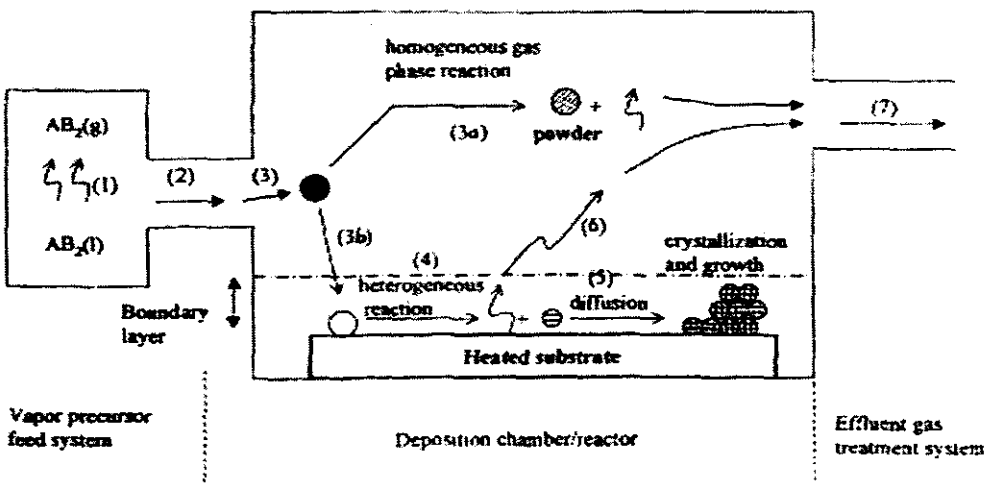

Figure 1.4 *Key steps during the precursor decomposition leading to the thin film deposition.*

Aerosol droplet size and its distribution are much dependent upon the aerosol generation

method. This in turn controls the nature and composition of the deposition product. Ultrasonic aerosol generation uses piezoelectric transducer placed underneath the precursor solution. The nature of the liquid precursor, intensity and wavelength of the ultrasonic generator affect the properties of the aerosol. The diameter of the droplets can be determined using the equation established by Land[61]:

$$d = k\,[2\pi\sigma / \rho f^2]^{1/2} \qquad \text{Equation 1.18}$$

Where k is a constant, r is the surface tension and f is the frequency of excitation. The diameter of the droplets is a function of $\lambda(d = k'\lambda)$ and hence, the ultrasonic frequency. Narrow droplet size distribution can be easily achieved using the ultrasonic method.

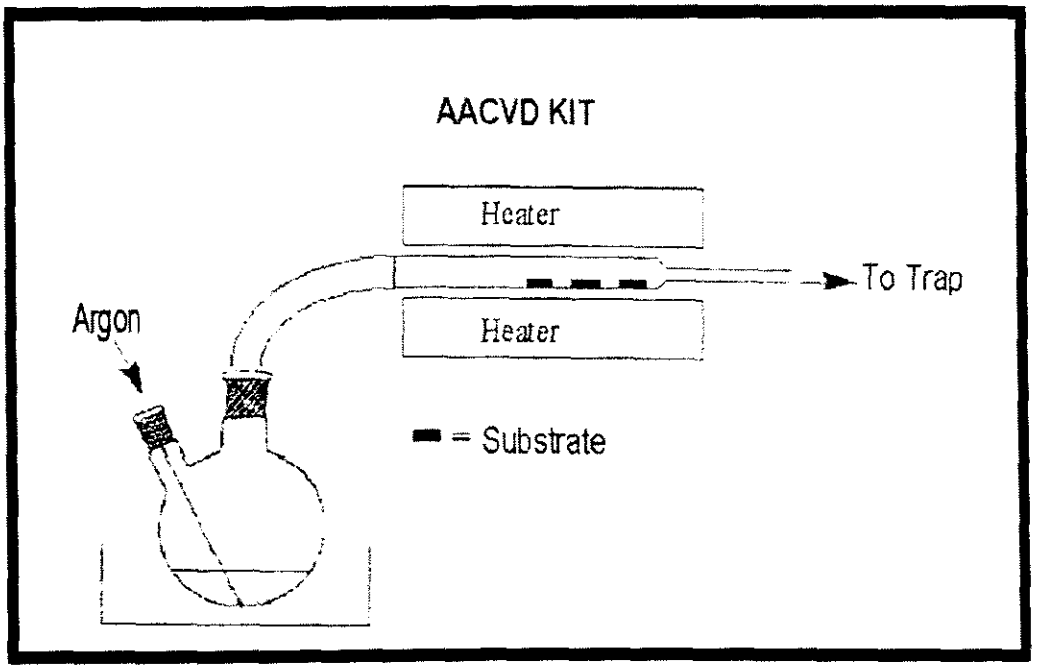

Figure 1.5 *A simplified schematic representation of the AACVD kit*

A general AACVD kit is presented in Figure 1.5. It contains a two-neck flask where the precursor aerosol is generated, a water bath at the top of the piezoelectric transducer for the humidifier, a reactor tube where the substrates are inserted, the furnace and the effluent system. As indicated in the above diagram the AACVD can be tailored easily to the needs of a specific reaction.

1.3.2.4. Metal-Organic Chemical Vapour Deposition (MOCVD)

Metal-organic chemical vapor deposition (MOCVD) is another form of CVD, which derives its name from the use of metalorganics as precursors. Metalorganics refer to compounds containing metal atoms bonded to organic radicals. The use of organometallic precursors has led to the naming of the process to Organometallic CVD (OMCVD) to reflect precisely the type of precursor used. This method has been exploited intensively in the deposition of semiconductor materials (IV-VI, III-V and II-IV), as well as metallic films and dielectrics. Metalorganic precursors usually undergo pyrolysis or decomposition. Most of the precursors have very low decomposition and pyrolysis temperatures compared with material precursors such as halides or halohydrides. From this observation they allow the use of lower decomposition temperatures than most CVD methods. An example:

Organometallic $Ga(CH_3)_3 + AsH_3 \rightarrow GaAs + 3CH_4$

600-800 °C (0.1-1 atm)

Halide $Ga + AsCl_3 + {}^3/_2\, H_2 \rightarrow GaAs + 3HCl$

800 °C (reduced pressure)

Temperature dependence of this technique is very profound.

T< 500 °C: The reaction is kinetically limited

550 °C ≤T≤ 750 °C: The reaction is diffusion-related.

T> 800 °C: homogeneous reactions and parasitic deposition on the walls of the reactor limit the reaction.

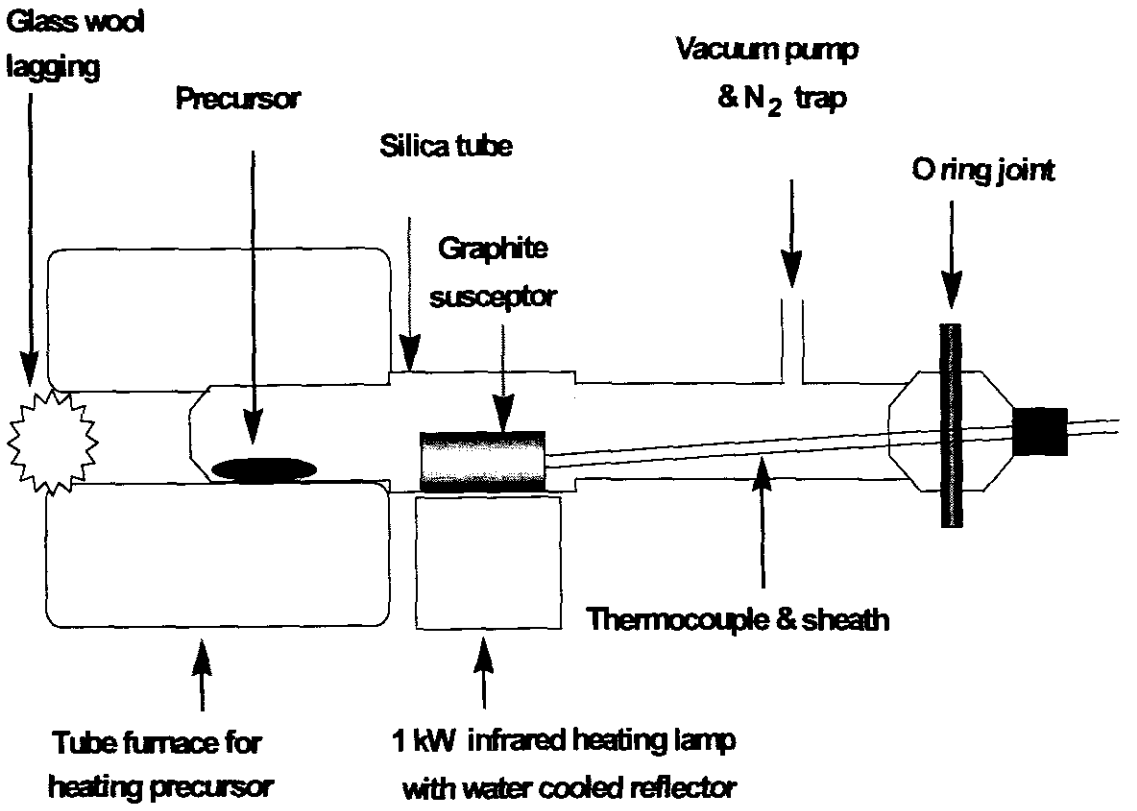

***Figure 1.6** A schematic representation of the LP-MOCVD apparatus.*

Figure 1.6 shows the scheme for the MOCVD reactor. These reactions are generally endothermic and use cold-wall reactors with single temperature zone. The thermal environment can be supplied using resistance, rf and IR lamp heating which goes along with water cooled reflector as in the example in Figure1.6 above.

1.3.2.5. Flame Assisted Chemical Vapour Deposition (FACVD)

Flame assisted chemical vapor deposition (FACVD) is a variant of CVD that involves combustion of liquid or gas precursor delivered into diffused or premixed flames, where the precursor will decompose and undergo chemical reaction and/or combustion in the flame. Vaporization, decomposition and chemical reactions are all catered for by the flame source, which provides the required thermal environment. The substrate is also heated by the flame source, which enhances the diffusion and surface mobility of the absorbed atoms on the substrate surface during the film deposition. Notably in this method, the time taken for the vaporization, decomposition and chemical reactions to occur is much shorter compared with conventional CVD methods.

The fuel for the FACVD can either be H_2 or hydrocarbons. The use of hydrocarbons leads to formation of soot, on the other hand H_2 combustion is faster and it does not produce condensed species compared to hydrocarbons. Working temperatures are between 1727-2730 °C in general, which leads to homogeneous reactions and thus deposition of powders. In addition to the general process parameters (precursor/fuel ratios), additives can be introduced into the flame to alter the size, phase and shape of the product.[62,63] There is a large temperature fluctuation of the flame source during decomposition, due to layers of the temperature gradient in the flame, which limits this

technique. Powders produced using FACVD have been used as starting materials for the fabrication of advanced ceramics. Figure 1.7 shows a schematic diagram of the FACVD setup.

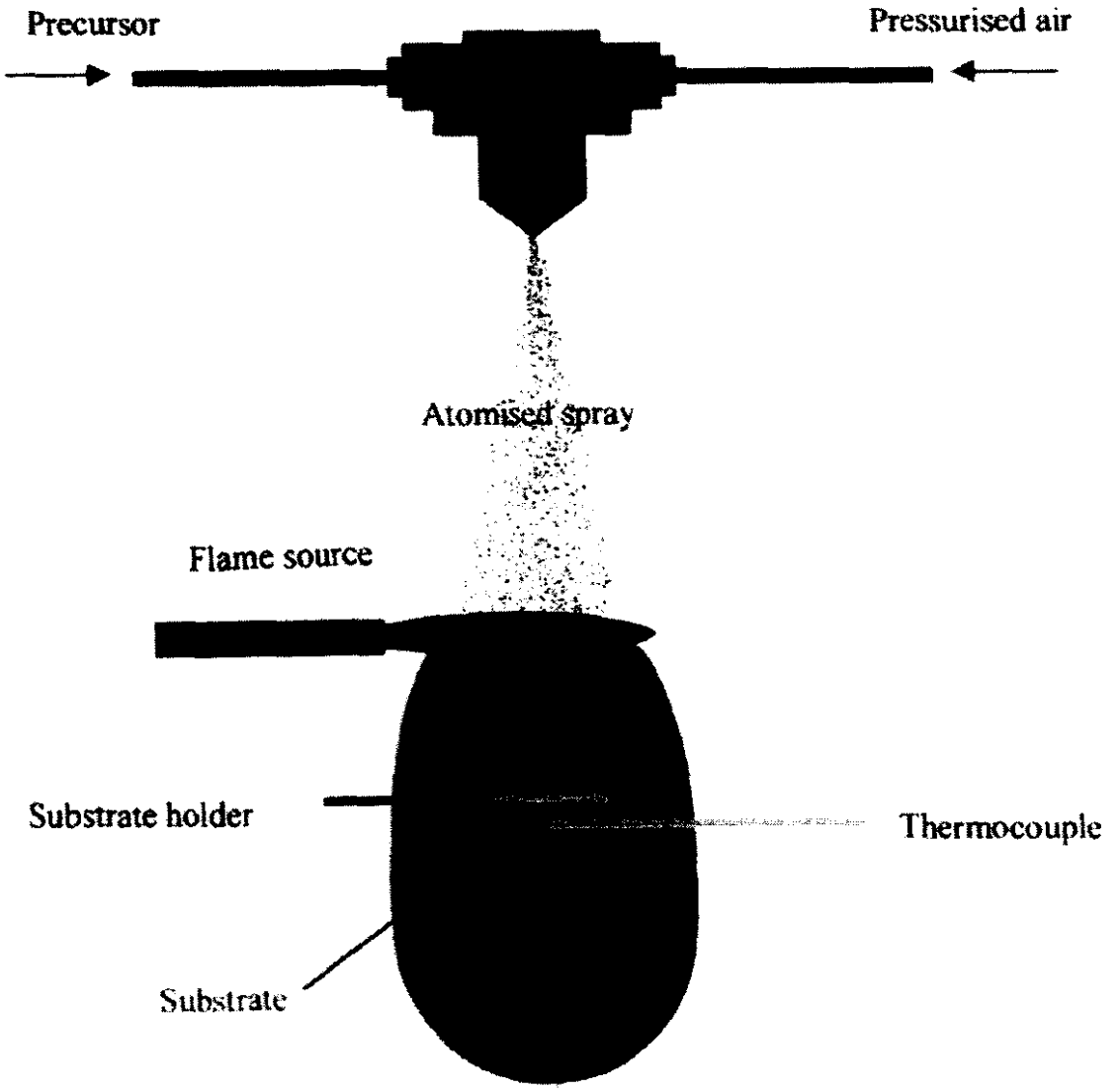

***Figure 1.7** A schematic diagram of the FACVD apparatus*

1.3.2.6. Plasma Enhanced Chemical Vapour Deposition(PECVD)

This method is generally referred to as glow discharge chemical vapor deposition. Plasma is used as activation source. The use of the plasma helps the deposition to occur at low temperatures and at reasonable rates. A reduced pressure of <1.3kPa is used. The high voltage electrical power is supplied to the gas, this result in the gas breaking down and generating a glow discharge plasma consisting of electrons, ions and electronically excite species. The electron impact ionizes and dissociates the vapor reactants and hence generating chemically active ions and radicals that undergo heterogeneous chemical reaction at or near the heated substrate forming a deposit of film.

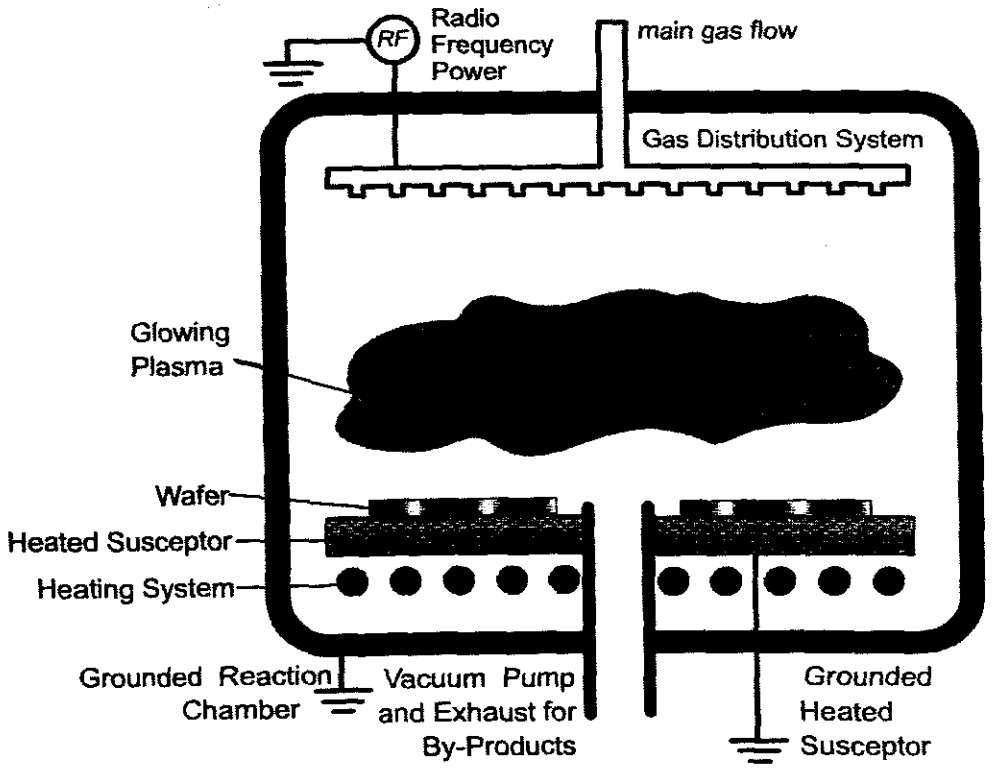

Figure 1.8 *A schematic representation of the PECVD apparatus.*

The electron temperature of the electrons can be on the order of 20 000 K or higher, while the temperature of the vapour reactants may remain near room temperature, which depends upon the pressure at which the discharge is operated. Different types of reactors can be used for the PECVD; direct reactors such as rf diode, microwave and ICP involve gaseous precursors and inert carrier gases substrates being placed directly in the plasma source region. Figure 1.8 shows a typical PECVD setup. Films with large hardness (about 8 000 Hk) have been deposited using PECVD.

1.3.2.7. Photo Assisted Chemical Vapour Deposition (PACVD)

PACVD relies on the absorption of light to raise the substrate temperature and cause thermal decomposition of the precursor in the gaseous or substrate surface. The decomposed intermediate products then undergo further heterogeneous chemical reactions on the substrate to form the desired film. Pressures ranging between 0.01-1 atm can be employed in PACVD. Numerous light sources are used, such as arc lamp, CO_2 lasers and argon lasers. A photothermal (pyrolytic) or photolytic mechanisms initiate the decomposition and/ or chemical reaction. Photothermal mechanism is usually used for selected area deposition which can be achieved by projection imaging with the use of a pulsed laser or laser scanning source. This avoids any thermal damage to the substrate. In the photolytic method UV is used. The wavelength ($\leq$ 250 nm) in the UV spectrum can cause the non-thermal decomposition formation of radicals from chemical precursors and allow the deposition to occur at lower temperature. Semiconductors (III-VI) and insulators (Si_3N_4) for interlayer electrical insulation have been deposited using this technique.

1.3.2.8. Electrochemical Vapour Deposition (EVD)

EVD is another variant of CVD. Dense ion or electron-conducting oxide films can be deposited onto porous electrodes at elevated temperatures using EVD. Typical working temperature ranges between 100-1327 °C and pressure is reduced to below 1 kPa. EVD is the key processing technique for the fabrication of seamless tubular oxide fuel cell (SOFC) technology.[64,65]

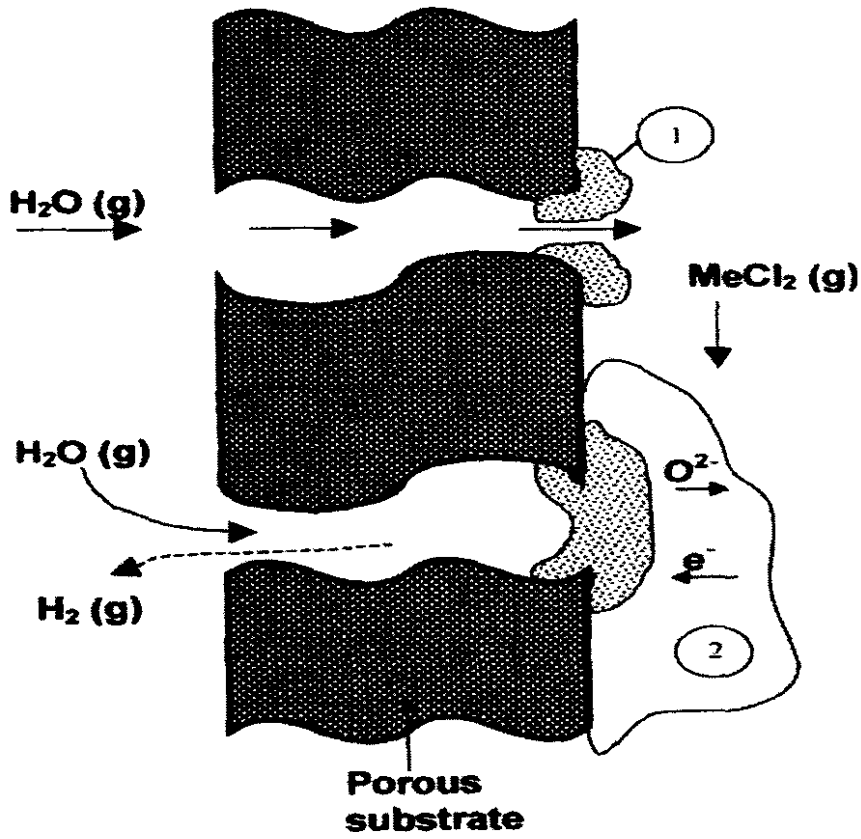

***Figure 1.9** A scheme for the EVD apparatus*

Stage 1 $$MCl_2(g) + H_2O = MO(s) + 2HCl(g) \quad (1)$$

Stage 2 $$H_2O(g) + 2e^- = H_2(g) + O^{2-} \quad (2)$$

$$MCl_2(g) + O^{2-} = MO(s) + Cl_2(g) + 2e^- \quad (3)$$

As represented in diagram 1.8, the EVD process works in two stages in the formation of a dense oxide layer. In stage 1, a direct reaction of the oxygen source and metal source reactants produces the porous oxide layer. In stage 2, the growth of the oxide over the pores occurs through an electrochemical process. Here, the reduction of the water vapour produces the oxygen ions, which subsequently diffuse through the oxide film to the metal chloride side and react with the metal chloride to form the oxide layer as shown in equation (2) and (3).

1.3.3. Applications of thin films

There are a vast number of applications of thin films in today's research. Although it would be impossible to mention all of them but there are quiet a number of applications that are leading the pack. Through the combination of electrical and optical properties of thin films, they have found a variety of applications. Coatings such as In_2O_3, SnO_2 and indium tin oxide (ITO or In_2O_3:Sn) are widely used in many areas related to their function as heat mirrors. Suitable material for specific application depends on its electrical, optical properties and mechanical stability. Optimization of both electrical and optical parameters is essential in all transparent conductive films. Although there is an overlap in most technological applications of thin films, a few stands out as listed next.

1.3.3.1. Wavelength Selective Applications

Solar energy conversion is one area where wavelength-selective surfaces play a vital role. Two classes of these surfaces: selective black absorbers and transparent heat mirrors. Selective black absorber has a high absorptivity for solar radiation and a low emissivity

for infrared thermal radiation. An absorber is used in solar collectors to convert solar radiation into thermal energy. Thermal radiation, which is the dominating loss mechanism at high operating temperatures, can be reduced by using these absorbers with high solar absorptivity and high infrared reflectivity (low infrared emissivity). Most common surfaces include films of Ni-black, Cu-black and Cr-black.

1.3.3.2. Electronic Components

Thin films have found applications in the fabrication of electronic components, more specifically microelectronic integrated circuits and solid-state devices. This is undoubtedly the area where there is the widest and most demanding need for applications of thin films. Semiconductor materials, dielectric and insulating materials are at the fore front of this area of research.

1.3.3.3. Electronic Displays

Transparent conducting films have been extensively used as transparent electrodes in various devices, such as Liquid Crystal Displays (LCD), Light Emitting Diodes (LED), Electroluminescent Displays (ELD), image sensors based on amorphous Si and many others.[64] The electrode material for display device must be conductive and optically transparent. It is also essential to pattern the transparent conductive layer, for which etching is required.

1.3.3.4. Magnetic Films for Data Storage

Thin films of magnetic materials have found extensive use in coating for commercial materials such as data storage in computers and control systems. The deposition process should produce magnetic materials with a high degree of hardness.

1.3.3.5. Optical Data Storage

Compact disks and computer memory systems have been improved in their optical data storage capabilities by the use of thin films. Organic polymer materials are deposited a storage media. Thin film materials can also be used as protective overcoats for these systems.

1.3.3.6. Other applications

There are a number of other applications that have been reported. Thin films of semiconductive materials are also deposited to provide protection from electrostatic discharges. Because the conductance of the semiconductor materials is modified directly by the interaction with an active gas, they are used as gas sensors. This is through the chemisoption of the active gas on the surface of the material film. Gases that could be detected this way include carbon monoxide, methane and propane, hydrogen, ethanol and nitrogen oxides (NO and N_2O). Apart from detection of specific gases, they can also measure odours.[65]

Hard surface coatings, optical waveguides, electrodes in electro-optic modulators, [66] buffer layers in superconducting thin films,[67] gate electrodes in capacitors, active elements in transparent thermocouples,[68] and as alternative materials for varistors[69] are all

applications reported in literature although some of these are still in their infant stages of development.

1.4 References

1. Deyand S. and Jain V.K., *Platinum Metals Rev.*, 2004, **48**, 1, 16
2. Johnston W.D., *J. Inorg. Nucl. Chem.*, 161, **22**, 13
3. Feichter S. and Kuhne H., *J. Cryst. Growth*, 1983, **87**, 517
4. Oftedal I., *Z. Phys. Chem.*, 1958, **135**, 291
5. Lutz H.D., Jund M. and Waschenbach G., *Z. Anorg. Allg. Chem*, 1987, **87**, 554
6. Hulliger F., *Nature*, 163, **200**, 1064
7. Huang J.K., Huang Y.S. and Yang T.R., *J. Cryst. Growth*, 1994, **135**, 224
8. Parthe E., Hohnke D.K. and Hulliger F., *Acta. Cryst.*, 167, **23**, 832
9. Beck J. and Hilbert T., *Z. Anorg. Allg. Chem.*, 2000, **626**, 72
10. Liao P.C., Ho C.H., Huang Y.S. and Tiong K.K., *J. Cryst. Growth*, 1997, **171**, 586
11. Lee C.S. and Miller G.J., *Inorg. Chem.*, 1999, **38**, 5139
12. Geller S., *Acta. Cryst.*, 1962, **15**, 1198
13. Schmid G., *Clusters and Colloids*, VCH:Winheim, 1994
14. Sinfelt J.H., *Bimettalic Catalysis--Discoveries, Concepts and Applications*, Wiley, New York, 1983
15. Gates B.C., Guczi L. and Knozinger H., *Metal clusters in catalysis*, Elsevier, Amsterdam, 1986
16. (a) Sinfelt J.H., Via G.H. and Lyte F.W., *J. Chem. Phys.*, 1980, **72**, 4832

(b) Via G.H., Drake K.F., Meitzner G., Lyte F.W. and Sinfelt J.H., *Catal. Lett.*, 1995, **5**, 25

17. Malm J., Bovin J., Petford-Lorg A., Smith D.J. and Schmid G., *Angew. Chem., Int. Ed. English*, 1988, **27**, 555
18. Nashner M.S., Sommerville D.M., Lane P.D., Alder D.L., Shapley J.R. and Nuzzo R.G., *J. Am. Chem. Soc.*, 1996, **118**, 12964
19. Dai H., Wony E.W. and Leiber C.M., *Science*, 1996, **272**, 523
20. Rodriguez N.M., Kim M.S. and Baker R.T.K., *J. Mater. Chem.*, 1994, **98**, 13108
21. Che G., Lakshni B.B., Martin C.R.and Fisher E.R., *Langmuir*, 1999, **15**, 750
22. Baum R.M., *Chem. Eng. News*, 1997, **75**, 39
23. (a) Alivasatos A.P., *Science*, 1996, **271**, 933

    (b) Schon G. and Simon U., *Colloid Polym. Sci.*, 1995, **273**, 101
24. Henglein A., *Chem. Rev.*, 1989, **89**, 861
25. Brus L.E., *J. Chem. Phys.*, 1983, **79**, 5566
26. Brus L.E., *J. Chem. Phys.*, 1984, **80**, 4403
27. Brus L.E., *J. Chem. Phys.*, 1986, **90**, 2555
28. Chestnoy N., Harris T.D., Hull R. and Brus L.E., *J. Phys. Chem.*, 1986, **90**, 3393
29. Bowen-Katan J.E., Calvin V.L. and Allivasatos A.P., *J. Phys. Chem.*, 1986, **98**, 4109
30. Steigerwald M.L. and Brus L.E., *Acc. Chem. Res.*, 1990, **23**, 183
31. Weller H., *Angew. Chem., Int. Ed. English*, 1993, **32**, 41
32. Weller H., *Adv. Mater.*,1993, **5**, 88
33. Trindade T., O'Brien P., Zhang X. and Motavelli M, *J. Mater. Chem.*, 1997, **7**, 1011

34. Trindade T., Monteire O.C., O'Brien P. and Motavelli M., *Polyhedron*, 1999, **18**, 1171

35. LaMer V.K. and Dinegar R.H., *J. Am. Chem. Soc.*, 1950, **72**, 4847

36. Wang Y. and Herron N., *J. Phys. Chem.*, 1987, **91**, 257

37. Watzke H.J. and Fendler J.H, *J. Phys. Chem.*, 1987, **91**, 854

38. Wang Y., Suna A., Mahler W and Kasowski A., *J. Chem. Phys.*, 1987, **87**, 7315

39. Henglein A., *Ultrasonics*, 1987, **25**, 6

40. Suslick K.S., *Sonochemistry, Science,* 1990, **247**, 1439

41. Arul Dhas N. and Gedanken A., *Chem. Mater.*, 1997, **9**, 3144

42. Yan Y., Liu H and Liew K.Y., *J. Mater. Chem.*, 2001, **11**, 3387

43. Toshima N. and Wang Y., *Chem. Lett.*, 1993, **1**, 1611

44. Taton T.A., *Trends Biotechnol.*, 2002, **20**, 277

45. Roy I., Onulchansky T.Y., Pudavar H.E., Bergey E.J. Oseroh A.R., Morgan J., Dougherty T.J. and Prasad P.N., *J. Am. Chem. Soc.*, 2003, **125**, 7860

46. Parak W.J., Gerion D., Pellegrino T., Zanchet D., Michael C., Williams C.S., Boudareau R., Lee Gros M.A., Larabell C.A. and Allivasatos A.P., *Nanobiotechnology,* 2003, **14**, 15-R27

47. Salana O.V., *J. Nanotech.*, 2004, **2**, 3

48. Mah C., Zolotukhin I., Fraites T.J., Dobson J., Batich C. and Byrne B.J., *Mol. Therapy*, 2000, **1**, S239

49. Eldestein R.L. and Tamanaha C.R., *Biosensors Bioelectron.*, 200, **14**, 805

50. Nam J.M., Thaxton C.C. and Mirkin C.A., *Science,* 2003, **301**, 1884

51. Ma J, Wong H, Kong L.B. and Pong K.W., *Nanotech.*, 2003, **14**, 619

52. Weissleder R., Elizondo G., Wittenburg J., Robito C.A., Bengele H.H. and Josephson L., *Radiology*, 1990, **175**, 489

53. Lewis K. and Quineti Q., 46th Annual Technical Conference Proceedinds, Society of Vacuum Coaters, 2003, ISSN 0737-5921

54. Bjorn M and Wolf E., *Principles of Optics*, Pergammon Press, Oxford, 1970, p51-70

55. Jenkins F.A. and White H.E., *Fundamentals of Optics*, McGraw-Hill, New York, 1976, p231

56. Abeles F., *Optical Properties of Solids*, North-Holland Press, Amsterdam, 1972

57. De Lodyguine J.S., *Illumination for Incandescent Lamps*, US Patent 575002, 1893

58. Choy K.L. In: Nalwa H.S., editor: *Handbook of Nanostructrured Materials and Nanotechnology,* Vol. 1: *Synthesis and Processing*, San Diego, California: Academic Press; 2000, p533

59. Xie S., Li W., Pan Z., Chang B. and Sun L., *Mater. Sci. Eng.*, 2000, **A286**, 1508

60. Dai H., Franklin N. and Han J., *J. Appl. Phys. Lett.*, 1998, **73**, 1508

61. Rayleigh J.W.S., *The Theory of Sound*, Vol. 2, New York, Dover, 1945

62. Hayness B.S., Hander H., Wagner H.G.G. In: 17th International Symposium on Combustion Institute, 1979, p1365

63. Akhtar M.K., Prastinis S.E., Mastrangelo S.V.R., *J. Am. Ceram. Soc.*, 1992, **72**, 3408

64. Hoheisel M., Mitwalsky A. and Mrotzek C., *Phys. Status. Solid. A,* 1991, **123**, 461

65. Fukui K., *Sens. Actuators*, 1991, **B5**, 27

66. Chen R.T. and Robinson D., *Appl. Phys. Lett.,* 1992, **60**, 1541

67. Kellett B.J., Gauzzi A., James J.H., Dwir B., Paveuna D and Reinhart F.K., *Appl. Phys. Lett.*, 1990, **57**, 2588

68. Kreider K.G., *Sens. Actuators*, 1992, **A34**, 95

69. Gould R.D., Hassan A.K. and Mahmood F.S., *Int. Electron.*, 1994, **76**, 895

CHAPTER 2

BASIC PRINCIPLES OF INSTRUMENTAL TECHNIQUES

2.1. X-ray powder diffraction

2.1.1. Introduction

In the crystalline state, all atoms are arranged in patterns which are characterized by periodic repetitions in three dimensions. Every atom in a crystal scatters the X-ray beam incident upon it in all directions. Due to the reason that even small crystals contain a very large number of atoms, the chance that the scattered waves would interfere constructively would be slim, if not nonexistent, except for the fact that the atoms are regularly arranged in repetitive manner in the crystal.[1]

2.1.2. Principles of powder diffraction method

2.1.2.1. Bragg's Law

Scattering from a crystal can be described in terms of reflection from a set of lattice planes. When two or more planes are considered the path length from incoming wave front, to plane, to scattered wave front is longer in the lower plane. An illustration of such phenomenon is presented in Figure 2.1 below

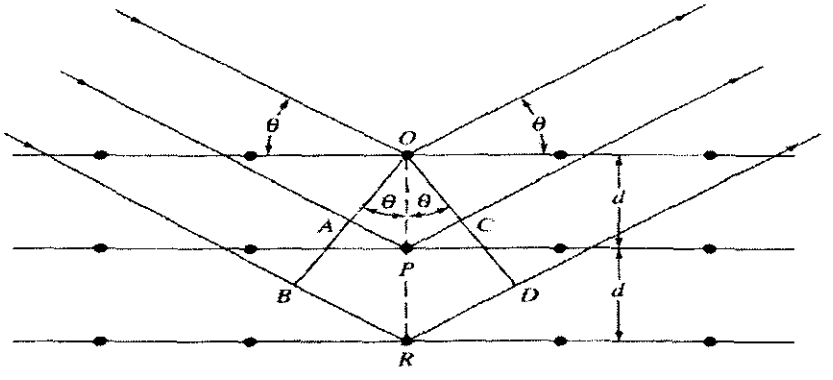

***Figure 2.1** The diffraction of the X-rays*

The greater path difference is:

$\Delta = ABC = 2AB$ Equation 2.1

Since $AB = d_{hkl} \sin\theta$ Equation 2.2

The total path difference is $\Delta = 2AB = 2\, d_{hkl} \sin\theta$ Equation 2.3

If both these planes scatter in phase, the path difference, Δ, must be an integral number of wavelengths i.e. $n\lambda$, where n is an integer. Therefore, the condition for scattering-in-phase is

$n\lambda = \Delta$ and $n\lambda = 2d_{hkl} \sin\theta$ Equation 2.4

This condition is known as Bragg's law,[2] and this equation is known as Bragg equation. This condition gives the relationship between the wavelength of the X-ray beam, λ, the angle of diffraction, θ, and the distance between each set of planes of the crystal lattice, d.

2.1.2.2. General considerations

For X-ray powder method, a powder sample with infinite number of randomly oriented crystallites is used. The principles in the production of a powder diagram can be appreciated by considering the simplified experimental setup in Figure 2.2.

An X-ray beam is defined by the pinhole from the tube. A photographic film is placed normal to the X-ray beam. The beam then travels through the powder sample, meeting thousands of grains of the powder, each of these grains acts as a tiny crystal in a different orientation. Each set of lattice planes, hkl, will scatter at the appropriate 2θ angle, according to Bragg's condition.

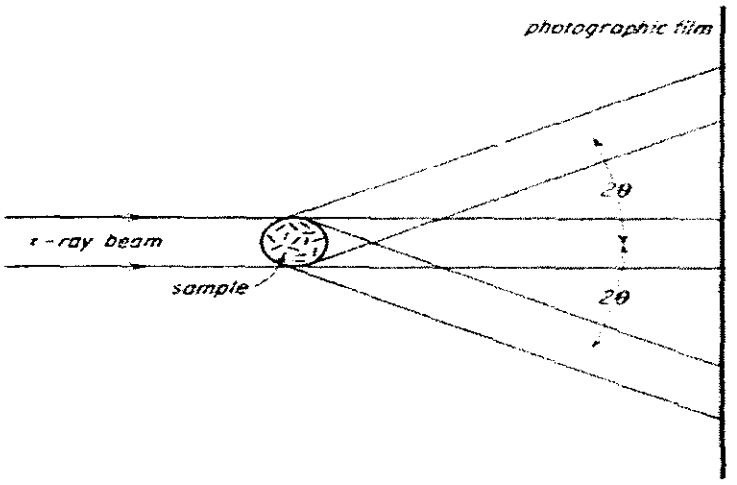

***Figure 2.2** A simplified experimental arrangement for the production of the powder diagram from XRD.*

Since all possible orientations of the crystallites should be present, a cone of scattering will be formed at each value. The cones could be intercepted at different 2θ values in an X-ray film, as in Debye-Scherrer method.[3] Analysis of the film of the material is as follows: i. Obtain 2θ angles, ii. Calculate $\sin^2\theta$, iii. Index lines, i.e. assign hkl values, $\sin^2\theta = c\,(h^2+k^2+l^2)$, where $c=q^2/4a^2$ and iv. Then finally find the mean value of a.

2.1.2.3. Geometry of Diffraction

The phenomenon of X-ray diffraction results from scattering in which the X-rays are scattered by electrons of the atoms without any change in wavelength. Bragg's Law can be used to express conditions which are suitable for the diffraction to occur from such scattering. The diffraction pattern of the crystal, which comprises both the positions and intensities of diffraction effects, is a fundamental property of the substance; this serves both for a speedy identification and as well as a complete structure elucidation. The

analysis of diffraction positions leads to knowledge of the size, shape and orientation of the unit cell. Measuring and analyzing the intensities leads to the immediate location of the positions of the individual atoms.

The scattering can either be caused by lattice atoms, where atoms act as an electrical system capable of being disturbed by an external field. The fluctuation of the electric field of an impinging electromagnetic wave displaces the electrons of the atom. Due to this reason they undergo vibration having the same frequency as the electromagnetic wave. The diffraction can also be caused by the whole crystal structure. Any crystal structure can be regarded as several mutually displaced lattice arrays. Each and every lattice array can diffract X-rays as if reflecting them from a plane (hkl).

2.2. Photoluminescence

2.2.1. Introduction

Generally, photoluminescence (PL) is defined as phosphorescence and fluorescence and these are somewhat similar in their mechanisms. If the molecule is excited by light and there seems to be no chemical reaction resulting, then the molecule will eventually return to ground state with the corresponding release in energy either through phosphorescence or fluorescence. Fluorescence does not involve change in electron spin and is therefore very short-lived, with luminescence ceasing almost immediately ($<10^{-5}$ s). In contrast, phosphorescence involves a change in electron spin, which causes the radiation to endure for a detectable time after irradiation is terminated, lasting from 10^{-3} s to the order of seconds.

2.2.2. Principles of photoluminescence

The discussions on both fluorescence and phosphorescence can be appreciated by the following illustration, Figure 2.3:

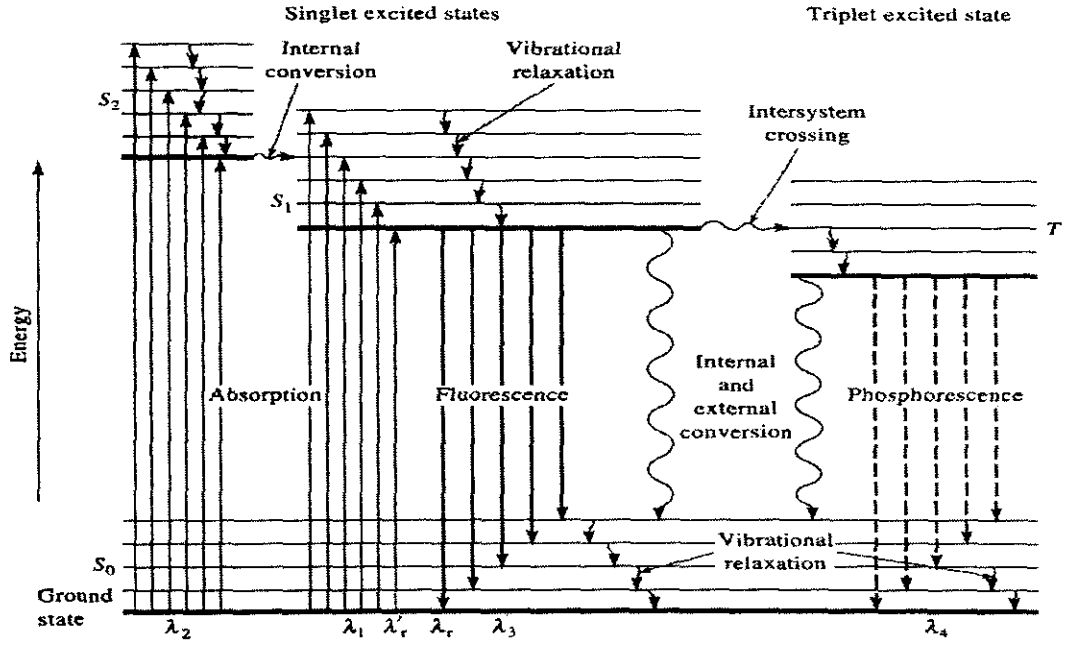

***Figure 2.3** The energy level diagram for a photoluminescent system.*

2.2.2.1. Fluorescence

When molecules are radiated with light of appropriate frequencies they can undergo absorption from the ground state to their first excited electronic state. At excited states, molecules can be in any of the several excited states as opposed to the single ground state. All these excited states are unstable, then a molecule can directly return to ground electronic level with the emission of radiation and hence fluorescence is observed. The emission spectra are displaced towards longer wavelength. The reason being that the time

required to execute a vibration (~10^{-13} seconds) is much shorter than the decay or mean lifetime (~10^{-9} seconds), most of the excess vibrational energy will be dissipated to the surroundings, and the excited molecules will now decay in their ground vibrational levels.

If the fluorescence is not the only decay mechanism available; the fluorescence is said to be quenched. A few of these mechanisms have been identified i.e. internal conversion, external conversion and excitation transfer.

2.2.2.2. Phosphorescence

Phosphorescence is quite a different mechanism of the return of excited molecules to ground electronic state. It is generally distinguished from fluorescence because: 1. possesses much longer decay process; 2. at room temperature it is not observable in solutions and 3. It is rarely observed in gases. Phosphorescence decay involves the molecule decaying to a metastable state, which is a triplet as depicted in Figure 2.3 above.

The decay from higher singlet to the triplet is by the radiationless transition. Practically there are always some spin-orbit interactions to 'mix' the states so that triplet↔singlet transitions are allowed. Triplet states always lie lower than the corresponding singlet level and it is due to this that phosphorescence has got longer wavelengths compared to both fluorescence and absorption. The most direct evidence of singlet←triplet decay mechanism is provided by magnetic susceptibility and Electron Spin Resonance

measurements. There are also a number of mechanisms which can deactivate the triplet states i.e. collision, paramagnetic ion quenching and spin conversion.

2.3. Mass spectroscopy

2.3.1. Introduction

Mass spectroscopy is one of the widely applicable analytical techniques due to its vast practical information it yields. This information includes elemental composition of samples of matter; the structure of inorganic, organic and biological compounds; the qualitative and quantitative composition of complex mixtures; the structure and composition of solid surfaces; and isotopic ratios in samples.

2.3.2. Principles of mass spectroscopy

The principles of mass spectroscopy can be appreciated by considering the schematic setup in Figure 2.4: The cell (ion source) is contained within a high vacuum chamber which is contained in a homogeneous magnetic field. After the ion formation, ions are trapped in the cell, held in radial direction (xy plane) by the magnetic field and along the axis of the magnetic field (z-axis) by small voltages (0.5-5V) applied to the trapping plates. Either positive or negative ions can be trapped in the cell simply by changing the polarity of the applied voltage. Due to momentum conservation, the initial ion velocity upon ion formation is the same as the velocity of its neutral precursors.

Without coherent motion, a signal cannot be detected. By applying a very short, high intensity, broadband radiofrequency signal to excite plates of the cell, the ions absorb

energy, which accelerates them into larger orbits and causes them to move together (coherent motion).

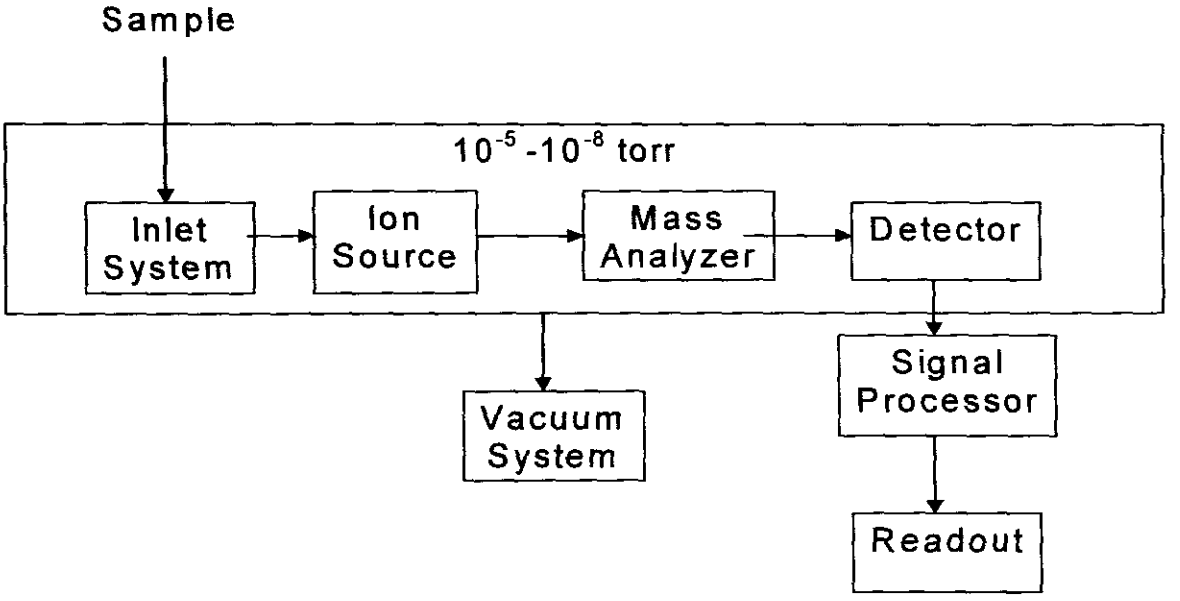

Figure 2.4 *Components of a basic mass spectrometer.*

The orbiting packet of ions induces a small alternating current in the receiver plates.[4] This signal is converted into a voltage, amplified, digitized and stored in a computer, or recorded in the oscilloscope. The frequency components of the image current correspond to the cyclotron frequencies of the ions present in the cell.

The frequency of the cyclic motion, ω, within the cell is given by the cyclotron equation:

$\omega = KqB/m$ Equation 2.5

Where K= proportionality constant, q= charge of the ion, m=it's mass and B= magnetic field strength. Due to the fact that the magnetic field strength (B) is constant, then ions of different masses will have unique cyclotron frequencies.

2.4. Infrared absorption spectroscopy

2.4.1. Introduction

The infrared covers the electromagnetic spectrum between 0.78-1000 μm. The wavelength is measured in wave numbers with the units of cm^{-1}. The infrared is divided into three regions as in table 2.1 below

Region	**Wavelength range (μm)**	**Wavenumber range (cm^{-1})**
Near	0.78-2.5	128000-4000
Middle	2.5-50	4000-200
Far	50-1000	200-10
Most used	2.5-15	4000-670

Table 2.1 *The regions of the infrared.*

2.4.2. Principles of IR

2.4.2.1. Molecular rotations

The energy responsible for molecular rotations refers to the radiation of 100 cm^{-1} or less. Due to the fact that rotational levels are quantized, absorption by gases in the far-infrared region is characterized by discrete, well-defined lines. However in ligands or solids these lines broaden into a continuum due to collisions and other interactions.

2.4.2.2. Vibrational transitions

The positions of the atoms in a molecule are not fixed; they are subject to a number of different vibrations and rotations about the bonds in the molecule. For a simple diatomic or triatomic molecule it is very easy to define the number and nature of such vibrations and relate these to energies of absorption. Molecules made up of several atoms are very difficult if not impossible to analyze. Vibrations fall into two main categories of stretching and bending. The former involves a continuous change in interatomic distance along the axis of the bond between two atoms; while the latter are characterized by a change in angle between two bonds and are four types: scissoring, rocking, wagging and twisting.

2.4.2.3. Selection rules

This rule states that transition from energy level 1 to 2 or from level 3 to 4 should be identical to that from 0 to 1 transition. This is given by the equation:

$$E = (v + \tfrac{1}{2})\, h\nu_m, \qquad \text{Equation 2.6}$$

ν_m = vibrational frequency of the classical mode, h=Planck's constant, and v = vibrational quantum number, which can take only positive integer values (including 0). From this equation we learn that quantum mechanical vibrations only take certain discrete energies. The selection rule states that $\Delta v = \pm 1$. Since the vibrational levels are equally spaced, only a single absorption peak should be observed.

2.4.2.4. Anharmonic oscillator

From qualitative considerations the description of a molecular vibration using classical quantum mechanism treatments of the harmonic oscillator appears to be imperfect. The wave equations of quantum mechanics permit the deviation of more nearly correct potential energy curves for molecular vibrations. Qualitatively, the curves must take the anharmonic form shown in Figure 2.5 below. A note should be made that both harmonic and anharmonic curves are nearly alike at low potential energies.

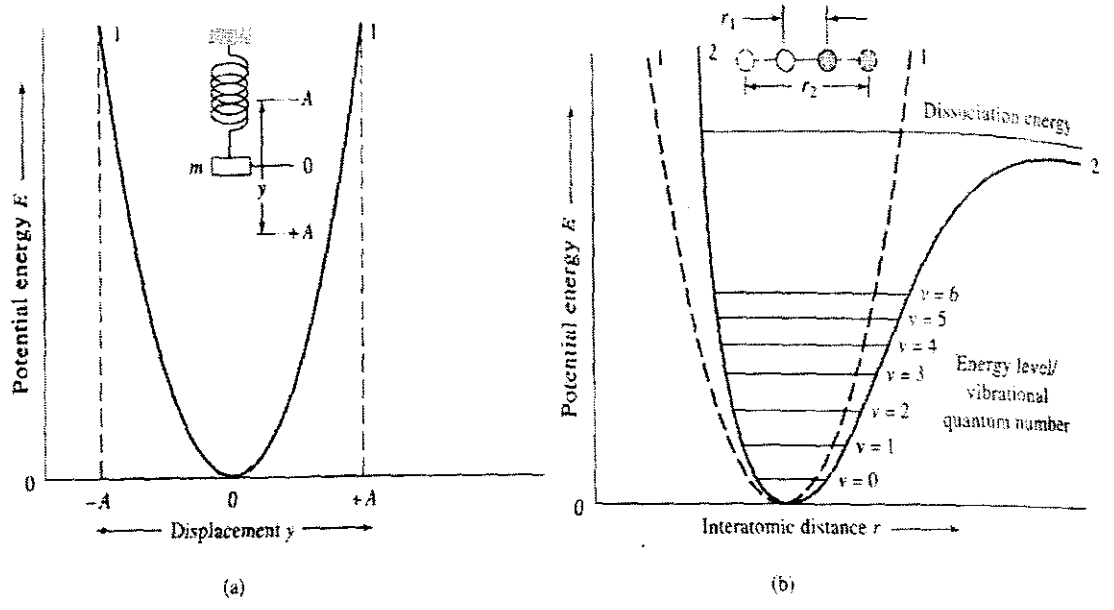

Figure 2.5 *Potential energy diagrams; 1. Harmonic oscillator and 2. Anharmonic oscillator.*

Anharmonicity leads to two types of deviations: at higher quantum numbers, ΔE becomes smaller (curve 2), and the selection rule is not rigorously followed; as a result this disobedience of selection rule, transitions of $\Delta v = \pm 2$ or ± 3 are observed. These are

responsible for the overtone lines observed at frequency 2 to 3 times that of the fundamental line. The intensity of such lines is very low and peaks may not be observed.

2.4.2.5. Vibrational coupling

In addition to the vibrations earlier discussed, interaction between vibrations can occur (coupling) if the vibrating bonds are joined to a single, central atom. Vibrational coupling is influenced by a number of factors:

- Strong coupling of stretching vibrations occurs when there is a common bond between the two vibrating bonds.
- Coupling of bending vibrations occurs when there is a common bond between the groups.
- Coupling between a stretching vibration and a bending vibration occurs if the stretching bond is one side of an angle varied by bending vibration.
- Coupling is greatest when the coupled groups have approximately equal energies.
- Little or no coupling is observed between groups separated by two or more bonds.
- Coupling requires that the vibrations be of the same symmetry species.[5]

2.5. Thermogravimetric analysis

2.5.1. Introduction

Thermogravimetry (TG) is a technique in which the mass of a sample is monitored against time or temperature while the temperature of the sample, in a specified atmosphere, is increased (usually linear with time). This technique is most commonly

called thermogrametric analysis (TGA). The apparatus is called a thermobalance, or thermogravimetric analyzer. A thermogram or a thermal decomposition curve[6] is a plot of mass or mass percent as a function of the temperature.

2.5.2. Principles of TGA

2.5.2.1. The balance

There are many types of thermobalance designs available commercially which are capable of giving quantitative information about samples ranging in mass from 1mg to 100g. The most common balances in use have a range of 5 mg to 20 mg. There are difficulties associated with the operation of a balance used in conjunction with a furnace. These include presence of either oxidizing or corrosive gases near the balance.

2.5.2.2. The furnace

Furnaces in use are generally non-inductively wound electrical resistance heaters, although IR and microwave heating have been suggested. A few important features should be observed in a furnace:

- It should have a zone of uniform temperature which is considerably longer than the sample plus holder.
- The balance mechanism should not be affected by the heat from the furnace
- The furnace should be capable of rapid response and a range of heating to temperatures way above those of interest.
- The lining of furnace should be inert at all temperatures used.

Often the cooling and heating rates of the furnace can be selected from just greater than zero to as high as 200 °C/min.

2.5.2.3. Samples

TGA is frequently carried out in solids. The sample should be obtained in an approved way[7] so that it provides meaningful analysis. Pure and homogeneous compounds are easy to use. Crystalline samples may behave differently from fine powders; this is rifer where surface reactions are involved. Thermoplastics are one example of the materials which is hard to produce a powder. Samples should ideally be small, powdered and spread evenly in the crucible.

2.5.2.4. Atmosphere

The sample needs to be surrounded by an inert or a reactive atmosphere, and to control the evolution of gases from the sample. Generally TGA is conducted under flowing gas stream. Too high a flow will disturb the balance mechanism while too low a flow will not remove product gases or supply reactant gas. Due to this, flow rates of between 10-30 mL/min are often used. The gas flow can also contribute to the transfer of heat and assist the transfer of products to any external gas analysis system.

2.5.2.5. Instrument control/Data handling

Modern thermobalances usually use a computerized temperature control routine that automatically compares the voltage output of the thermocouple with a voltage versus temperature table that is stored in Read-Only Memory (ROM). The computer uses difference between the temperature of the thermocouple and the temperature specified in

ROM to adjust the voltage to the heater. An agreement between the specified temperature program and the temperature of the sample may be established using this method.

2.6. Nuclear Magnetic Resonance

2.6.1. Introduction

Nuclear magnetic resonance or NMR is one of the most widely used analytical tools. NMR is based on the bulk magnetic properties of materials made up of certain isotopes, most notably, protons (^{1}H), but encompassing a wide variety of species including ^{13}C, ^{19}F, and ^{29}Si. NMR is used to measure magnetic fields with exquisite precision and is the basis of MRI-magnetic resonance imaging.

2.6.2. Principles of NMR

2.6.2.1. Nuclear spins

The magnetic properties of the Nuclei were postulated by Pauli[8] to explain the hyperfine structural features of atomic spectra. The rules for determining the net spin of a nucleus are as follows:

- If the number of electrons and protons are both even, the nucleus has no spin
- If the number of neutrons plus number protons is odd, the nucleus has a half-integer spin (1/2, 2/2, 5/2 etc)
- If the number of neutrons and the number of protons are both odd, the nucleus has an integer spin (1, 2, 3 etc)

These rules can be used to predict the magnetic moments, but they are not exact. A nucleus with a spin, I, will have 2I + 1 possible orientations.

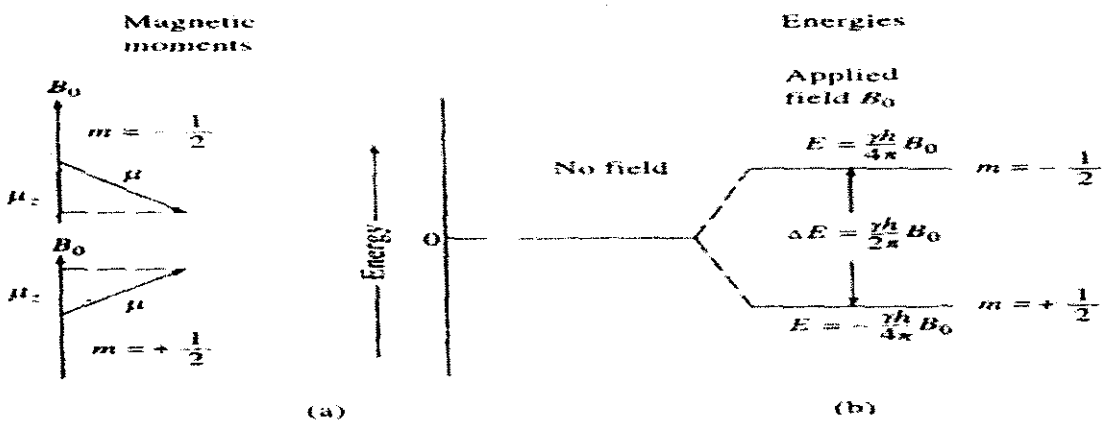

Figure 2.6 *Energy levels and magnetic moments for a nucleus with a spin quantum number of ±½.*

For a nucleus in a magnetic field, the initial population of the energy levels is determined using Boltzmann distribution. This means that the lower energy level will contain slightly more nuclei than higher levels.

2.6.2.2. Magnetization and precession[9]

Imagining a nucleus (1/2 spin) in a magnetic field at lower energy and spinning on its axis. With the presence of a magnetic field, this axis of rotation will precess around the magnetic field. The frequency of precession is termed Langmuir frequency, which is identical to the transition frequency. The potential energy of the precessing nucleus is given by:

$$E = \mu B \cos\theta \qquad \text{Equation 2.7}$$

θ=angle between the direction of the applied field and the axis of nuclear rotation. If energy is absorbed by the nucleus, then the angle of precession, θ, will change.

2.6.2.3. Effects of pulses

Disturbances and detection of nuclear magnetic interaction occur at radiofrequencies due to the precession frequencies of nuclei in the range of 10-100 MHz for the magnetic field of 1-10 Tesla. Precession can occur if the magnetization can be moved away from its equilibrium position and thus a signal can be detected. This displacement of magnetization from the equilibrium is also known as excitation. This excitation is brought about by a second magnetic field, B, which oscillates at the appropriate radiofrequency. This field is indicated in coil wound perpendicular to B_0.

2.6.2.4. Useful nuclei

Knowledge of magnetogyric ratio, γ, and spin quantum number (I) for nuclei allows one to estimate the resonance frequency from the equation:

$$\nu = \gamma B/2\pi \qquad \text{Equation 2.8}$$

where ν is the applied radiation. Resonant frequencies for particular nuclei can be listed at a particular field, which is much more convenient, than noting the exact value of γ. The nuclear moment for any nucleus serves as a pointer towards its sensitivity: the greater the nuclear moment, the larger the energy between transitions for a given applied field.

A nucleus with I=0 have no magnetic moment and thus no NMR properties except that it alters the distribution of electrons in neighbouring nuclei and thus affect their resonance positions. These types include common isotopes of carbon (^{12}C), oxygen (^{16}O) and silicon (^{28}Si). Nuclei with I= ½ are most suitable for NMR.

2.6.2.5. Relaxation

Relaxation causes broadening of the NMR signals, and in extreme cases no signal or effect on the nuclei can be observed. Halides are examples of the extreme cases, which show no NMR effects when covalently bonded. ^{14}N gives rise to an intermediate effect, with broad but observable NMR signals. ^{2}D and ^{11}B, which have got very small quadrupole moments, can be observed in normal manner because their broadening is not excessive.

There are two major relaxation processes:

Spin-lattice: A lattice is a term given to a sample which the nuclei are held. The magnetic field caused by motion of nuclei within the lattice is called lattice field. Some components of lattice field can interact with nuclei in the higher energy state, and cause them to lose energy (returning to the lower state).

Spin-spin coupling: This relaxation explains the interaction between neighbouring nuclei with identical precessional frequencies but differing magnetic quantum states.

2.7. UV/Vis spectroscopy

2.7.1. Introduction

The UV/Vis is primarily the absorption spectroscopy ranging between 160-780 nm. Although this may look very narrow, its importance is vital to life on earth because its interaction with molecules is the primary step both in vision and photosynthesis. Thus the measurements of those molecular interactions form basis of UV/Vis and gives wealth of information about those molecules.

Although the range limits of UV/Vis spectrum is unknown but it is well defined. This, in part, is because most gases absorb appreciably below 185 nm. Measurements in this range therefore needs to be done in evacuated enclosures. This vacuum-UV region is therefore outside the range of most spectrometers. The remaining UV region is loosely divided into near-UV and far-UV regions. These are relative since there is no consensus on where the divide should be, and different authorities place it at various points between 200 and 30 nm.

2.7.2. Principles of UV/Vis

2.7.2.1. Absorption of radiation

When UV/Vis radiation encounters an atom or molecule, an interaction between electrons and the radiation occurs. This results with the attenuation of the radiation and the increase in the energy of the electrons. This is then regarded as a promotion of one of the outer or bonding electrons from ground state into one level higher.

2.7.2.2. Measurements of transmittance and absorbance

The absorbance/transmittance is linearly related to the concentration c of the absorbing analyte by the equation below contained in cell of path length b:

$$A = -\log T = \log P/P_0 = \varepsilon bc \qquad \text{Equation 2.9}$$

T= transmittance, ε= molar absorptivity, and P, P_0 is the radiation power.

This relationship is known as the Beer's law.[10] Under general laboratory conditions A and T cannot be measured because the analyte should be in a completely transparent cell. Beam attenuation is also observed in several ways: two air/wall interfaces and two wall/solution interfaces. Due to this, the power of the transmitted beam by the analyte is usually compared to the power of the beam transmitted by the cell with only the solvent. From this, these variables can then be obtained from the equation:

$$T = P_{solution}/P_{solvent} = P/P_0 \qquad \text{Equation 2.10}$$

$$A = \log (P_{solvent}/P_{solution}) \qquad \text{Equation 2.11}$$

P_0 refers to the power of radiation after it has passed through the cell containing the solvent and P refers to that passing the cell with the analyte.

2.7.2.3. Absorbing species

2.7.2.3.1. Organic compounds

Absorption of radiation in organic compounds is because of the interactions between photons and electrons that either participate directly in bond formation or are localized about such atoms, these may be oxygen, nitrogen, sulfur and the halogens. Single bonds absorb at very low wavelengths because their electrons are tightly bound. In double and triple bonds the electrons are not as tightly bound and are therefore easily excited by radiation. Unsaturated organic functional groups that absorb UV/Vis are known as chromophores. Different transitions are possible in the electrons of a compound as depicted in Figure 2.7 below.

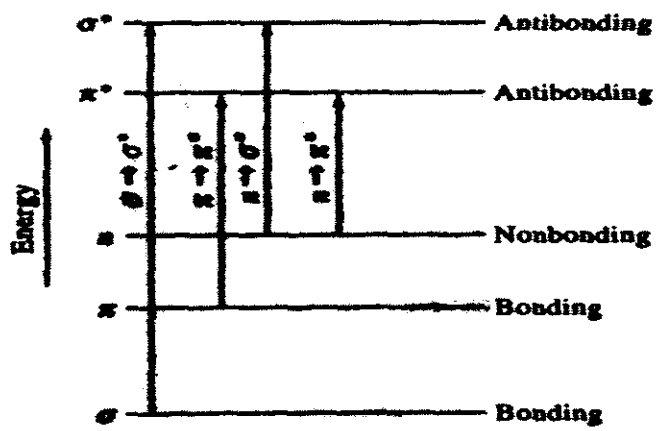

***Figure 2.7** Electronic molecular energy levels.*

2.7.2.3.2. Inorganic compounds

Ions and compounds of elements in the first and second transition series absorb UV/Vis in at least one of their oxidation states.

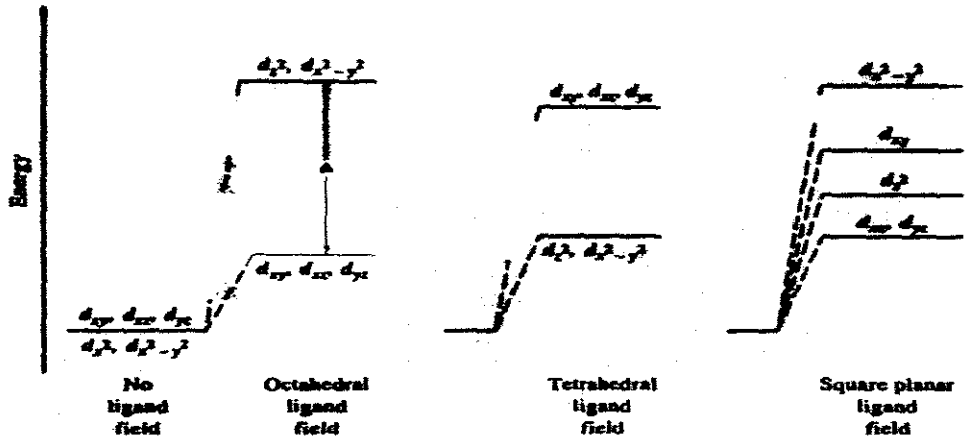

Figure 2.8 *Different energy levels for the d-orbitals; an illustration of the ligand field effect.*

Absorption depends on the transition of an electron from the filled to the unfilled d-orbitals. This process is demonstrated in Figure 2.8 above. The energy differences between the d-orbitals depend on the position of the element in the periodic table, its oxidation state, and nature of the ligand bonded to it. Absorption spectra of ions of actinides and lanthanides are totally different from those of d-ions. The electrons responsible for this are 4f and 5f.[11]

2.7.2.3.3. Charge-Transfer absorption

Inorganic complexes that exhibit this feature are called charge-transfer complexes. A charge-transfer complex consists of an electron-donor group bonded to an electron acceptor. When the radiation is absorbed, the electron from donor is transferred to an orbital largely associated with the acceptor.

2.8. Scanning Electron Microscopy with Energy Dispersive X-ray Analyzer

2.8.1. Introduction

Generally 3 techniques can be used to obtain high resolution surface information i.e. scanning electron microscopy (SEM), transmission electron microscopy (TEM) and atomic force microscopy (AFM). SEM equipped with energy dispersive X-ray analyzer (EDAX or EDX) is by far one of the most used tools for the study of both morphology and composition of materials. Morphology or topography of a specimen can be obtained by scanning an electron probe across the surface of the specimen. Even at very low magnifications, high-resolution pictures are always obtained.

2.8.1.1. Electron optics

Magnetic condenser and objective lens system serves to reduce the image to a final spot size on the sample of 5-200 nm. SEM scanning is accomplished by the two pairs of electromagnetic coils located within the objective lens: One pair deflects the beam in the x direction across the sample, and the other pair deflects in the y direction. An electrical signal is applied to one of the pairs to control the scanning. The variation of the signal as a function of time, the electron beam is moved in a straight line across the sample and returned to the signal position. After the completion of this line scan the other set of coils (y coils) is used to affect the beam slightly.

The image of the sample is produced by using the output of a detector to control the intensity of the spot on the CRT. This scanning method produces a map of the sample in

which there is a one-to-one correlation between the signal produced at a location on the sample surface and a corresponding point on the CRT display.

2.8.1.2. Electron source

The electron beam comes from a filament, made of various types of materials. The most common is a loop of Tungsten which functions as a cathode. A voltage is supplied to the loop, causing it to heat up. The anode, which is positive with respect to the filament, forms powerful attractive forces for the electrons. This causes electrons to accelerate towards the anode. Some of the electrons accelerate right by the anode and down the column, to the sample.

After the electron beam hits the sample, producing secondary electrons from the sample. These electrons are scattered by a secondary detector or a backscatter detector, converted to a voltage, and amplified. The amplified voltage is applied to the grid of the CRT and causes the intensity of the spot of light to change. The image consists of thousands of spots of varying intensity on the face of the CRT that corresponds to the topography of the sample. There are several other types of filaments including Lanthanum Hexaboride filaments and Filed Emission guns.

2.8.1.3. The interaction of electron beams with solids

2.8.1.3.1. Elastic scattering

When the electron collides elastically with an atom, the direction changes but the speed is not affected, so that the kinetic energy of the electron remains essentially constant. The deflection is random and can vary between 0-180°. Some of the electrons, however, eventually lose energy by inelastic collisions and remain in the solid. The majority undergoes numerous collisions and as a result eventually exits from the surface as backscattered electrons. A note should be made that the backscattered electrons have a much larger diameter than the incident beam (1000 times). This diameter acts as one factor that limits the resolution of an electron microscope.

2.8.1.3.2. Secondary electrons production

When a solid surface is bombarded with an electron beam having energies of several keV it is observed that electrons having energies of 50 keV or less are emitted. Generally the number of these secondary electrons is 1/5 or less of the number of backscattered electrons. These electrons are produced as a result of interactions between the energetic beams electrons and weakly bound conduction electrons in the solid. Secondary electrons are produced from the depth of only 50-500 Å and exit in a beam that is slightly larger in diameter than the incident beam.

2.8.2. General principles of SEM

2.8.2.1. Principles of SEM (with BSE and SE detectors)

An electron beam is produced by the electron gun at the top of the SEM column under high vacuum. The focused beam is either focused on a grain of a sample or is scanned across the entire sample surface in a raster pattern. The raster pattern is similar to that in the cathode ray tube (CRT), in which the electron beam is: i. swept across the surface in a straight line (x direction), ii. Returned to its starting position and, iii. Shifted downwards (y direction) by a standard increment. This process is repeated until the desired area has been covered. During this process, a signal received above the surface (z direction) and stored in the computer, where it is converted into an image. The sample interacts with the electron beam and further produces other signals.

These signals include X-rays, secondary electrons (SE), backscattered electrons (BSE), Auger electrons and cathodoluminescence. The scanning electron microscope generally is equipped with BSE and SE. EDX detectors are also fitted into scanning electron microscopes when microanalysis is to be acquired. BSE production varies proportionally with the average atomic number of the sample. For higher average atomic number materials, the image of the sample will appear brighter than low average atomic number materials on a SEM image. Production of the scanning electrons leaves the atom with very low energy (5 eV) when incident beam strikes the atom. This low energy means that only scanning electrons that are very close to the surface can exit the sample and be examined. Scanning energy images can show very good topographic effect of particles and display details of surface irregularities much better.

2.8.2.2. Principles of EDAX

The de-energization of the sample atoms after secondary electrons are produced causes the X-rays. Secondary electrons are low energy electrons and since they leave the surface, a lower energy shell then has a vacancy. An electron with a higher energy can then fall into the lower energy shell, thus filling the vacancy. This 'falling' electron emits X-rays. These X-rays have a characteristic energy that is unique to the elements from which they originate. The EDX detector then detects these signals, sends them into the EDX analyzer that sorts the signals into the different elements present in the sample, and into X-ray count for each element. These X-ray counts are resolved and displayed as peaks corresponding to the elements in the sample.

2.9. Transmission Electron Microscopy

2.9.1. Introduction

Materials of TEM must be specially prepared to thicknesses that can allow electrons to transmit through the sample, much like light is transmitted through materials in conventional microscopy. Because the wavelength of electrons is much smaller than that of light, the optimal resolution attainable for TEM images is many orders of magnitude better than that from a light microscope. TEMs can reveal the finest details of internal structure-in some as small as individual atoms. Magnifications of 350 000x can be routinely obtained for many materials, whilst in special instruments, atoms can be imaged at magnifications of >150 million.

2.9.1.1. TEM illumination

2.9.1.1.1. Electron source

The illumination is based on self-biasing electron gun. The system is composed of an electron gun that has a hot wire filament and a Wahnelt shield. The filament leads to the formation of thermionic emissions of electrons. The filament and shield called the cathode, are then set to a very high electric potential between 25 000-125 000 V. This then gives the incentive for the electrons to move. The electrons will be accelerated towards the grounded anode if not for the bias shield as the filament heat is turned up.

Surplus electrons collected at the shield making the shield more negative, which in turn inhibit the release of more electrons.[12] This process is known as self-biasing and is controlled by the bias resistor. If there were no resistors in the circuit, the electrons will flow out of the cathode uninhibited. The filament heat is brought up to a point where equilibrium exists between the filament and the shield. This process is called saturation, and will vary with different bias settings.

Once saturation state is reached, there will be no further increase in electron beam current as the heat is increased. A good beam current is about 10 μA. The higher the beam current the shorter the life of the filament, also the more damage to the specimen by the electron beams.

2.9.2. Principles of TEM

When an electron beam strikes the sample it can either bounce off elastically, that is, without loss of energy, or inelastically, where some of its energy is transferred to the atoms. If the electron bounces inelastically, its energy will remain constant and the angle of the bounce can be determined. This electron can be used to give high resolution information on the sample. The image is formed from electrons which pass through the specimen that hits the photographic film. The contrast arises if there is interference between electrons coming from different angles.

If a small objective aperture is used, electrons that get at greater angles are blocked, and the contrast of the image is enhanced. On the other hand, electrons with high deflection contain high resolution information and are therefore lost. A balance between the two should be established, so that both a good contrast and high resolution are obtained. Due to the fact that electrons pass through the sample before hitting the photographic screen, they contain information on the inside structures of the sample being analyzed. The darkness of the resultant image is proportional to the electron absorbency properties of the material used.

2.10. Ellipsometry

2.10.1. Introduction

Ellipsometry is a versatile non-destructive technique that has applications in many different scientific fields. Ellipsometry is a sensitive measurement technique and it provides unequalled capabilities in thin film metrology. This technique is often used to

characterize thickness for sample layer or complex multilayer stacks ranging from a few angstroms to several microns with excellent accuracy. It measures the change in the state of polarization of the light reflected off the film's surface.

The technique relies on the fact that the reflection at a dielectric interface depends on the polarization of the light, while the transmission of light through a transparent layer changes the phase of the incoming wave depending on the refractive index of the material. Although measurements of the state of polarization of a light wave is important on its own right, Ellipsometry is generally conducted in order to obtain information about an optical system that modifies the state of polarization.[13] A lot more properties can be extracted from ellipsometric measurements

Optical: Refractive index (n) and coefficient of extinction (k)

Materials properties: composition/crystallinity, microstructure and film uniformity by area and depth.

2.10.2. Principles of ellipsometry

A general scheme representation of the ellipsometry measurement is presented in Figure 2.9

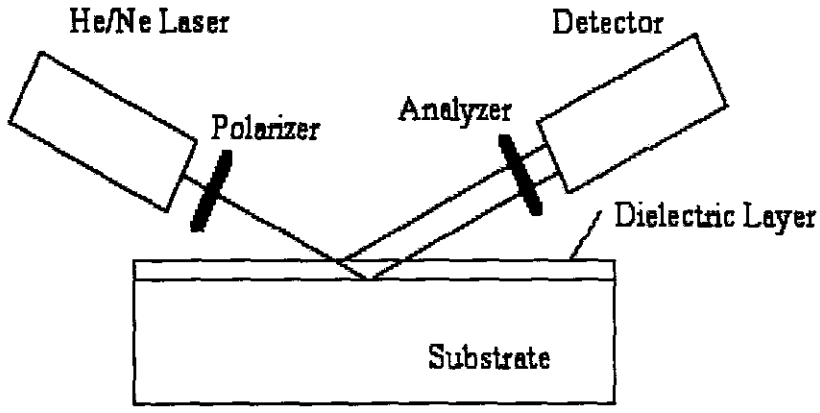

***Figure 2.9** A schematic representation of an ellipsometer.*

The laser produces a well collimated or quasi-monochromatic beam from a suitable light source (He/Ne) and is passed through a variable polarizer to produce light with known controlled polarization. This light interacts with the optical system (dielectric layer) and its polarization is modified. The modified state of polarization at the output of the system is measured (analyzed by a variable polarization analyzer) then followed by a photodetector.[14,15] The interaction between the light wave and the optical system is assumed to be linear and frequency conserving. The state of polarization of the light is modified by one or a combination of the following factors.

1. **Reflection or refraction:** This occurs at the interface between optically dissimilar media, the state of polarization is changed abruptly.
2. **Transmission:** The state of polarization changes non-stop as light progresses through a medium that exhibits optical anisotropy (refractive, absorptive or both).
3. **Scattering:** This occurs when light wave transverses a medium with spatially inhomogeneous index of refraction caused by the presence of scattering centers as in aerosols and emulsions. Scattering is usually accompanied by a distribution of the scattered energy over a wide range of solid angles.

2.10.3. Data analysis

The ellipsometer measures Psi and Delta ($\Psi$and Δ) usually as a function of wavelength and the angle of incidence, these factors are used to describe a change in light's polarization state caused by its interaction with a sample. This technique is a model dependent technique, which means it's not possible to directly measure the physical quantities in question. Therefore due to this limitation a mathematical model is required to determine these properties. A stepwise procedure as illustrated in Figure 2.10:

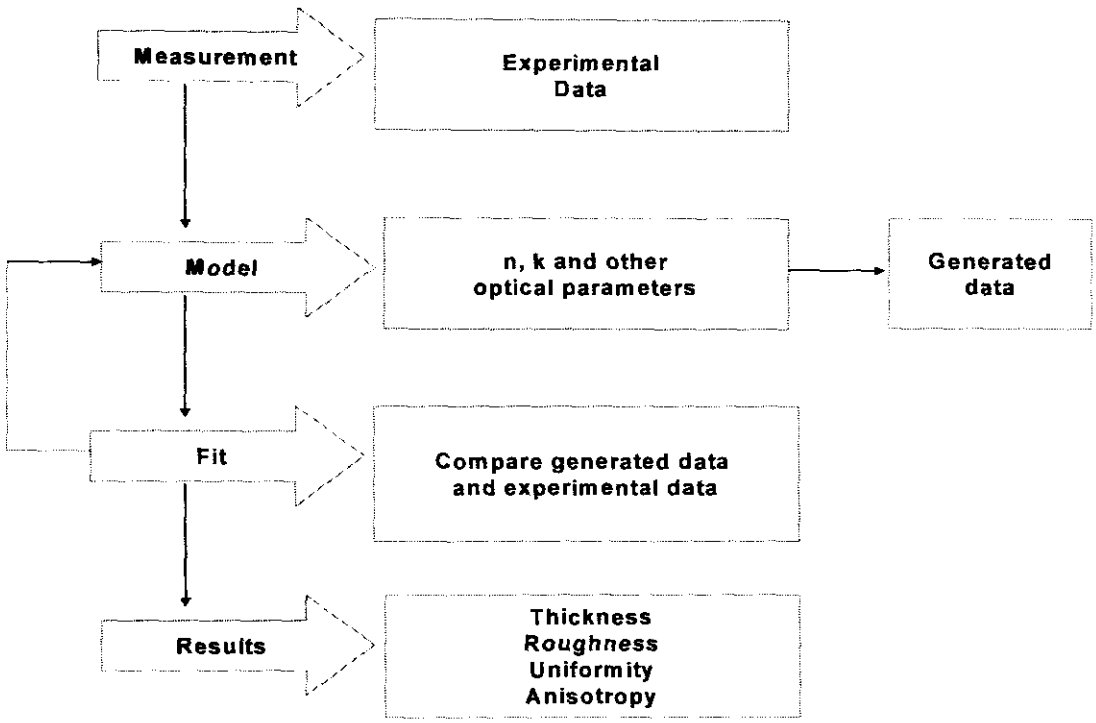

Figure 2.10 *Key steps in the derivation of information from the ellipsometry.*

1. Experimental measurements to acquire Ψ and Δ as a function of wavelength and angle of incidence.
2. Building a model that describes the sample structure using as much as information about the sample as possible. All layers of the sample should be accounted for.
3. Generating theoretical data from the optical model that corresponds to the experimental data. This is followed by comparing the experimental data with the generated data. The unknown parameters in the optical model, such as thin film thickness or optical constants or both, are varied to produce the best fit to the experimental data. Mathematical regression algorithms (least squares) are used to

vary unknown parameters and minimize the difference between the generated and experimental data.

4. Physical parameters of the sample such as thickness, composition, surface roughness, anisotropy, optical constants, interfacial regions, etc can be obtained once a good fit to the experimental data is achieved.

There are a few advantages of using ellipsometry for such information acquiring, these include: ellipsometry is highly accurate and reproducible (even in low light levels), no reference sample is required, it's not susceptible to scattering, lamp or purge fluctuations and it has got increased sensitivity, especially to ultra thin films (<100 nm).

2.11. References

1. Azaroff L.V.and Buerger M.J., The powder method. New York: McGraw-Hill Book Company, 1958.
2. *Powder Diffraction-Inorganic Compounds,* JCPDS International Conference for Diffraction Data, Philadelphia, 1984
3. Jeffrey J.W., *Methods in X-Ray crystallography,* London: Academic Press, 1971
4. Comisorow M.B., *J. Chem. Phys.*, 1978, **69**, 4097
5. Cotton F.A., *Chem. App. Of Group Theory*. NY: Wiley, 1971
6. Fifield F.W. and Kealey D., *Analytical Chemistry*, 2nd edition, Blackie, Glasgow, 1990
7. Pernicone N. and Traina F., *Pure. Appl. Chem.*, 1978, **50**, 1169
8. Pauli W., *Naturwissenschaften*, 1924, **12**, 741

9. Sanders J.K.M., *Modern NMR Spec.*, NY: Oxford Press, 1989

10. Knowles A. and Burgess C., *Prac. Abs. Spec.*, NY: Chapman and Hall, 1984

11. Skoog D.A., West D.M. and Holler F. J., *Analytical Chemistry*, 7th ed., NY: Saunders College Publishing, 1991

12. Misell D.L., *Developments in Electron Microscopy and analysis*, 1977, Series number 36.

13. Azzam R.M.A. and Bashara N.M., *Ellipsometry and Polarized light*, North-Holland Physics Publishing, Amsterdam, 1988, p153

14. Cohen M.H., *Proc. IRE*, 1958, **46**, 172

15. Suzuki S. and Tsuchiya A., *Proc. IRE*, 1958, **46**, 532

CHAPTER 3:

DEPOSITION OF RUTHENIUM AND RHODIUM SULFIDE THIN FILMS USING AEROSOL ASSISTED CHEMICAL VAPOUR DEPOSITION (AACVD)

3.1. *Introduction*

Chemical Vapour Deposition (CVD) is a relatively mature technique. The oldest example of CVD, since prehistoric times, is the formation of soot due to the incomplete oxidation of firewood. In the 19th century CVD was developed as an economically viable industrial process in the fields of high purity refractory materials such as Ti, Ni and Ta. De Lodiguine's[1] patent literature is perhaps one that describes the initial industrial exploitation of CVD techniques. It is in the past 40 years that an in-depth understanding of the processes and the ever increasing applications has been well investigated.

AACVD is a variant of CVD based on the use of aerosol precursors. The aerosol of the volatile precursor is carried by a carrier gas, e.g. O_2, N_2 and Ar, from the humidifier into the heated zone. In this zone the solvent will rapidly evaporate or get combusted, the aerosol precursor undergoes subsequent decomposition and /or chemical reaction near or at the heated substrate surface to deposit the desired material. The decomposition/chemical reaction conditions should be optimised such that the decomposition occurs at or near the substrate (heterogeneous) and not in the gaseous phase (homogeneous). This avoids the formation of powdery deposits which may result in haziness in the film.

The deposition rate is largely determined by the substrate temperature and gas flow rate. If the substrate temperature is too low, carbon occlusions are found in the films as a result of incomplete oxidation of the organic materials and also low or no growth is observed. If the temperature is too high, excessive diffusion of surface impurities during film growth can occur. The gas flow and system geometry determine the uniformity of the films deposited over a reasonably large area. Due to this, it is then important to introduce the gas into the reaction chamber in a controlled manner both in terms of gas inlet location and flow rate. Fiest[2] discussed the number of reactor designs for CVD for the growth of homogeneous and uniform films.

The use of AACVD is advantageous in a number of ways:

- The vapour precursor generation and delivery method are simplified, and therefore lowers the cost of operation.
- AACVD largely uses single source precursors, which provides good molecular mixing of chemical precursors which allows synthesis of multicomponent materials with well controlled stoichiometry.
- It allows rapid formation of the deposited phases at relatively low temperatures due to the small diffusion distances between reactants and intermediates.
- It is a low cost process compared with the conventional CVD because AACVD process can be performed in an open atmosphere for the deposition

of oxides and less oxygen sensitive non-oxide materials without the need of sophisticated reactor and/or vacuum system.

For the deposition of a high quality materials of choice the relationship between the process parameters, CVD phenomena and the film properties should be studied and understood. Table 3.1 shows some of these dynamics which should be considered for any CVD process being undertaken.

Process Parameters	**Thin film properties**	**CVD phenomenon**
Precursor type	Deposition rate	Chemical kinetics
Deposition temperature	Microstructure	Mass transport
Flow rate	Composition	Thermodynamics
Deposition time	Uniformity and adhesion	
	Stoichiometry	

Table 3.1 *Some of the relationships that are established, between process parameters, thin film properties and the CVD phenomenon.*

The use of single source precursors is obviously the most advantageous in this type of thin film deposition. The use of bis(dialkyldithiothio-/diseleno carbamato) M (II) complexes as single source precursors for the deposition of metal chalcogenide materials has been reported in literature.[3-5] Decomposition of the metal dithiocarbamates has been studied to give metal chalcogenides (ME)[6] and have been employed extensively to deposit thin films.[7-10]

3.2. Synthesis of single source molecular precursors

A series of single source molecular precursors were synthesized, some with success and others unsuccessfully. A list of these attempted preparations is listed in Table 3.2 below.

Precursor (expected formulation)	**Sample code**	**Colour**
$[Ru(S_2CNEt_2)_3]$	**A1**	Black
$[Ru(S_2CNMeHex)_3]$	**A2**	Black
$[Ru(S_2CN^iPr_2)_3]$	**A3**	Black
$[Ru(S_2CN^tBu_2)_3]$	**A4**	Black
$[Rh(S_2CNEt_2)_2]$	**B1**	Orange
$[Rh(S_2CNMeHex)_3]$	**B2**	Orange
$[Rh_3[S_2CN^iPr_2]_3Cl_6]$	**B3**	Dark orange
$[Rh(S_2CN^tBu_2)_3]$	**B4**	Light orange

Table 3.2 *Attempted syntheses of the precursors.*

3.2.1. Synthesis of metal dialkyldithiocarbamates.

These complexes were synthesized by employing the method illustrated in Figure 3.1 below. The differing aspect for all the preparation was the dialkyl group for each individual complex, which is achieved by varying the amine. Table 3.3 shows the reaction parameters and reagents.

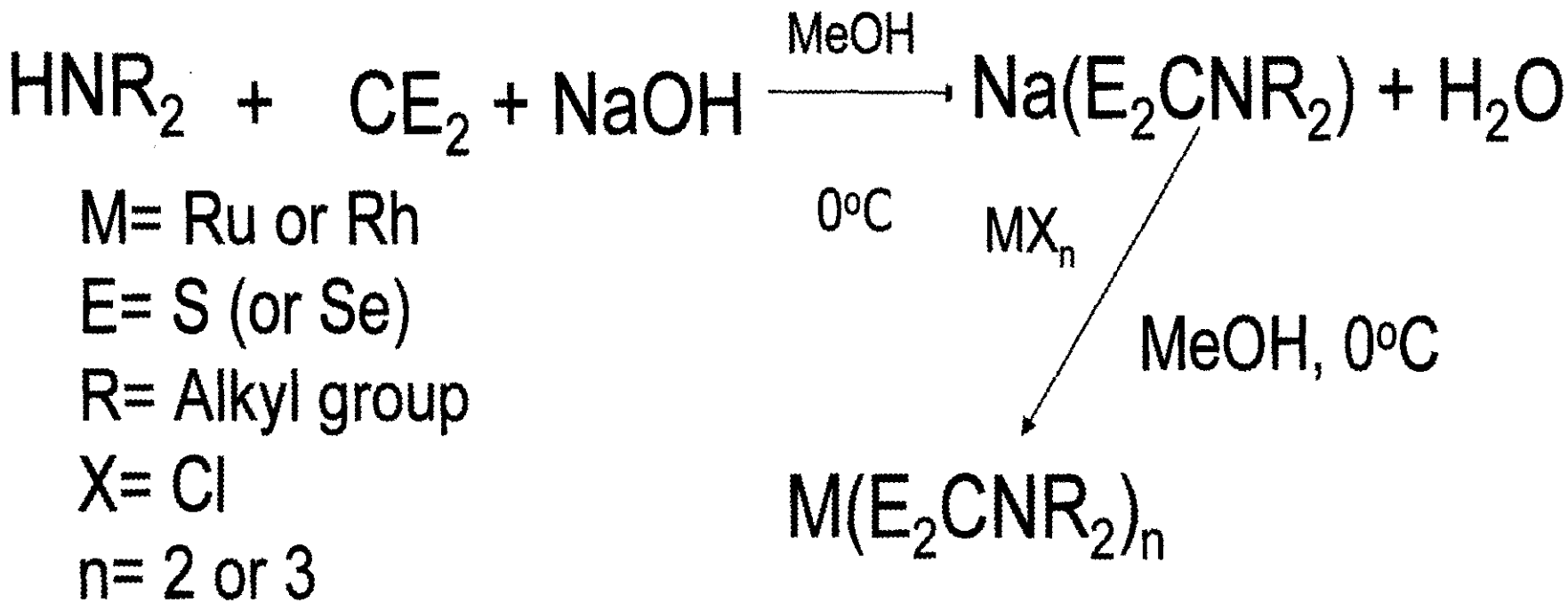

Figure 3.1 *The formation of the metal dialkyldithiocarbamate complexes of Ru and Rh.*

Complex Code	Metal salt (amount)	NaOH (amount)	CS_2 (amount)	Amine (amount)
A1	$RuCl_3.H_2O$ (16.87 mmol)	(50.62 mmol)	(50.62 mmol)	Et_2NH (50.62 mmol)
A2	$RuCl_3.H_2O$ (14.46 mmol)	(43.38 mmol)	(43.38 mmol)	MeHexNH (43.38 mmol)
A3	$RuCl_3.H_2O$ (9.64 mmol)	(28.93 mmol)	(28.93 mmol)	$^iPr_2NH$ (28.93 mmol)
A4	$RuCl_3.H_2O$ (4.82 mmol)	(14.46 mmol)	(14.46 mmol)	$^tBuNH_2$ (14.46 mmol)
B1	$RhCl_3.H_2O$ (3.11 mmol)	(9.32 mmol)	(9.32 mmol)	Et_2NH (9.32 mmol)
B2	$RhCl_3.H_2O$ (4.78 mmol)	(14.34 mmol)	(14.34 mmol)	MeHexNH (14.34 mmol)
B3	$RhCl_3.H_2O$ (2.39 mmol)	(7.17 mmol)	(7.17 mmol)	$^iPr_2NH$ (7.17 mmol)
B4	$RhCl_3.H_2O$ (4.78 mmol)	(14.34 mmol)	(14.34 mmol)	$^tBuNH_2$ (14.34 mmol)

Table 3.3 *Synthesis of the single source molecular precursors*

3.2.2. Results and discussion for the complexes

Initial characterization was conducted on these compounds. Several properties were expected from these compounds as for any dithiocarbamate complexes. The analysis included elemental compositions, ^{1}H-NMR, IR and Mass spectroscopy. The elemental percentages were done first and followed by the rest if they appeared workable. The IR assignment for the CN bond is expected to be different from that of amines, which is located at 1250-1350 cm^{-1}.[11]

Chatt *et al*[12] were the first to report that the CN of dithiocarbamates exhibit a band of medium to strong intensity in the region of 1480-1550 cm^{-1}; between the ranges of C-N and C=N. This has been assigned to CN stretching, where CN bond order is between 1 and 2 due to the resonance shown below.

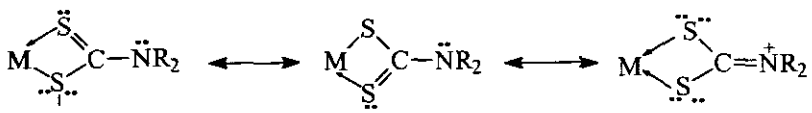

Figure 3.2 *The resonance structures of the CN bond.*

Discussions on NMR trends of the dithiocarbamate complexes were first done by Pandey *et al* [13] when studying the dithiocarbamates of transition metals. A summarised discussion of the results is presented next.

A1.

A black powdery precipitate was obtained with high yields. Initial characterization was then performed on the product. This formulation requires 33.00 % C, 5.54 % H and 7.69 % N; 31.64 % C, 5.53 % and 7.19 % N were found. This result showed a close correlation to the expected results and further analysis was done to confirm the actual formulation of **A1.** The IR assignments for CN bond was at 1458 cm^{-1} with medium intensity.

The ^{1}H-NMR of the compound showed a good correlation to the expected patterns of such a complex. The resonances were as follows:

σ (1.40, t, J = 7 Hz, CH_3)

σ (3.95, q, J = 7 Hz, CH_2)

These were obtained in $CDCl_3$ and were in agreement with the normal resonances for both the methyl and methylene groups. The mass spectroscopy results showed a strong peak (100 %) at 546 m/z which corresponds to the $(M - 1)^{+}$ ion.

A2.

This compound was obtained in a form of a paste and was reduced in volume and washed with MeOH and hexane. After evaporating in air further characterization was done on the complex. The elemental percentages were found to be far less than expected. The expected values were C 42.77, H 7.18 and N 6.23 but the complex showed C 20.60, H 3.60 and N 2.72. Already this complex showed a different formulation from the expected one.

Notably the values for the analysis showed that they were half of the expected values and NMR was also conducted. The resonances on the ^{1}H-NMR showed obvious correlation to the expected ones. A series of complex multiplets were spread from 1.50 ppm to 4.01 ppm. No immediate correlation seemed possible. The infrared was run using Nujol and the expected absorption of the CN was not observed at the normal region for dithiocarbamates.

A3.

The black compound was obtained at very high yields. The calculated elemental composition of this compound is C 40.1, H 6.7 and N 6.7 and the values found were C 15.23, H 2.833 and N 1.99. Clearly the values showed that the expected compound was not synthesized. On the mass spectrum there was no ions corresponding to the expected M^{+} or any other fragment that could be associated with this structure.

A4.

This compound was obtained as a black powdery product. The expected elemental composition of the compound was C 45.41, H 7.62 and N 5.88 the results found were C 7.81, H 2.78 and N 0.97. These were way off the expected values and IR and proton NMR also showed no sensible formulation of this product.

B1.

The orange powdery compound was obtained at relatively low yields and was analysed as follows. The elemental composition was found to be C 30.45, H 5.08, N 6.91 and the

calculated values were C 30.07, H 5.05 and N 7.01. These were in agreement with the expected values and further analysis was conducted to further ascertain the composition of the compound. The ^{1}H-NMR was conducted and the resonances were found as follows: σ 1.23 (2H, q, J = 7 Hz, CH_2) and σ 3.65 (3H, t, J = 7 Hz, CH_3). The infrared was run as a KBr pellet and the assignment for the CN absorption was located at 1496 cm-1, with a strong intensity. The mass spectroscopy measurement was conducted to locate a peak at m/z 398 corresponding to the $(M-1)^+$ of the molecular ion (M^+).

B2.

The pasty precipitate was reduced in size and washed before being evaporated and initial analysis done. The elemental composition of this compound was in good agreement with the expected one. The values expected were C 42.77, H 7.18, N 6.23 and the found values were C 41.45, H 6.89 and N 5.84. From this result, this complex conforms to the expected product.

The ^{1}H-NMR of the compound was done, complex multiplets were observed at σ 3.80, 3.45 and 3.2 ppm and very broad peaks were observed at σ 1.25 and 1.60 ppm. These resonances did not correspond to the expected ones. The methyl protons were expected to show a very distinct singlet at the range of 3.20 ppm since they do not couple with any other protons. The mass spectrum showed no ion for this compound and there were no absorption that could be attributed to the CN group in the IR region.

B3.

The initial characterization was done on the dark orange powdery product. The elemental composition was found to be C 21.97, H 3.77 and N 1.95 whereas the expected composition for the complex was C 36.01, H 6.20 and 6.15. The values found were too low compared with expected ones and they seem to b contaminated from the free ligand ions. Further analysis showed no coherence to the expected result.

B4.

The elemental composition of this complex was found to be C 18.20, H 3.67 and N 3.59 for the formulation to be satisfied the values should be C 42.25, H 7.09 and N 5.48. The result showed a marked difference from the accepted result if this complex was to be as expected. Further analysis showed no consistency with expected result.

From the above results it was observed that only two complexes, that is, **A1** and **B1** were good enough for further use in this work and they were used in the deposition of the thin films as well as nanoparticles (discussed later on) of the metal sulfide.

3.3. Deposition of RuS_2 using $[Ru(S_2CNEt_2)_3]$

3.3.1. Introduction

The chemistry and properties of transition metal dithiocarbamates (dtc) has been studied extensively.[14-19] The complexes follow very simple preparation methods. These metal chalcogenide complexes demonstrate elongated stability under normal conditions. The crystal structure of tris(N,N-diethyldithiocarbamato) ruthenium (III),

$[Ru(S_2CNEt_2)_3]$ was established by Pignolet[20]. These complexes have been found to be stereochemically nonrigid.[21] Figure 3.3 depicts the crystal structure for $[Ru(S_2CNEt_2)_3]$.

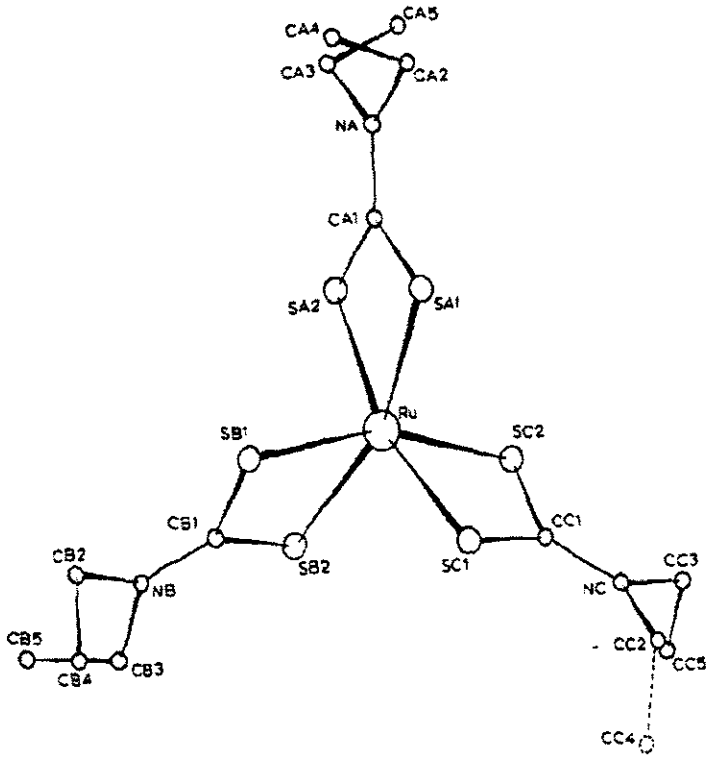

Figure 3.3 *The crystal structure of* $[Ru(S_2CNEt_2)_3]$.[20]

The geometry of $[Ru(S_2CNEt_2)_3]$ has been described comparing the octahedral (O_h) and trigonal prismatic (TP) geometries. Angular structural parameters on the RuS_6 core[20] were studied and the twisted trigonal prismatic geometry was observed as the most dominant geometry.

3.3.2. Synthesis of $[Ru(S_2CNEt_2)_3]$

CS_2 (50.62 mmol) was slowly added into a mixture of NaOH (50.62 mmol) and diethylamine (50.62 mmol) in 50 mL MeOH at 0 °C with constant stirring. The yellow mixture was reacted with a cold MeOH solution of $RuCl_3 \cdot nH_2O$ (16.87 mmol). The black precipitate was refrigerated overnight, filtered, washed with MeOH and then with hexane. The resulting black powdery product was dried in air.

3.3.3. Deposition of RuS_2

0.2 g of the precursor $[Ru(S_2CNEt_2)_3]$ was dissolved in 20 mL toluene in a two-necked flask. Eight glass substrates, with dimensions of 1x 2.5 cm, were placed inside the reactor tube. The Platon gauge was used to control the carrier gas flow at 200 mL/min. The flask was then placed in the water bath over the ultrasonic humidifier. The precursor aerosol was generated and metered into the heated zone by the nitrogen carrier gas. The precursor evaporated and decomposed at the substrate surface, depositing the film on glass substrate.

After 2 hours the precursor supply was terminated and the substrate was heated for further 10 minutes to remove any traces of organic matter in the system. The resulting film was cooled to room temperature and stored in air tight container, and further characterization was conducted.

3.3.4. Results and discussion

$[Ru(S_2CNEt_2)_3]$ has been synthesized and found to be a good starting material for the deposition of the RuS_2 thin films. The ^{1}H-NMR showed a triplet at 1.40 ppm corresponding to the $-CH_3$ protons and a quartet at 3.85 ppm assigned to $-CH_2$. The integration of 1.6:1 was obtained which conforms to the proton ratios. Previous reports are well in agreement with this observation.[22] The full description is given in 3.2.2.

The TGA spectrum in Figure 3.4 shows the decomposition patterns of this complex. The decomposition starts just above 200 °C and continues smoothly up to values close to 300 °C. About 45 % of the precursor weight is lost during this temperature range. From 300-370 °C a total of 60 % weight is lost and then a steady decomposition is observed up to temperatures higher than 500 °C; where the final decomposition product is obtained as a residue. Although the decomposition starts at relatively low temperatures (200 °C), very little to no growth is observed when the decomposition is attempted at such temperatures for the deposition of the thin films.

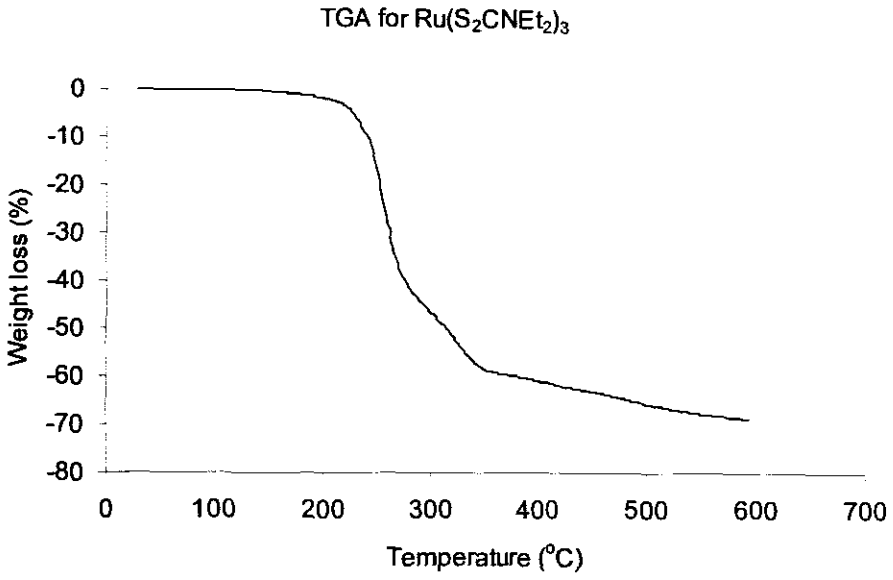

Figure 3.4 *The TGA spectrum for the complex, $[Ru(S_2CNEt_2)_3]$*

3.3.4.1. Structural properties

Ezzouia, *et al*[23] was the first to deposit RuS_2 materials on SiO_2 and Al_2O_3 substrates. The EDAX spectrum (Figure 3.5) ran between 0-20 keV shows the peaks for both ruthenium (Ru) and sulphur (S) confirming the presence of the components of the thin film.

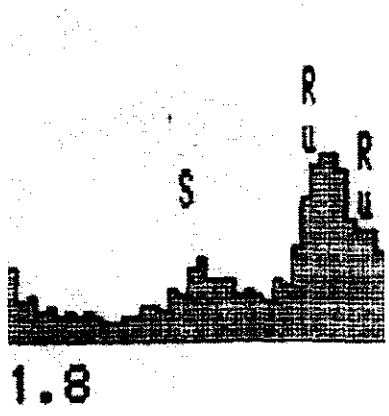

Figure 3.5 *The EDAX image for the RuS_2 thin films.*

The surface morphology of the thin film prepared at 350 °C is shown in Figure 3.6.

Notably there are growth centres that protrude on the surface of the film. Generally in such reactions, the morphology of the film is largely affected by the nature of the reaction and the activation mechanism. Temperature is one other major factor in this property, more especially if it too high or too low. These growth centres that are observed are due to low surface mobility on the film-substrate interface. The diffusion of the intermediate species is low and thus preventing these species from migrating to more energetic sites where growth will occur at a wider area. This type of growth is referred to as amorphous. A side view image in Figure 3.6 B shows the humps that are observed as protrusions from the surface of the film.

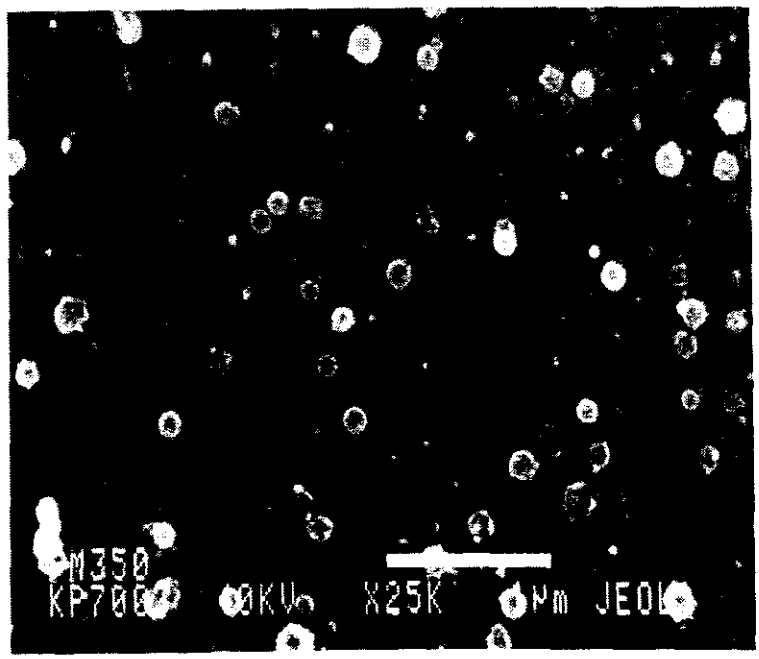

Figure 3.6A *SEM top view micrograph of the* RuS_2 *thin films prepared at 350 °C*

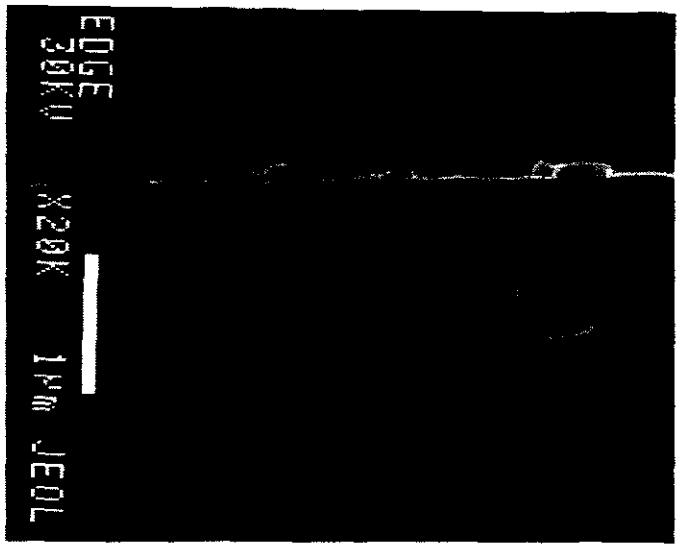

***Figure 3.6B** A side view SEM micrograph of the RuS_2 thin films prepared at 350 °C*

RuS_2 prepared at 450 °C shows a much more uniform surface. The surface morphology patterns of RuS_2 (450 °C) is showed in Figure 3.7. A uniform polycrystalline film was obtained. Polycrystalline growth involves nucleation at different substrate sites and then leading to the growth of islands, coalescing to form a polycrystalline layer. Fine and randomly oriented grains are observed which are termed equiaxed structure.

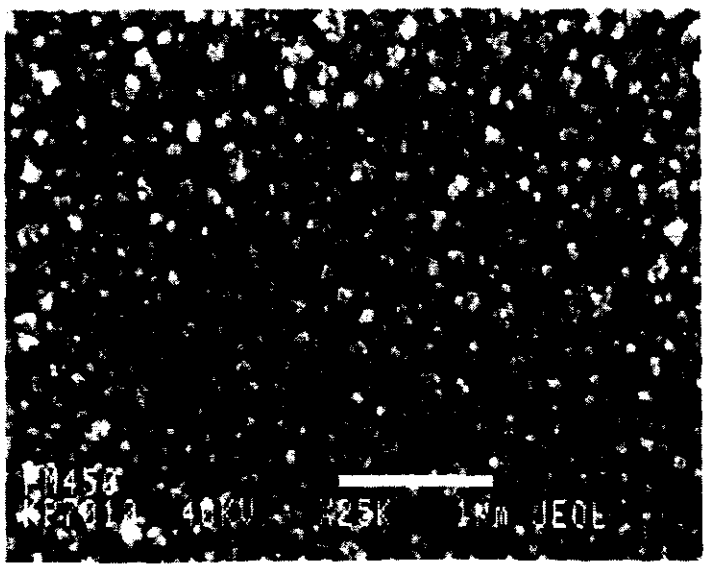

***Figure 3.7A** Top view SEM micrograph of RuS_2 deposited at 450 °C.*

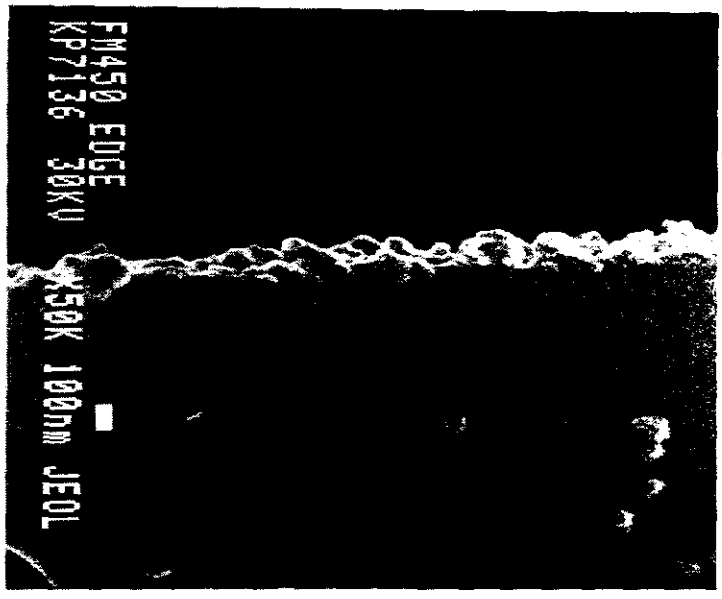

Figure 3.7B *Side view SEM micrograph of RuS_2 deposited at 450 ^oC.*

Grain sizes ranges between 0.0951 – 0.171 μm with a few grains of sizes up to 0.21 μm. Figure 3.7B illustrates the side view image of the thin film. The film thickness was measured to be 382.39 nm (0.382 μm) respectively. The growth rate translates to 3.19 nm/min.

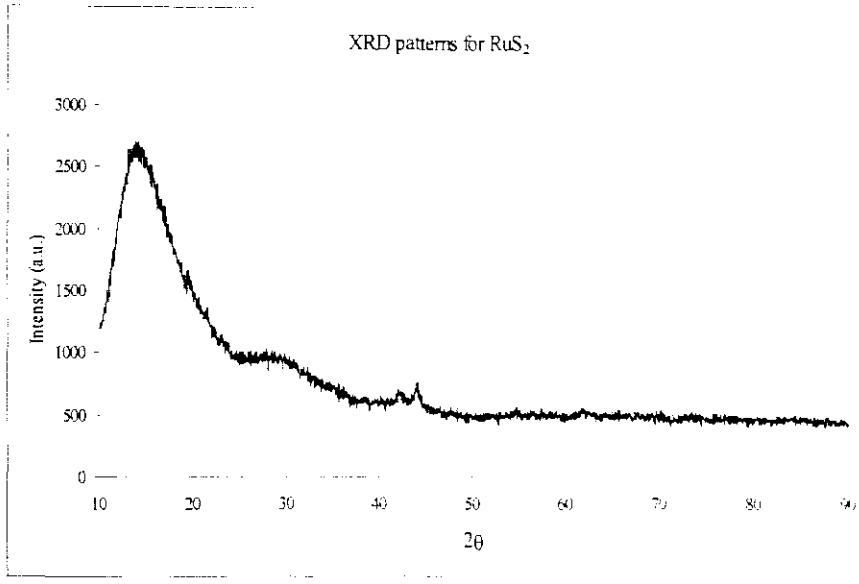

Figure 3.8 *XRD patterns of the RuS_2 thin films deposited at 450 °C.*

The XRD patterns of the RuS_2 deposited at 450 °C is shown in 3.8 above. A broad peak is observed for this material which is contrary to the expected patterns,[31] which show a cubic material for this chalcogenide. Chalcogenides of this nature have been synthesized and a cubic formation has been found to be the most dominant.

3.3.4.2. Optical properties

The UV-Vis absorption spectrum for the RuS_2 thin films grown at 350 and 450 °C is shown in Figure 3.9 and Figure 3.10 respectively. The band gap for the bulk ruthenium sulfide is observed at 1.22 eV.[24] In the present study the band gap energy is observed at 1.40 eV (450 °C) and 1.37 eV (350 °C). This observation shows a blue shift in the spectra compared with the bulk. Such feature was initially observed by Le Negard[23], where it was observed that the band gap for RuS_2 is 1.60 eV deposited on substrate such as GaAs and Al_2O_3. The difference in band gap energy for the materials deposited at different temperatures shows a slight shift to higher energy (0.03eV from 350 °C to 450 °C) with the increase in temperature (Figure 3.10).

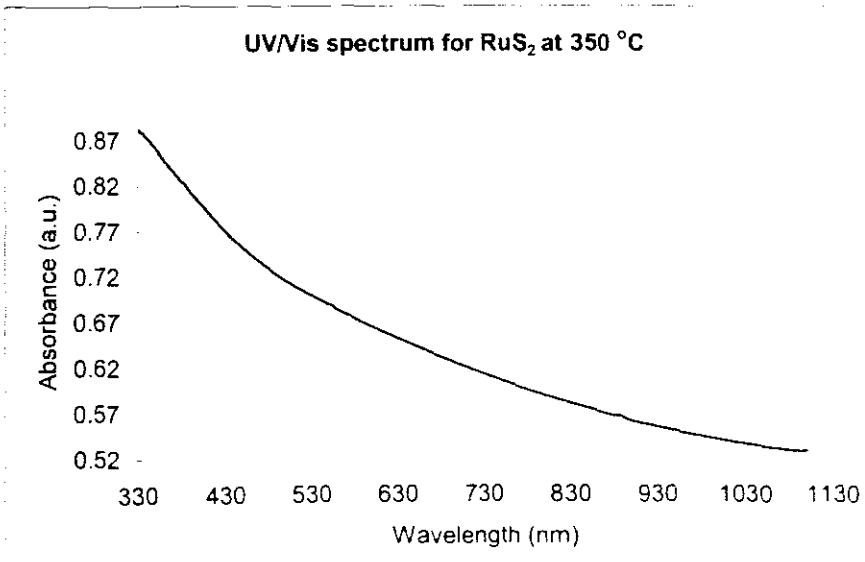

Figure 3.9 *The absorption spectrum for the RuS_2 thin films deposited at 350 °C.*

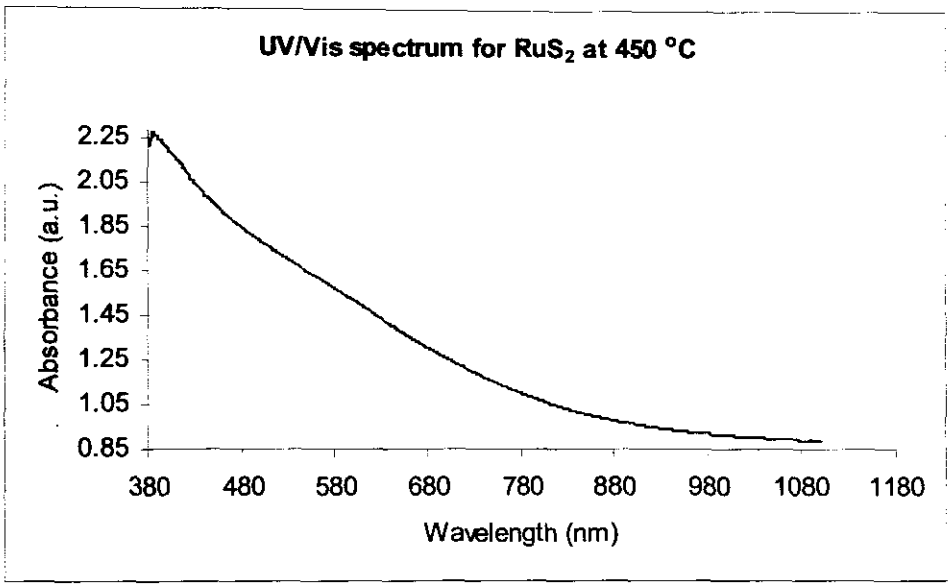

Figure 3.10 *The absorption spectrum for the RuS_2 thin films deposited at 450 °C*

3.3.5. Conclusions

The ruthenium diethyldithiocarbamato complex has been successfully synthesized using a straight forward procedure. The complex showed to be a tris-chelate Ru(III) complex. The complex proved to be a good precursor material for the deposition of ruthenium sulfide thin films, showing very volatile decomposition patterns. These semiconducting thin films showed very low band gap excitation energies. These band gap energies shift towards higher energy with increase in carrier concentration. The XRD patterns of this material showed a broad peak at low 2θ values and this could be attributed to strain mechanism in the thin films. The expected cubic formation was not found although this result is first of a kind and there has not been any full explanation for such observation.

The substrate/decomposition temperature at which the deposition was carried showed a marked influence on the optical properties of the thin film materials. Higher deposition

temperature leads to higher band gap energies. The temperature decides the extent of decomposition and hence free carrier concentration. Another observation is that an increase in temperature greatly improves the surface morphology. More uniform growth patterns are observed as the temperature is increased. The film thickness also is affected by the decomposition conditions. The higher the temperature, the higher the rate of decomposition and the faster the deposition rate (at constant flow rate and precursor concentration).

3.4. Deposition of Rh_2S_3 thin films from $[Rh(S_2CNEt_2)_2]$

3.4.1. Introduction

The d^7 Rh(II) dithiocarbamate complex was prepared in low yields. Notably there has not been much attention paid to the studies of coordination compounds of platinum metal d^7 ions.[25] Only a handful of substantiated studies on mononuclear complexes of rhodium complexes have been well reported.[26-33] Structural studies reveal that they are square planar complexes.[25] These are bis-chelate compounds of paramagnetic nature.

3.4.2. Synthesis of $[Rh(S_2CNEt_2)_2]$

A MeOH solution (50 mL) of NaOH (9.32 mmol) was reacted with diethylamine (9.32 mmol). The reaction mixture was cooled to 0 °C and CS_2 (9.32 mmol) added drop wise. The yellow reaction mixture was reacted with a MeOH of $RhCl_3.nH_2O$ (3.16 mmol) at 0 °C. The resultant orange precipitate was filtered, washed with MeOH and then hexane. The precipitate was then dried in air.

3.4.3. Deposition of Rh_2S_3

The AACVD was performed for the deposition of thin films at the following conditions.

Substrate	Glass
Temperature	350, 450 °C
Concentration	0.20 g/ 20 mL Toluene
Carrier gas	Nitrogen
Flow rate	200 mL/ min
Duration	2 hours

Table 3.4 *Parameters for the deposition of rhodium sulfide thin films.*

After the process had run for 2 hours, the precursor supply was terminated and the heating continued for a further 10 minutes. The black shiny thin films were cooled to room temperature and stored in air tight containers and further analysis was conducted.

3.4.4. Results and discussion

$[Rh(S_2CNEt_2)_2]$ was obtained in yields enough for the deposition of the metal chalcogenide thin films. The TGA spectrum in Figure 3.11 shows the decomposition patterns of this dithiocarbamate complex. Major decomposition starts at 350 °C and sharply continues until around 400 °C. 65 % of the complex weight is lost within this temperature range, which is a good sign of high volatility and the eligibility of this complex as a single source precursor in decomposition reactions.

Decomposition temperatures were done at 350 °C and 450 °C respectively. Temperature variations were used to monitor the behaviour of the film properties. As observed from the decomposition patterns, nucleation of the film is expected to be very fast, which may produce weakly adhered films.

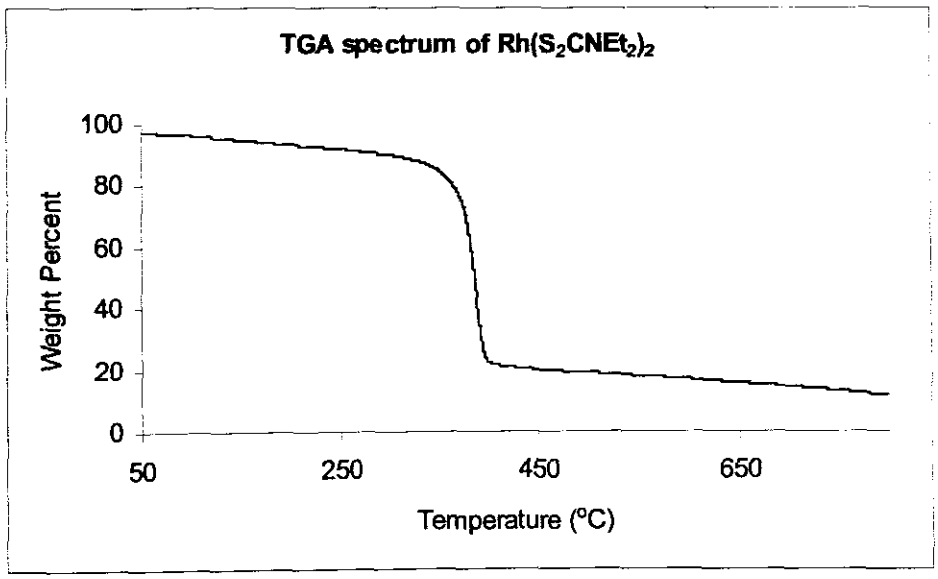

Figure 3.11 *TGA spectrum of [Rh(S$_2$CNEt$_2$)$_2$].*

3.4.4.1. Structural properties

The EDAX was performed to ascertain the presence of rhodium (Rh) and sulphur (S), as depicted in Figure 3.12.

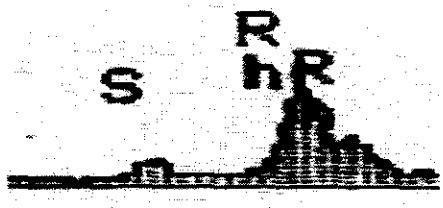

Figure 3.12 *The EDAX spectrum for RuS_2 thin films.*

Surface morphological patterns are illustrated in Figure 3.13 for the materials deposited at 350 °C. Large centres of growth stick out on the surface. This non-uniform growth is attributed to the low energy on the substrate surface; growth diffusion is limited to only a few sites on the substrate surface. Low growth temperatures are directly responsible for such observations. Although this type of growth occurs at the boundary layer (heterogeneous), adsorption of the film to the substrate is poor and may lead to traces of organic matter on the film surface.

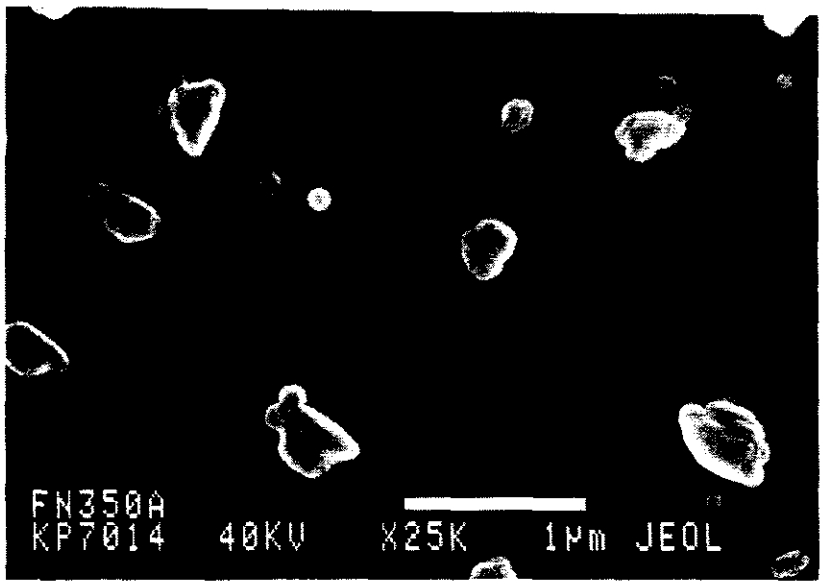

Figure 3.13A *SEM micrograph of Rh_2S_3 prepared at 350 °C (Top view).*

Grains with dimensions of 0.61 – 0.66 μm by length and 0.26 – 0.34 μm by breadth, are consistently observed. Figure 3.13B shows a side view of the thin film. Clearly the growth centres are observed and the distances between the growth centres which would normally be absent if the surface mobility was much higher than 350 °C.

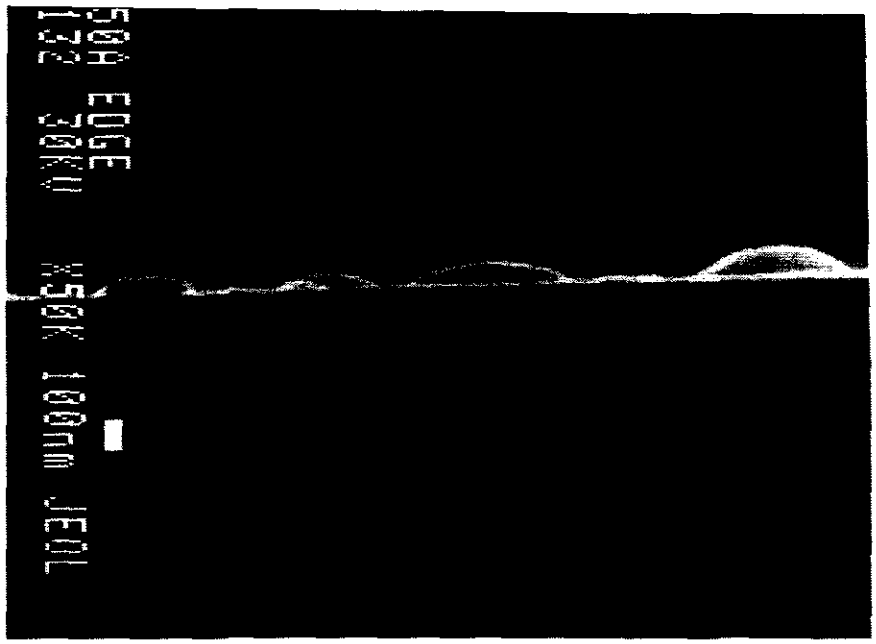

Figure 3.13B *SEM micrograph of Rh_2S_3 prepared at 350 °C (Side view).*

Growth at higher temperatures (450 °C) gives a much better morphology, with a much uniform surface. Scanning electron micrographs in Figure 3.14 illustrates the surface morphology of Rh_2S_3 deposited at 450 °C. The morphology of the thin film surface is very sensitive to the substrate temperature. The increase in temperature leads to the deposition of randomly oriented grains that grew up into larger (longer), more dense grains. The increase in temperature also affected the surface uniformity, with the crystallites becoming more clearly defined and the surface smoother with rod-like growth features. Film thickness of 255.632 nm was obtained at this temperature. Such a thickness translates to growth rate of 2.13 nm/min.

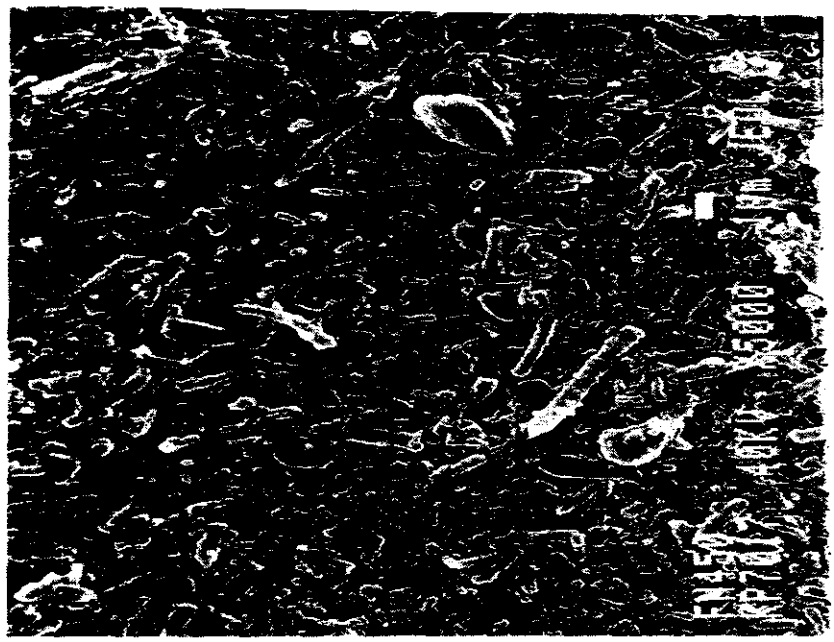

Figure 3.14A *A top view SEM micrograph of Rh_2S_3 thin film deposited at 450 °C*

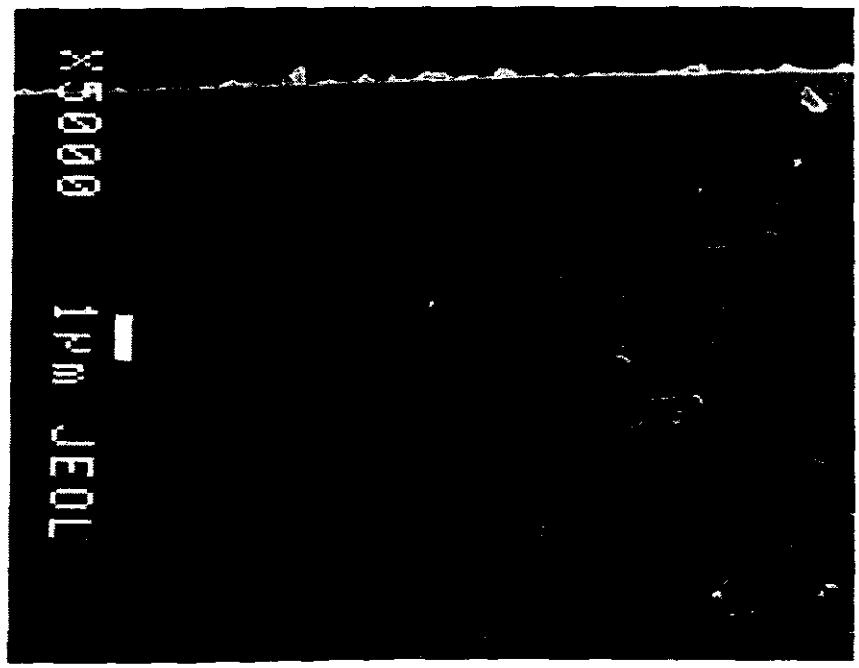

Figure 3.14B *Side view SEM micrograph of Rh_2S_3 deposited at 450 °C*

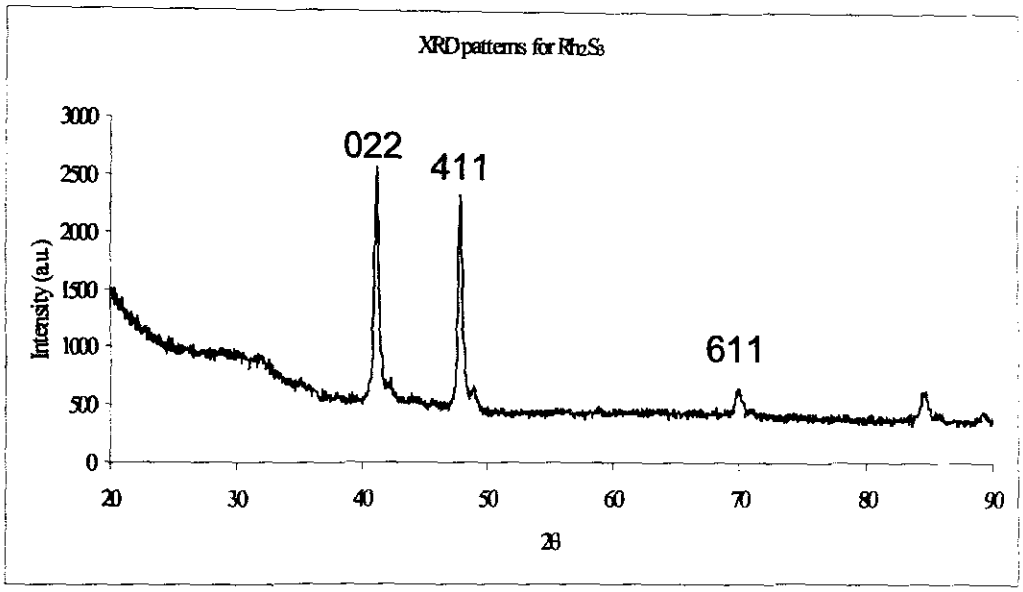

Figure 3.15 *The XRD patterns of Rh_2S_3 thin film*

2θ (Exp.)	**2θ (Lit.)**	***hkl***
41.2	42.15	022
47.8	47.96	411
70.2	70.23	611

Table 3.5 *XRD data for rhodium sulfide thin films deposited at 450 °C.*

Figure 3.15 shows the XRD patterns for the Rh_2S_3 patterns and Table 3.5 shows the XRD data for the thin films of rhodium sulfide (450 °C). Sharp peaks of the (022), (411) and (611) lattice planes corresponds to the orthorhombic phase of Rh_2S_3. No result of this kind has been reported, since no films of such materials have been reported before this study.

3.4.4.2. Optical properties

The band gap energy for this material is reported to be lower than 1 eV. Previous reports[34-36] suggested that the chalcogenides of rhodium show metallic to semiconducting behaviour. The only measured band gap for the bulk Rh_2S_3 was reported[24] to be 0.6 eV, which is deep in the infrared (IR) region. Optical measurements showed no obvious absorption by these materials at the UV-Vis spectrum range (180-900 nm). These are therefore of less importance in the mainstream semiconducting applications.

3.4.5. Conclusions

The orange $[Rh(S_2CNEt_2)_2]$ was synthesized using the standard procedure. The complex was obtained in low yields but enough to carry out decomposition reactions. The rhodium dithiocarbamato complex is a bis-chelate complex with the central metal ion at +2 oxidation state. The decomposition patterns of this complex showed a very volatile pattern which is a good indication of its suitability for the deposition of the metal sulfide thin films. The complex showed major decomposition at relatively low temperatures.

The metal sulfide thin films showed a rod-like growth patterns at higher deposition temperature (450 °C), with very high yields. Such growth preferences are sometimes attributed to the nature of the precursor material. As earlier observed, the surface morphology becomes more uniform as the decomposition temperature is increased. The thin films of Rh_2S_3 show lattice planes at (022), (411) and (611) show that these thin films of Rh_2S_3 are orthorhombic. The XRD data table showed correlation to this observation as observed in Table 3.5. The optical properties of such materials proved to be at lower energies (longer wavelength) compared to normal semiconducting materials and no significant absorption was observed within the UV-Vis range of the spectrum. This observation suggests that these materials are more metallic in their optical properties. This is an important feature in their applications in infra red materials.

3.5. References

1. De Loduguine J.S., *Illumination for Incandescent Lamps*, US Patent 575002, 1893
2. Feist W.M, Steele S.R. and Ready D.W., *Physics of Thin Films*, 1969, Vol 5, G. Hass and R.E. Thun, New York: Academic, p237
3. Hurtshouse M.B., Malik M.A., Motavelli M. and O'Brien P., *J. Mater. Chem.*, 1992, **2**, 949
4. Trindade T., O'Brien P. and Zhang X., *J. Chem. Mater.*, 1997, **9**, 523
5. Hursthouse M.B., Malik M.A., Motavelli M. and O'Brien P., *Polyhedron*, 1992, **11**, 45
6. West D.X. and Liberta A.E., *Coord. Chem. Rev.*, 1993, **123**, 49

7. O'Brien P., *Inorganic Materials*, 2nd Ed., W. Bruce, D. O'Hare, 1996, p525

8. Cowley A.H. and Jones R.A., *Polyhedron*, 1994, **13**, 1149

9. Bradley D.C., *Polyhedron*, 1994, **13**, 1111

10. P. O'Brien and Nomura R., *J. Mater. Chem.*, 1995, **5**, 1761

11. Cotton F.A. and McCleverty, *Inorg. Chem.*, 1964, **3**(10), 1399

12. Chatt J., Duncanson L.A. and Venanzi L.A., *Suomen Kemi*, 1956, 75

13. Pandey K.K., Nehete D.T. and Sharma R.B., *Polyhedron*, 1990, **9**(17), 2013

14. Coucouvanis D., *Prog. Inorg. Chem.*, 1970, **11**, 233

15. Williams J., Cras J.A., Staggara J.J. and Keijzers C.P., *Struct. Bonding*, 1976, **28**, 83

16. Eisenberg R., *Prog. Inorg. Chem.*, 1970, **12**, 295

17. Halls D.J., *Mikrochim. Acta*, 1969, 62

18. Bond A.M. and Martin R.L., *Coord. Chem. Rev.*, 1984, **54**, 23

19. Bond A.M., Hendrikson A.R., Martin R.L., Moir J.E. and Page D., *R. Inorg. Chem.*, 1983, **22**, 3440

20. Pignolet L.H., *Inorg. Chem.*, 1974, **13**(9), 2051

21. Serpone N. and Sieverers R.E., *Coord. Chem. Rev.*, 1971, **17**, 391

22. Wheeler S.H., Mattson B.M., Meissler G.L. and Pignolet L.H., *Inorg. Chem.*, 1978, **17**(2), 340

23. Le Negard N., Bounani A., Ezzaouia A. and Gorochov O., *J. Cryst. Growth*, 1990, **104**, 365

24. Yang T.R., Huang Y.S., Chyan Y.K. and Cheng J.D., *Czech. J. Phys.*, 1996, **46**, 2541

25. Pandey K.K. and Ahuja S.R., *Inorg. Chem.*, 1985, **24**, 2855

26. Martin B., McWhinne W.R. and Waind G.M., *J. Inorg. Nucl. Chem.*, 1961, **23**, 207

27. Fisher E.O. and Linder H.H., *Organomet. Chem.*, 1964, **1**, 307

28. Livingstone S.E., *Quatr. Rev.*, 1965, **19**, 386

29. Osborn J.A., Jardine F.H. and Wilkinson G., *J. Chem. Soc. A*, 1966, 1711

30. Baird M.C., *Inorg. Chim. Acta*, 1971, **5**, 46

31. Muniz R.P.A., Vngman N.V. and Danon J., *J. Chem. Phys.*, 1971, **54**, 1284

32. James B.R. and Styres D.V., *J. Am. Chem. Soc.*, 1972, **94**, 6225

33. Pneumatikakis G. and Psaroulis P., *Inorg. Chem. Acta*, 1998, **46**, 97

34. Dey S. and Jain V.K., *Platinum Metals Rev.*, 2004, **48**(1), 16

35. Jobic S., Brec R., Chateau C., Haines J., Leger J.M., Koo H.J. and Whangbo M.H., *Inorg. Chem.*, 2000, **39**, 4370

36. Matthias B.T., Corenzivit E. and Miller C.E., *Phys. Rev.*, 1954, **93**, 1415

CHAPTER 4

SYNTHESIS OF RHODIUM AND RUTHENIUM SULFIDE NANOPARTICLES

4 Introduction

The synthesis of semiconductor nanoparticles using single-source precursors has been proven successfully as a method of choice towards producing high quality, crystalline monodispersed nanoparticles. O'Brien *et al*[1-3] initially pioneered this method in the synthesis of II-VI semiconductor nanoparticles. There has been tremendous research into ways of developing efficient precursors for the deposition of semiconductor nanoparticles. There also have been reports on the use of single-source precursors for deposition of such materials by MOCVD.[4-6] Dithio- or diseleno-carbamato complexes of transition metals (e.g. Zn and Cd) have been extensively explored in this regard.[7]

Dithiocarbamato complexes of ruthenium and rhodium were synthesized and subsequently employed as the single- molecular precursors for the synthesis of ruthenium and rhodium sulfide nanoparticles in this work. There have been no reports of the use of such compounds for the synthesis of ruthenium and rhodium sulfide nanoparticles. The preparation of these small entities requires stabilizing agents to prevent them from aggregating. The presence of a stabilizing agent (surfactant or capping agent) prevents the particles from coalescing and allows their self-assembly on various surfaces. These surfactants can either be classified as anionic, cationic, zwitterionic or non-ionic. They have an amphipathic structure in the solvent of use i.e. lyophobic (solvent repulsive) and/or lyophilic group (solvent attractive).The most successful stabilization was achieved with the use of tri-*n*-octylphosphine oxide (TOPO) to cap CdS, CdSe and CdTe nanoparticles by Murray *et al.*[8] This synthesis involved thermolysis of Me_2Cd (Cd

source) and TOPE (E = S,Se or Te; the chalcogenide source) in hot TOPO (120 – 300 °C) to produce crystalline, surface-passivated nanoparticles.

Various capping agents have been employed in the preparation of nanoparticles. These include long-chain thiols,[9] phosphines,[10] pyridine derivatives[10] and long-chain amines.[11] The use of pyridyl derivatives has been reported by Steigerwald[12]; whereby, $Cd(SePh)_2$ precursor was thermolysed in 4-ethylpyridine producing monodispersed CdSe nanoparticles. The choice of stabilizer also has a marked influence on the final properties of the material. One explanation for such an observation might be the coordination mode of the capping agent on the nanoparticle.

Although there has never been any reported attempt on the synthesis of ruthenium and rhodium sulfide nanoparticles from such precursors, their dithiocarbamato complexes have been well documented.[13-14] In this study the dialkyldithiocarbamates of ruthenium and rhodium were synthesized and used as single-source precursors for the deposition of metal chalcogenide nanoparticles.

4.1. Synthetic route

The single-source molecular precursor method involves dispersing the precursor in tri-*n*-octylphosphine (TOP) solution, generally stirring for periods of 24 hrs. The TOP dispersed precursor is then injected into hot TOPO (250-350 °C) or hexadecylamine (HDA). The decomposition of the molecular precursor controls (limits) the nanoparticle formation and the growth is terminated with the depletion of the precursor supply. Notably, the duration of reaction, reaction temperature and the monomer concentration all affect the process of nanoparticle formation. To counter this, other factors are kept constant whilst changing one or two others.

On injection of the precursor solution, there is a rapid nucleation, followed by slow growth of the nuclei by Ostwald ripening mechanism as in Figure 4.1. The resultant nanoparticles are passivated with the TOPO or HDA to prevent agglomeration. Although this is necessary, it inadvertently counters the formation of particles with very narrow size distribution, where nuclei form at nearly the same time and agglomeration and Ostwald ripening of particles in solution does not occur.

Isolation of the nanoparticles is usually achieved by addition of a non-solvent (MeOH), which increases the solution polarity and in the process lowers the energy barriers to the formation of a loose network of particles (flocculation). The precipitate (if obtained) is then centrifuged and redispersed in toluene or any other relevant solvent to give optically clear TOPO/HDA capped nanoparticles.

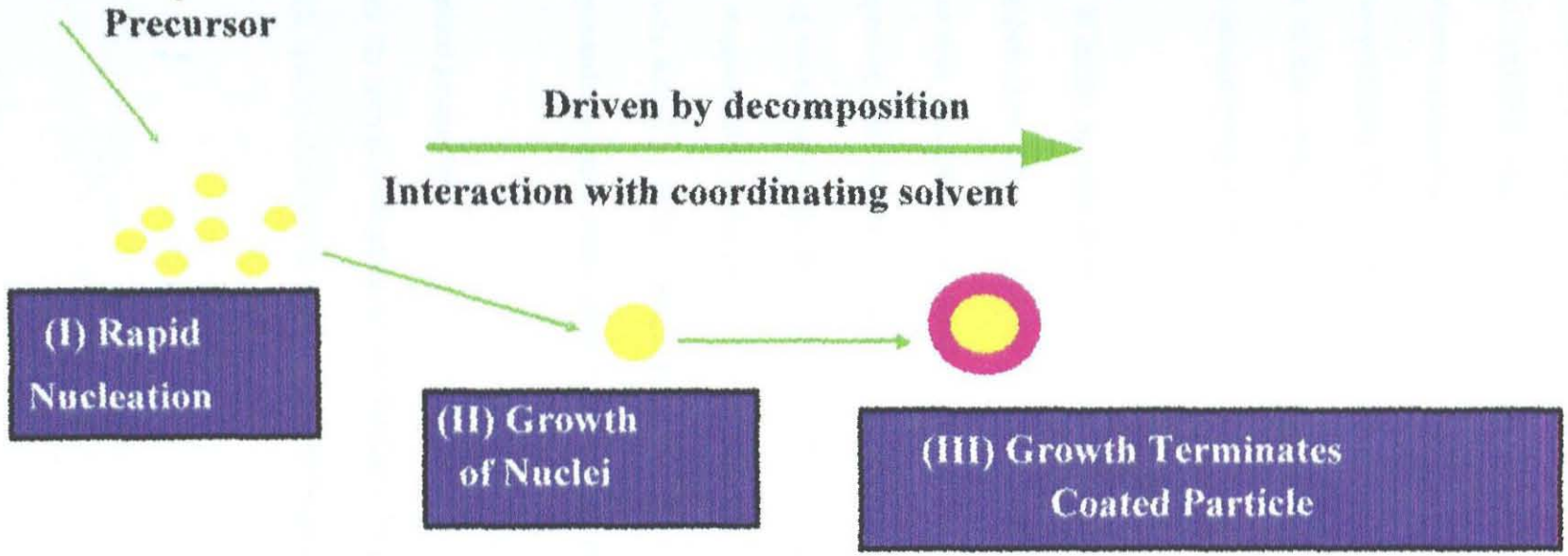

Figure 4.1 *The mechanism of growth leading to the formation of the coated nanoparticles.*

4.2. Synthesis of $[Rh(S_2CNEt_2)_2]$

The synthesis of $[Rh(S_2CNEt_2)_2]$ (**B1**), its subsequent characterizations and its decomposition patterns is reported in Chapter 3.4. This compound showed high volatility at relatively low temperatures. This diethyldithiocarbamato complex of rhodium was used for the deposition of thin films and the nanoparticles as well. In this study attempts at preparation of the nanoparticles of Rh_2S_3 are described.

4.2.1. Synthesis of Rh_2S_3 nanoparticles at 280 °C

B1 (0.6 g) was dispersed in TOP (10 mL) for 24 hours with constant stirring. The red-orange mixture was then injected into hot HDA (5 g) solution, pre-heated and maintained at 280 °C. On injection, the solution darkened on continued heating. A fraction was extracted (2 mL) of the solution after 90 minutes and the reaction continued for 2 hours. The reaction was stopped after 120 minutes, the mixture was cooled to about 70 °C and excess methanol was added to induce flocculation. The dark orange powder was then centrifuged and repeatedly washed with methanol and redispersed in toluene.

4.2.1.1. Optical properties

Figure 4.2 A shows the optical absorption for the fraction of the Rh_2S_3 extracted at t = 90 minutes. The optical spectra show a blue shift in the absorption edge of the Rh_2S_3

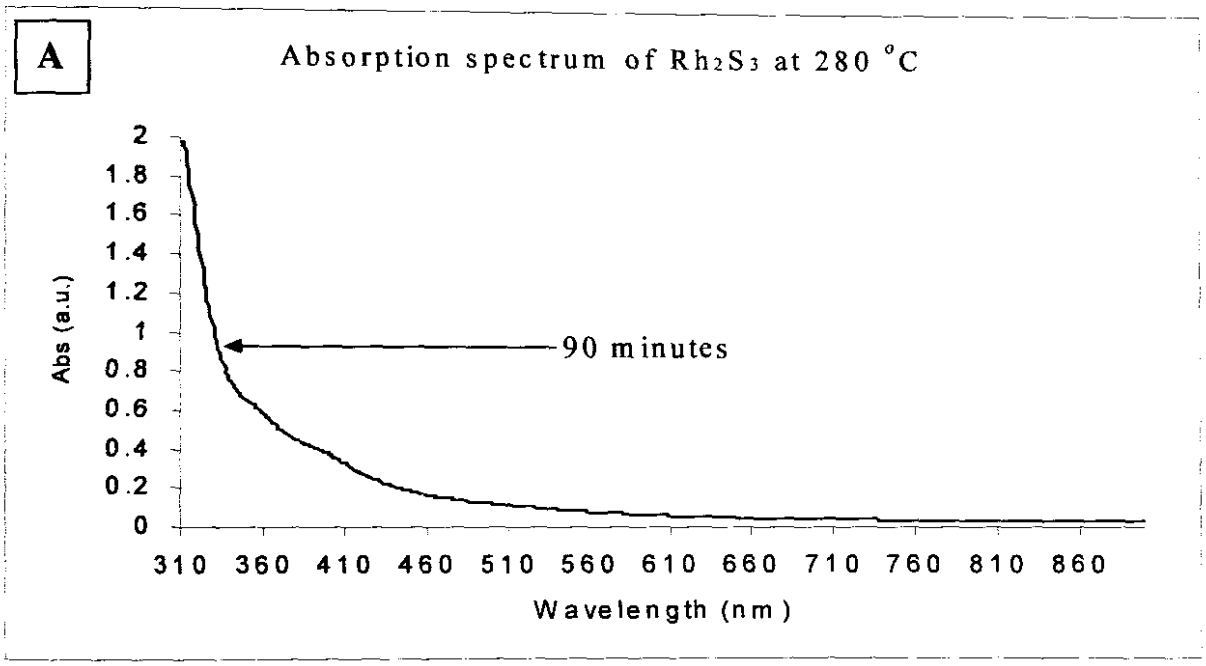

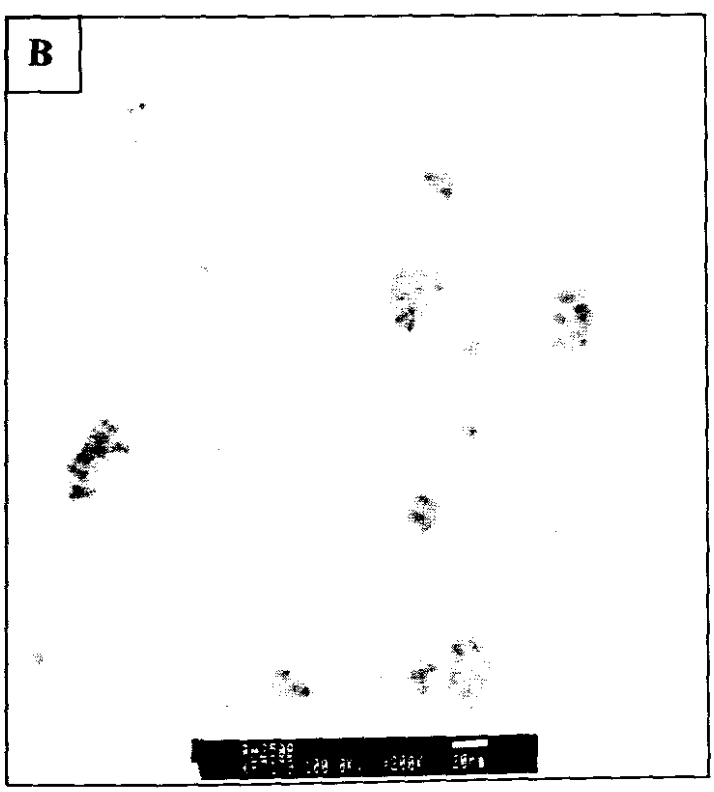

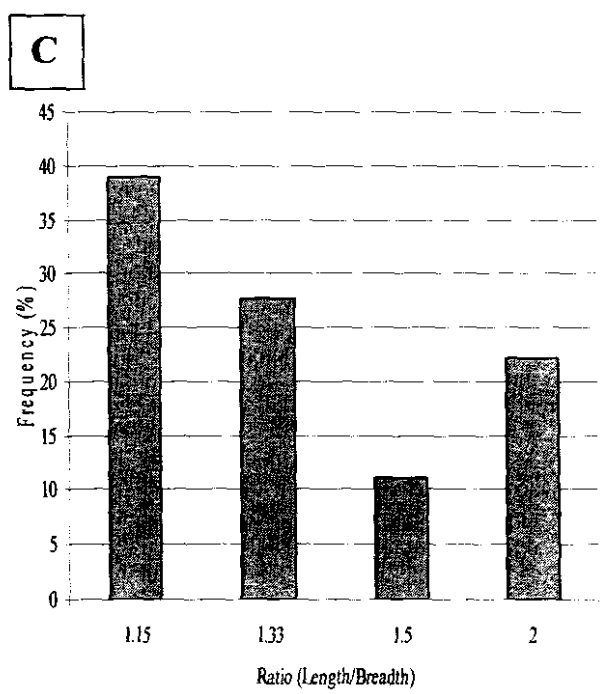

Figure 4.2 A. *Optical absorption,* ***B.*** *TEM micrograph and* ***C.*** *aspect ratio distribution of the Rh_2S_3 nanoparticles for the first fraction (t = 90 minutes).*

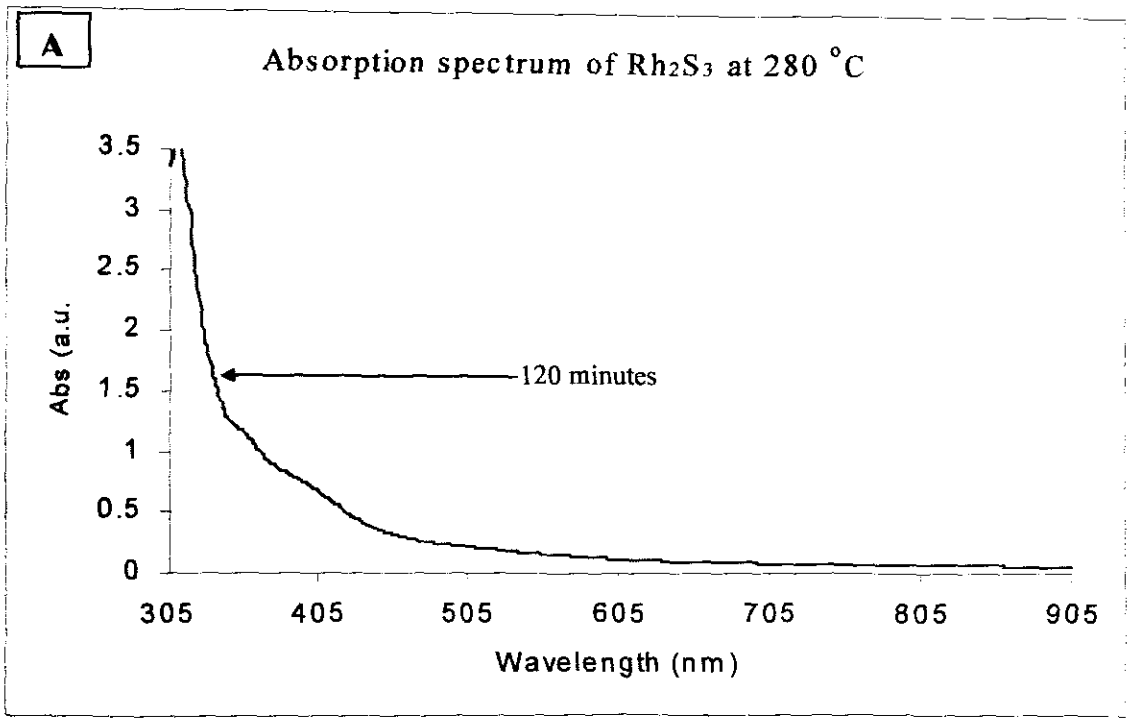

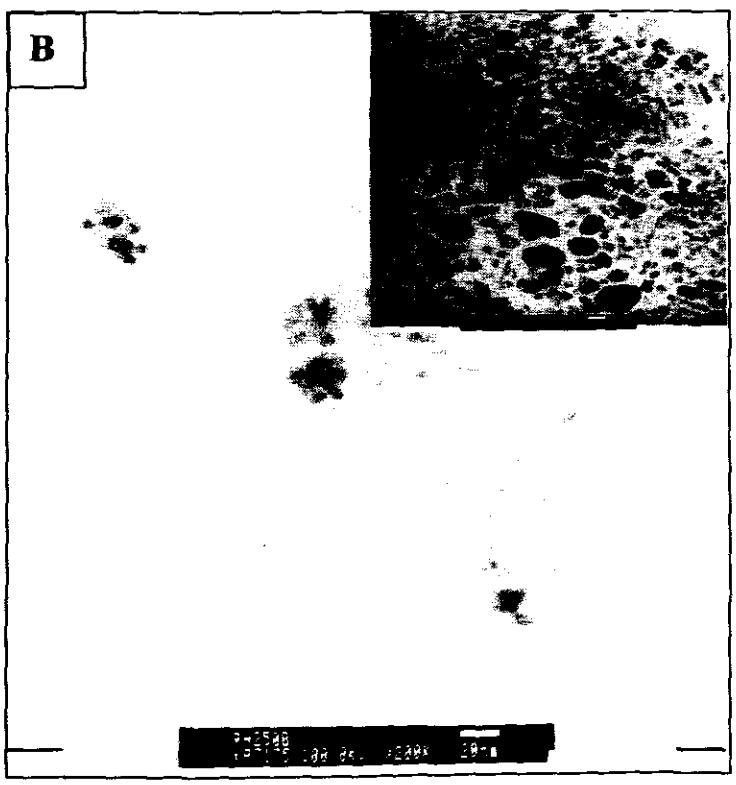

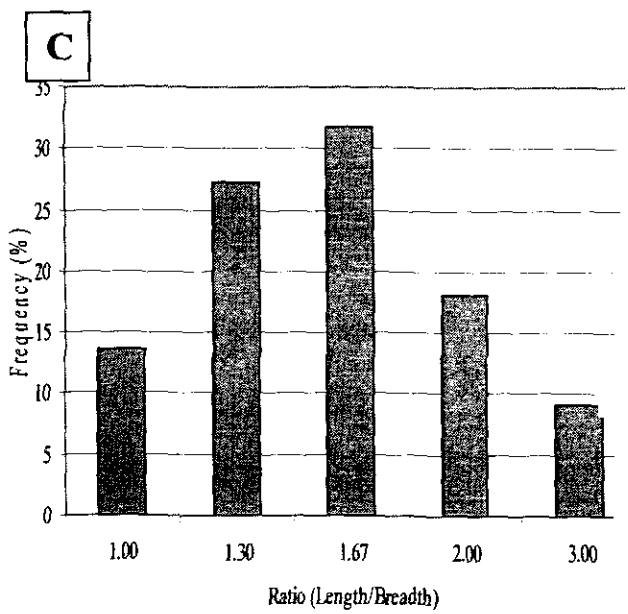

Figure 4.3 *A. Optical absorption,* ***B****. TEM micrograph with a zoomed area and* ***C****. aspect ratio of the Rh_2S_3 nanoparticles for the second fraction (t = 120 minutes).*

compared with bulk macrocrystalline Rh_2S_3 (0.6 eV, 2066.7 nm). This feature is attributed to the quantum size effects of the nanosized materials. This effect can be explained by considering the absorption of a light quantum in nanosized Rh_2S_3, an electron is transferred from the valence band to the conduction band, leaving behind a hole. In small nanosized particles, the wave functions of the electron and the hole are confined to the particle volume. Hence, if the particle size becomes comparable or smaller than the de Broglie wavelength of the charge carriers, the confinement increases the energy required for creating an electron/hole pair. The band gap of 420 nm (2.95 eV) is observed for the fraction taken after t = 90 minutes. The absorption edge for the t = 120 min sample (Figure 4.3 A) is slightly red shifted at 422 nm (2.93 eV). This red shift is due to the growth of the particles with time, an example of tunability of the properties of nanosized materials.

4.2.1.2. Structural properties.

Figure 4.2B shows the TEM micrograph of the Rh_2S_3 nanoparticles at t = 90 minutes. Predominantly rod-shaped growth patterns and some sparsely distributed spherical particles are observed. The average length of the rods is *ca.* 7.27 nm and they have an average breadth of *ca.* 5.40 nm. As can be seen in Figure 4.2C the ratio of the length to the breadth of the rods. This ratio gives an indication on how the length differs with the diameter. The highest ratios occurred at the longest lengths. There is also a high degree of clustering of the nanoparticles which makes accurate quantification of particle size distribution difficult.

Figure 4.3 B shows the TEM micrographs of the second fraction of the Rh_2S_3 nanoparticles. The second fraction also shows predominantly rod-like growth patterns. The average length of the rods is *ca.* 10.27 nm and their average breadth is *ca.* 6.12 nm. The aspect ratio of the length to diameter is shown in Figure 4.3C where an even distribution is observed. Ratios of the length to diameter of up to four times are observed here and occur at higher lengths. Comparing the two fractions it is clear that the first fraction comprises of shorter (by at least *ca.* 3.0 nm margin) rods compared to the second fraction. The dispersity of the material is quite large (5.45 – 12.73 nm for t = 90 minutes, and 3.64 – 9.09 nm for t = 120 minutes in length). The first fraction comprises the better dispersity compared with the second one. The first fraction has a more populated growth compared with the second one, which might suggest that growth was still in process.

4.2.2. Synthesis of Rh_2S_3 at 350 °C

A similar procedure as in 4.2.1 above was used. TOPO (10 g) was used as the capping agent for this preparation, and the temperature was kept constant at 350 °C. Light orange solution rapidly turned black on continued heating. The reaction was terminated after 120 minutes, and excess methanol was added, but the whole reaction mixture dissolved in MeOH. Other attempts including petroleum ether and ethanol also did not precipitate the material out of solution.

4.2.2.1. Optical properties

Figure 4.4 shows the optical absorption for the nanoparticles. There is an increase in the absorption spectra towards shorter wavelengths (blue), compared with bulk material.

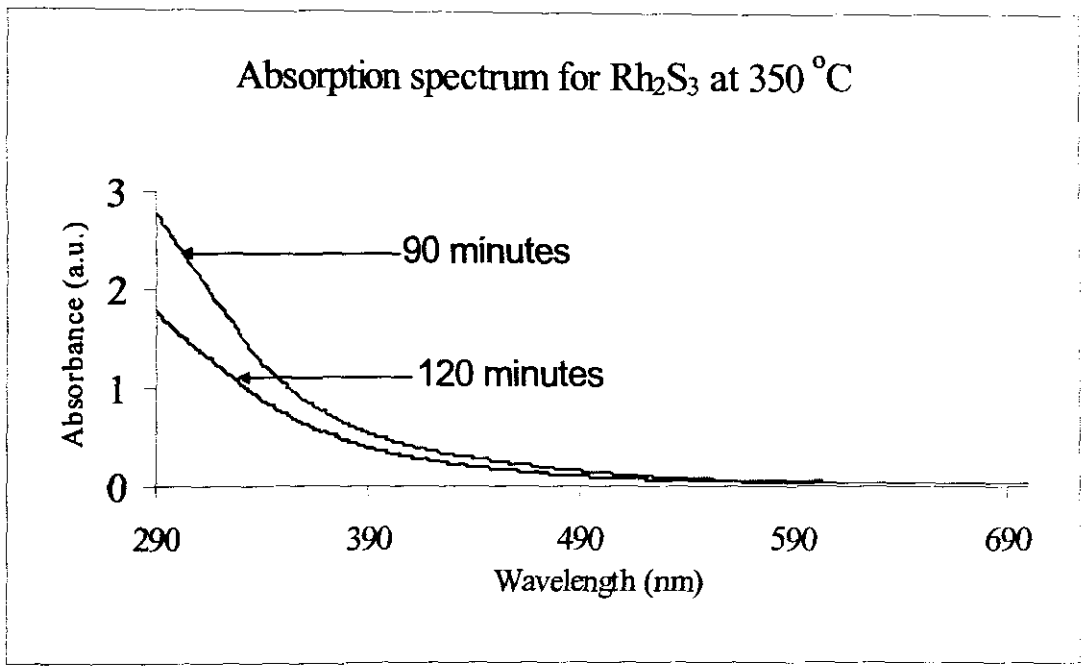

***Figure 4.4** The absorption spectra for Rh_2S_3 prepared at 350 °C from complex* **B1.**

The fraction at longer time period (t = 120 minutes) shows an absorption edge of 465 nm (2.67 eV), which is blue shifted from bulk. The other fraction (t = 90 minutes) is blue shifted even further at 459 nm (2.70 eV). This represents a shift of 0.03 eV between the time intervals.

4.3. Synthesis of $[Ru(S_2CNEt_2)_3]$

The preparation and characterization of $[Ru(S_2CNEt_2)_3]$ (**A1**) is presented in Chapter 3.3. This compound was shown to reasonably have high volatility at low temperatures. Thin films were successfully deposited using this dithiocarbamato complex and was also employed for the attempts at synthesizing the nanoparticles. Many attempts were made to precipitate these materials with some reasonable success.

4.3.1. Synthesis of RuS_2 nanoparticles at 300 °C

1g of **A1** was dispersed in 10 mL TOP and constantly stirred for 24 hours. The TOP-precursor mixture was injected into the hot TOPO (10 g) at 300 °C in a 3-neck flask. The mixture was heated and maintained at 300 °C. After 120 minutes, the reaction was stopped, cooled to 70 °C and excess methanol was added. The whole precipitate was dissolved in methanol and other precipitation techniques were attempted with no positive results. The optical spectra were recorded in MeOH.

4.3.1.1. Optical properties

The optical spectra for the RuS_2 nanoparticles are shown in Figure 4.5.

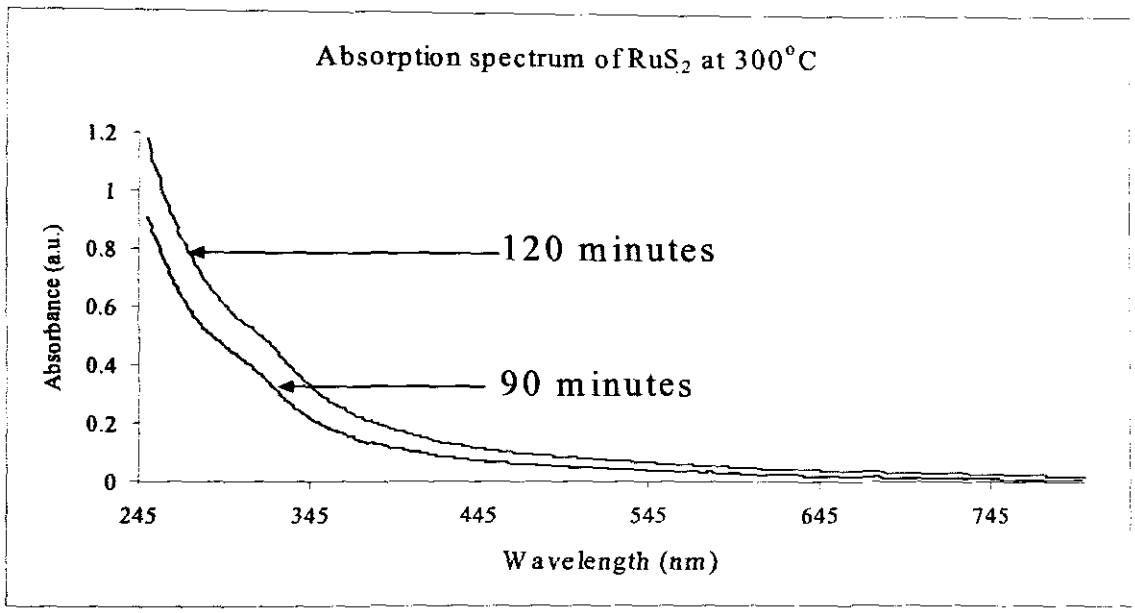

***Figure* 4.5** *Absorption spectra for RuS_2 showing the blue shift due to quantum size effects.*

Excitonic shoulders are visible for both the spectra. They both show a large blue shift compared with the bulk material of the same composition, at 1.6 eV (775 nm). The excitonic shoulder for the fraction at t = 90 minutes is observed at 352 nm (3.52 eV) compared with that observed at 360 nm (3.44 eV). This corresponds to a 0.12 eV shift in the spectra. The observation of the excitonic shoulder is evidence of the confinement effect of the particles.

4.3.2. Synthesis of RuS_2 nanoparticles at 280 °C

A similar procedure as in 4.3.1 was used with HDA instead of TOPO as the capping agent. **A1** (0.5 g), HDA (5 g), reaction duration of 120 min and the reaction was maintained at 280 °C. After 2 hours of reaction, it was stopped and excess methanol was

added, centrifugation followed; a small trace of the product was obtained and then redispersed in toluene for further analysis.

4.3.2.1. Optical properties

Figure 4.6A shows the optical spectra for RuS_2 prepared by the thermolysis of **A1** in HDA at 280 °C. The optical band edge was calculated at 426 nm (2.91 eV), which is also shifted towards higher energy compared with the bulk material of same composition. The absorption for the second fraction is observed at 420 nm (2.95 eV). This represents a blue shift of 0.04 eV between the time intervals.

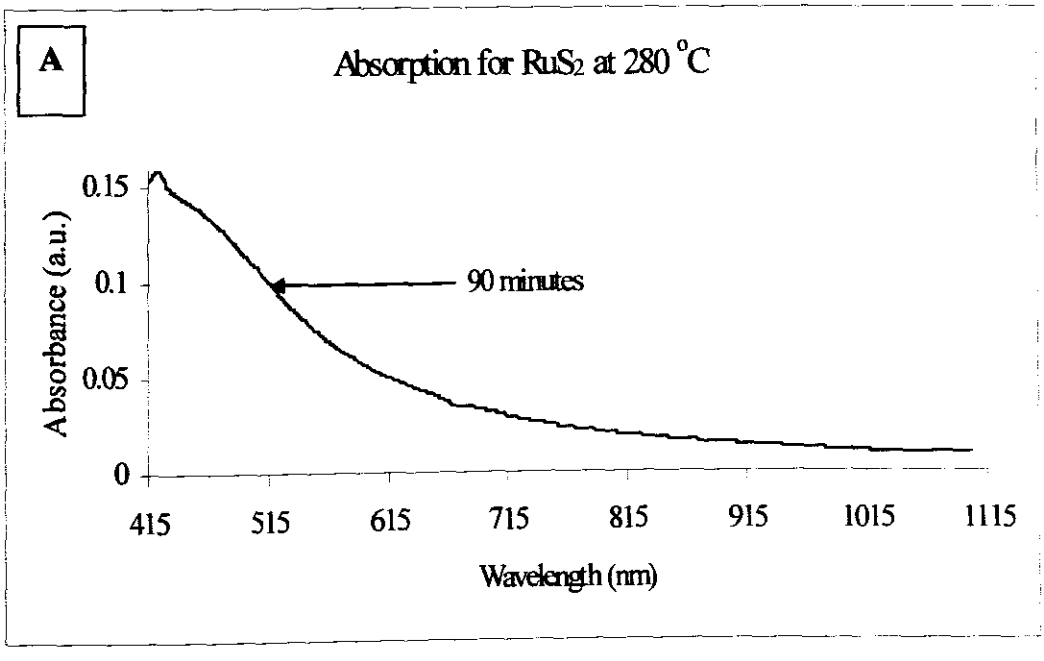

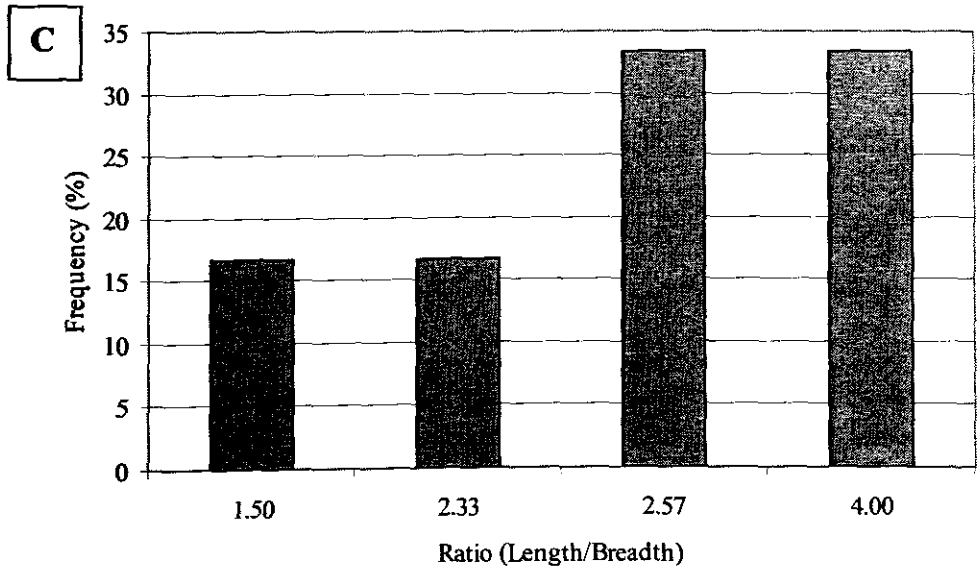

Figure 4.6 A. *Absorption spectrum,* ***B.*** *TEM micrograph and* ***C.*** *aspect ratio distribution of the RuS_2 nanoparticles (t =90 minutes).*

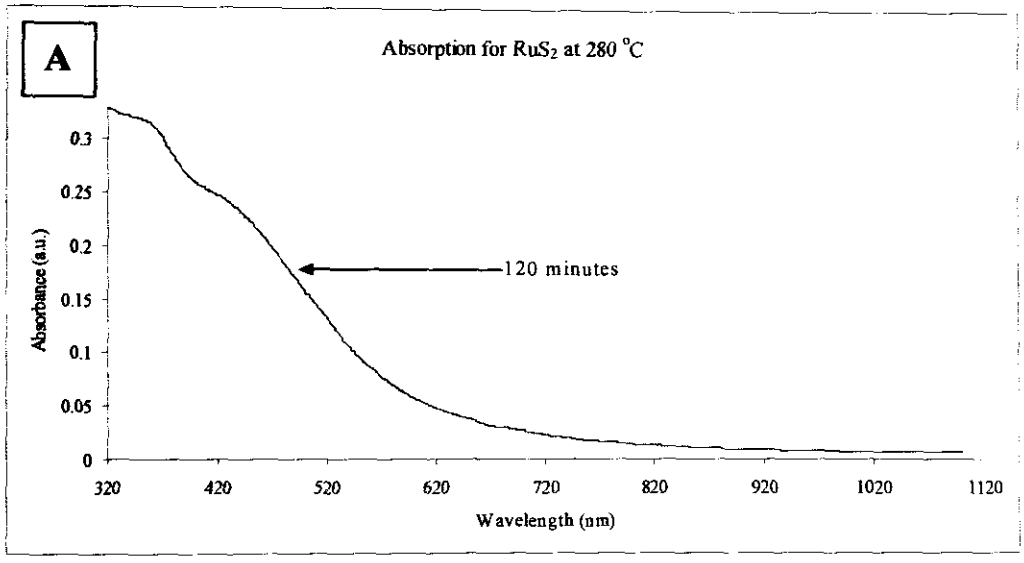

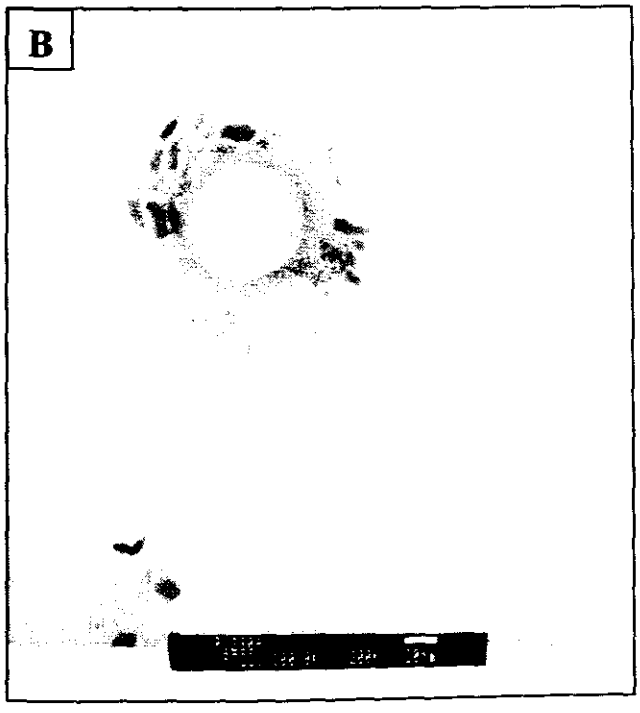

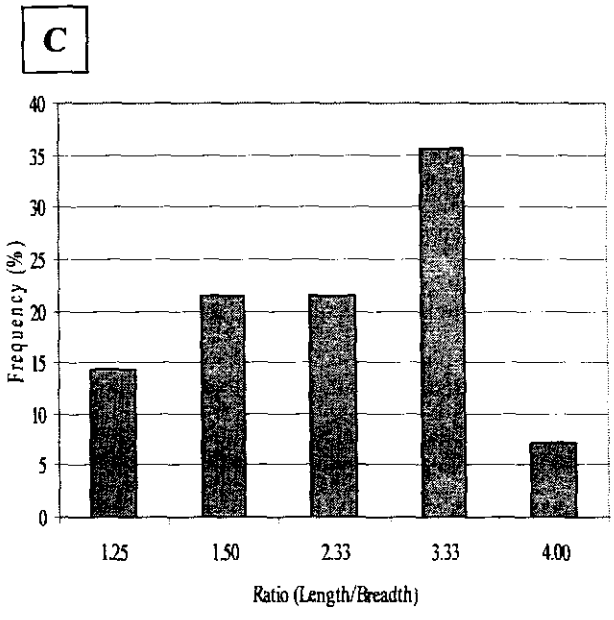

Figure 4.7 A. *Absorption spectrum,* ***B.*** *TEM micrograph and* ***C.*** *aspect ratio distribution of RuS_2 (t =120 min. fraction).*

4.3.2.2. Structural properties

Figure 4.6B shows the TEM micrograph of the nanosized RuS_2 fraction (t = 90 minutes). Sparsely distributed nanorod growth patterns are observed. The average breadth of the rods is *ca.* 6.18 nm and the average length is *ca.* 12.7 nm and their ratios are illustrated in Figure 4.6 C. Here most rods show a marked difference in their dimensions. Although they show higher occurrence of high ratio dimensions they all occur at relatively lower lengths. Figure 4.7 B shows the TEM image of the second sample (t = 120 minutes). These show similar patterns of growth but seem to be more defined than the sample at t = 90 minutes. The size ratio distribution is illustrated in figure 4.7 C. Their average length is *ca.* 15.39 nm whereas the average breadth is *ca.* 6.62 nm. These rods are slightly longer compared with the ones in the first sample (90 minutes).

The difference in the length of these entities for the two samples (*ca.* 0.44 nm) suggests that growth continues more in length and slightly in breadth as the reaction time is extended. There is also the observation of the large empty space in the particles, which might be attributed to the incorporation of the capping agent traces within the confines of the nanorod growth.

4.3.3. Synthesis of RuS_2 nanoparticles at 250 °C

Similar procedure as in 4.3.1 was used and TOPO was used as the capping agent. **A1** (0.5 g), temperature was kept at 250 °C and the reaction was maintained for 90 minutes. After the heating was stopped, the solution was cooled to 70 °C and excess methanol was added which subsequently dissolved all the contents of the mixture.

4.3.3.1. Optical properties

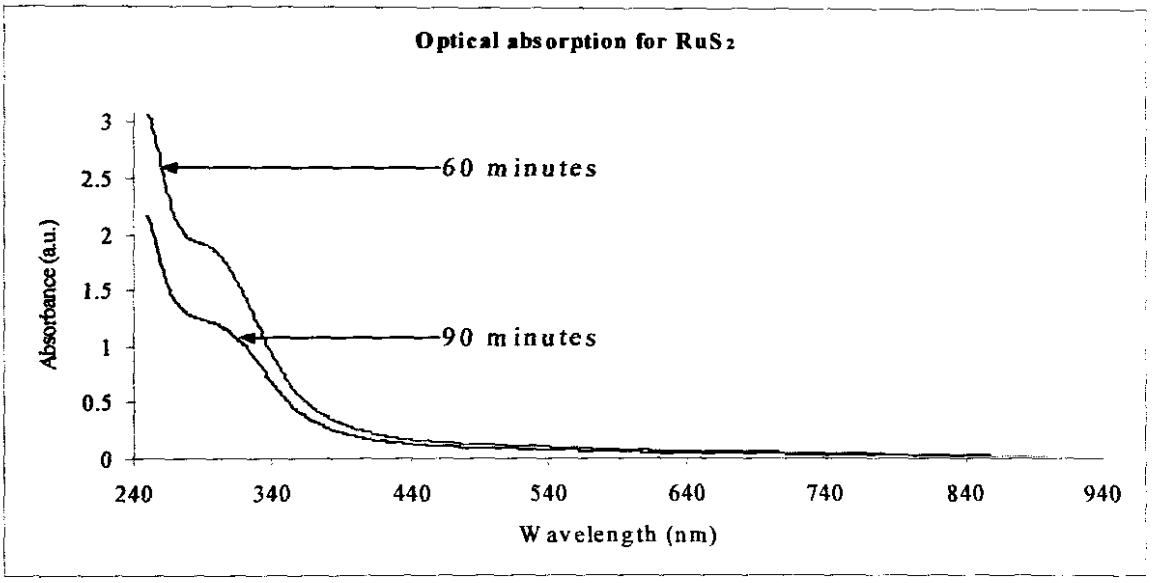

Figure 4.8 *Optical absorption of the RuS_2 nanoparticles thermolysed at 250 °C.*

Figure 4.8 shows the optical absorption of the ruthenium sulfide nanoparticles prepared at 250 °C. These show prominent excitonic shoulders in their absorption spectra. The band gap is observed at 342 nm (3.62 eV) for the sample at 60 minutes. The fraction taken after 90 minutes shows an absorption edge at 353 nm (3.51 eV). There is a red shift when time of reaction is increased. The shift of 0.11 nm is observed. These observations also show very high shift in the absorption energy when compared with the bulk material of similar composition.

4.4. Conclusions

Highly volatile dithiocarbamate complexes $[Ru(S_2CNEt_2)_3]$ and $[Rh(S_2CNEt_2)_2]$ have been successfully used as single source molecular precursor for the deposition of HDA and TOPO capped RuS_2 and Rh_2S_3 nanoparticles. These precursors proved to be reasonably effective as air-stable single source molecular precursors for this preparation. The inherent drawback is that they tend to form materials that show high solubility in MeOH (which is non-solvent to nanoparticles due to its lyophilic properties).

The Rh_2S_3 nanoparticles showed rod-like growth patterns and showed the quantum confinement effect in their absorption. They showed no luminescence properties, which means other deactivation processes are responsible for this. Radiationless mechanisms such as internal conversion and vibrational relaxation might be some of the deactivation routes. A steady increase in particle sizes for Rh_2S_3 was observed with the increase in reaction time. This can also be observed by the decrease in band gap energy as the reaction time increased. The TEM of Rh_2S_3 particles (280 °C) showed predominantly rod-like formation with the length of between 7.27 – 10.27 nm and breadth between 5.40 – 6.12 nm between the time intervals.

RuS_2 nanoparticles also showed growth preferences of predominantly rods. They also showed a decrease in band gap energy as the time of reaction increased. Their absorption was blue shifted with respect to the bulk material of similar composition. These materials also have no luminescence property, which means other radiationless deactivation mechanisms are favored. For materials prepared at 280 °C, the TEM image showed rod-

oriented preferential growth. The average length of between 12.7 – 15.39 nm and the breadth of 6.18 - 6.62 nm was observed. For both RuS_2 and Rh_2S_3, growth patterns showed higher definition at higher reaction times, which signifies the completeness of growth.

4.5. Additional work

4.5.1. Synthesis of palladium sulfide nanoparticles

Preparation of palladium dithiocarbamate complexes has been described by Nakamoto[16] and Kuriascose.[17] They reported the reaction of ammonium dithiocarbamate with palladium and platinum salts. In this study, the complexes were synthesized by the reaction of the metal salt and a sodium dithiocarbamate salt (prepared by the action of CS_2 on the reaction mixture of NaOH and an amine). The ligands for such preparation can be varied by using different kinds of alkyl amine.

O'Brien, *et al*[18] used such compounds to synthesize TOPO capped palladium sulfide and platinum sulfide nanoparticles, employing these complexes as single source molecular precursors. Similar compounds have been used to deposit thin films by MOCVD.[18] The nanoparticles of palladium and platinum have shown high level of applicability in catalysis[19] and in material sciences.[20]

4.5.1.1. Synthesis of $[Pd(S_2CN^iPr_2)_2]$[16]

This complex was prepared by the literature method. K_2PdCl_4(1.0 g; 3.06 mmol) was reacted with a cold (0°C) solution of $Na(S_2CN^iPr_2)$ (9.18 mmol), prepared by the reaction of NaOH (0.37 g; 9.18 mmol), CS_2 (0.55 mL; 9.18 mmol) and $^iPr_2NH$ (1.30 mL; 9.18 mmol) in cold water (0°C). The black-red precipitate was obtained after overnight refrigeration and filtration.

4.5.1.2. Synthesis of TOPO capped PdS nanoparticles

0.2 g of $[Pd(S_2CN^iPr_2)_2]$ was dispersed in TOP (10 mL) for 24 hours. The TOP-precursor mixture was then injected into TOPO (10 g) preheated and maintained at 280 °C. The heating was maintained at this temperature for 90 minutes and the black precipitate was then cooled to 70 °C. Excess MeOH was added to flocculate the particles and the precipitate was separated by centrifugation.

4.5.1.2.1. Results and discussion

The TGA spectrum for the complex is illustrated in Figure 4.9. Notably the complex showed very poor decomposition patterns, which is a measure of its volatility. A steady decomposition starts at around 50 °C, but stabilizes and starts again at around 200 °C where it continues to *ca.* 300 °C. During this 100 °C range about only 11 % of the sample weight is lost. A steady decrease continues all the way to 800 °C with a few kinks but no significant major loss of weight. Such patterns are a major hindrance in the deposition of thin films. Nanoparticles can be deposited using such a precursor although the yields

would not be expected to be very high. An overall loss of *ca.* 35 % of the sample weight was observed, which is a far less from what works from thin films.

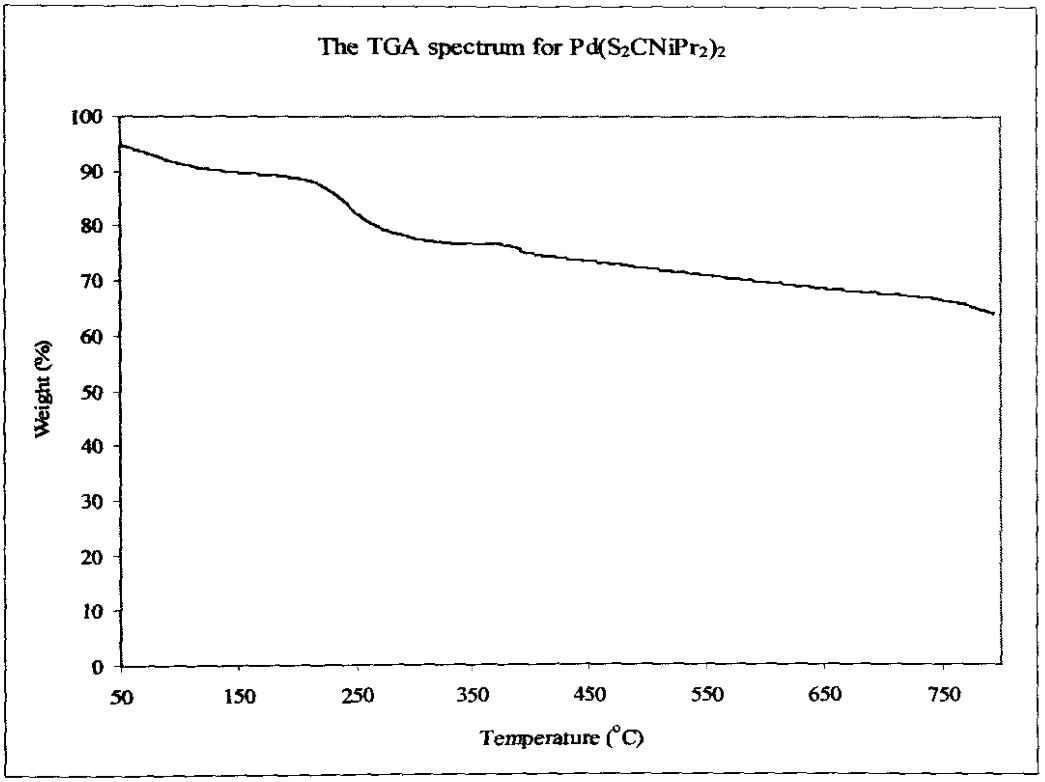

Figure 4.9 *The TGA spectrum of the complex [Pd($S_2CN^iPr_2$)$_2$]*

4.5.1.2.2. Optical properties

The absorption and emission spectra of PdS nanoparticles are illustrated in Figure 4.10A and B. The band gap is observed at 444 nm (2.79 eV) with no visible excitonic features. The emission maxima for PdS (468 nm; 2.65 eV) is red shifted with relation to the absorption band gap. The non-smooth lines of the emission peak signify the difference in the particle sizes of the PdS nanoparticles.

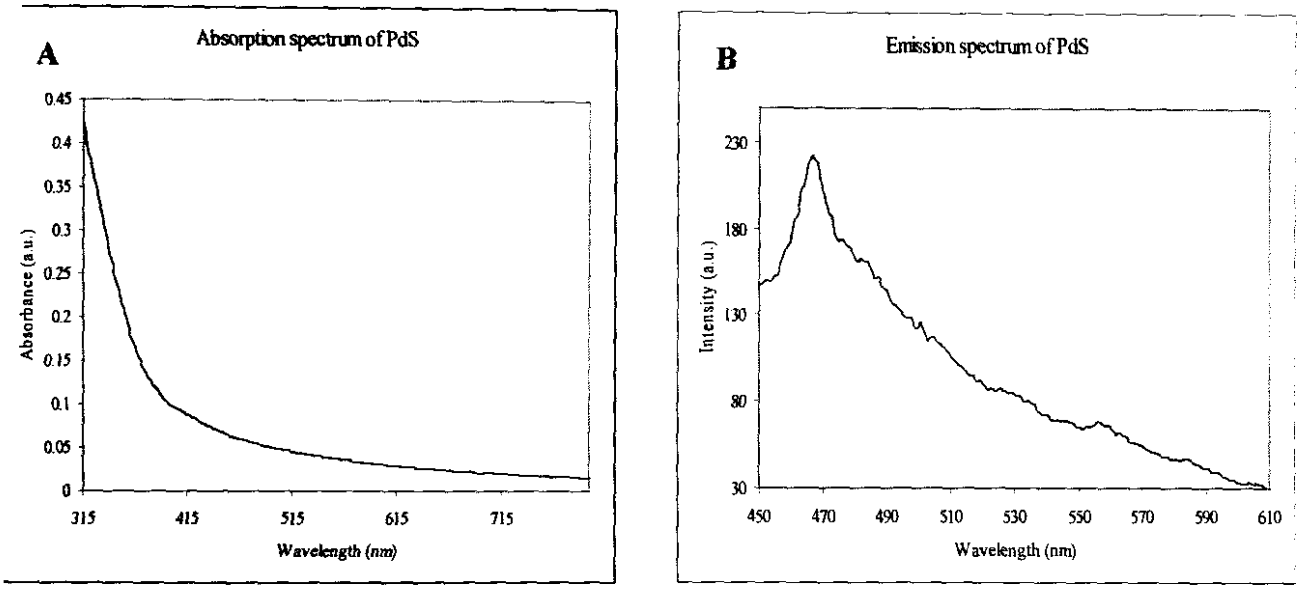

***Figure 4.10 A**. Absorption and **B**. emission spectra for PdS nanoparticles.*

4.5.1.2.3. Structural properties

Figure 4.11A and 4.11B show the TEM micrographs of the TOPO capped PdS nanoparticles. The particle sizes ranges between 3.65 – 8.18 nm and the average particle size is 6.14 nm. The TEM image showed growth preference of spherical particles, with some areas densely populated with particles than others. This fact poses a degree of agglomeration of the particles, which might be due to the sample preparation of the TEM sample or the growth mechanism of these particles. The particles clearly show growth patterns which are in line with the previously reported findings for PdS nanoparticles.[18]

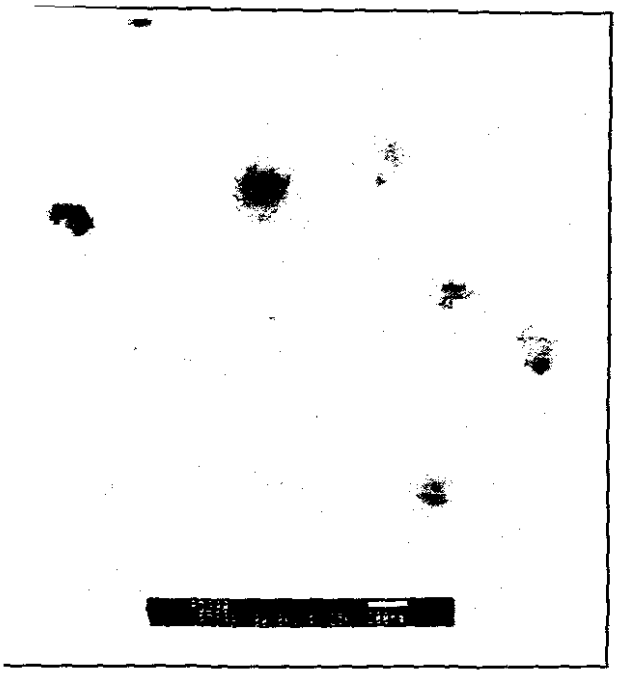

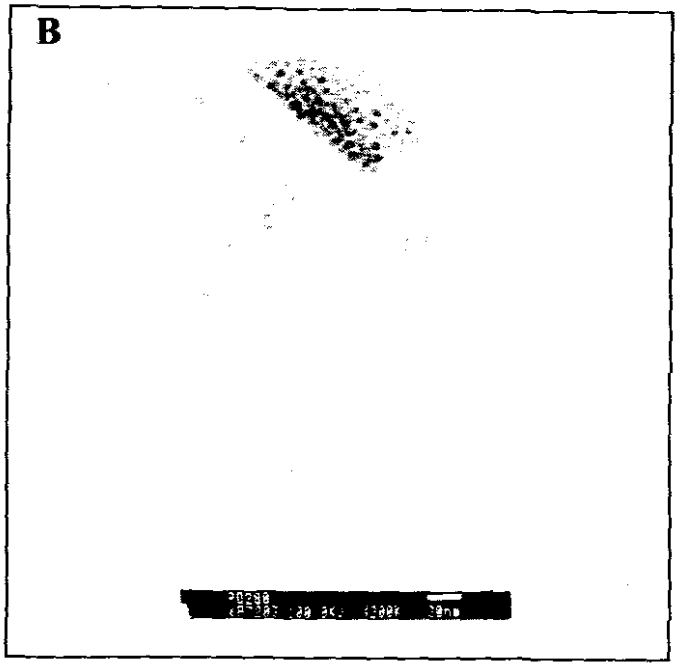

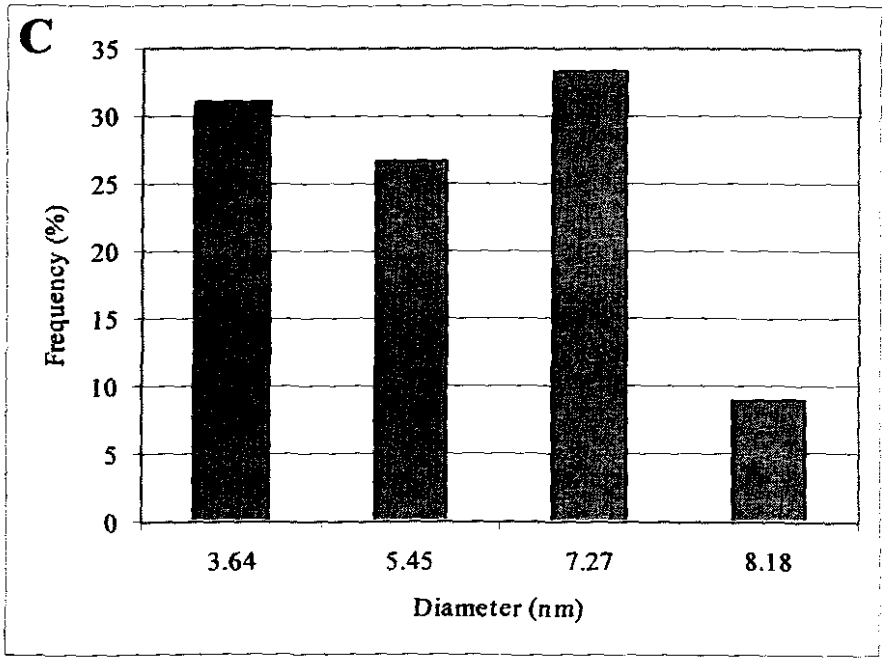

***Figure 4.11 A**. TEM image, **B**. same as figure A. at higher magnification and **C**. particle size distribution of the PdS nanoparticles.*

4.5.1.3. Conclusions

The bis(tertbutyl)dithiorcabamato palladium (II) complex has been used to synthesize the nanoparticles of PdS. This complex showed very low volatility and was not usable in the deposition of thin films because of low growth rates even at high temperatures. However TOPO capped PdS nanoparticles were synthesized since the volatility is not of high importance for this preparation as compared with the thin films. Particles of size range 3.65 – 8.18 nm were successfully synthesized.

4.5.2. References

1. Trindade T., O'Brien P. and Zhang X., *Chem. Mater.*, 1999, **9**, 523
2. Trindade T. and O'Brien P., *Adv. Mater.*, 1996, **8**, 151
3. Trindade T., O'Brien P., Zhang X. and Motavalli M., *J. Mater. Chem.*, 1997, **7**, 1011
4. O'Brien P. and Nomura R., *J. Mater. Chem.*, 1995, **5**, 1761
5. Bochmann M., *Thin Solid Films*, 1993, **225**, 17
6. Arnold J., *Progr. Inorg. Chem.*, 1995, **43**, 353
7. Afzaal M., Aucott S.M., Crouch D., O'Brien P., Woolins J.D. and Park J.-H., *Chem. Vap. Deposition*, 2002, **8**(5), 187
8. Murray C.B., Norris D.J and Bawendi M.G., *J. Am. Chem. Soc.*, 1993, **115**, 8706
9. Chen S. and Murray R.W., *Langmuir*, 1995, **15**, 682
10. Schmid G., Maihak V., Lantermann F. and Peschel S., *J. Chem. Soc., Dalton Trans.*, 1996, 589
11. Yonezawa T, Tominaga T. and Richard D., *J. Chem. Soc., Dalton Trans.*, 1996, 783

12. Brennana J.G., Siegrist T., Carrol P.J., Stuczinski S.M., Brus L.E. and Steigerwald M., *J. Am. Chem. Soc.,* 1989, **111**, 414

13. Pignolet L.H., *Inorg. Chem.,* 1974, **13**(9), 2051

14. Pandey K.K., Nehete D.T. and Sharma R.B., *Polyhedron*, 1990, **9**(17), 2013

15. Jeevanandam P., Koltypin Y., Gofer Y., Diamant Y. and Gedanken A., *J. Mater. Chem.,* 2000, **10**, 2769

16. Nakamoto K., Fujita J., Condrate R.A. and Morimoto Y., 1963, **39**, 423

17. Rufus I.B., Viswanathan B., Ramakrishnan V. and Kuriascose J.C., *Photochem. and Photobilogy, A-Chem*, 1995, **91**, 63

18. Malik M.A., O'Brien P. and Revaprasadu N., *J. Chem. Mater.,* 2002, **12**, 92

19. Misono M. and Nojiri N., *Appl. Catal,*.1990, **64**, 1

20. Yamamoto T., *Chem. Abstr.,* 1987, **106**, 8769

CHAPTER 5

EXPERIMENTAL

5.1. Chemicals

Ruthenium chloride hydrate (Aldrich); Rhodium chloride hydrate (Aldrich); n-MethylHexylamine (Fluka); tert-Butylamine (99,5+ %, Aldrich); Diisopropylamine (99,5+ %, Aldrich); Diethylamine (Aldrich); Carbon Disulfide (Saarchem); Sodium Hydroxide (Aldrich); Dioctylamine (Aldrich); Tri-*n*-octylphosphine (TOP, 90%, Aldrich); Hexadecylamine (HDA 98 %, Aldrich); Tri-*n*-octylphosphine oxide (TOPO 90 %, Aldrich); Hexane (Aldrich); Dichloromethane (Aldrich); Toluene (Aldrich); Acetone (Saarchem), Methanol (BDH); Nitric acid (ACE); Hexane (BDH); Petroleum ether (ACE); Ethanol (Saarchem); DMSO (Merck).

5.2. Instrumentation

5.2.1. UV-Vis spectroscopy

A Perkin Elmer Lambda 20 UV-Vis spectrophotometer was used to perform the optical measurements. The samples were measured in quartz cells (1 cm path length) using toluene as the reference.

5.2.2. Infrared spectroscopy

Infrared measurements were performed using a Perkin Elmer Paragon 1000 FT-IR spectrometer. The samples were measured as KBr pellets and as Nujol mulls.

5.2.3. Electron Microscopy

Energy Dispersive Analysis by X-rays (EDAX) was performed on the thin film samples deposited on the glass substrate by evaporation using a JEOL JSM35CF Scanning Electron Microscopy.

5.2.4. Thermogravimetric Analysis

The thermogravimetric analysis (TGA) of the precursor compounds was carried out using the Perkin Elmer Pyris 6 TGA instrument under nitrogen gas. The heating rate of 10 ^{o}C/min was maintained during the analysis.

5.2.5. Photoluminescence

The photoluminescence of the samples was collected using the Perkin Elmer LS 55 spectrometer. The samples were run with toluene as their reference material.

5.2.6. Nuclear Magnetic Resonance

^{1}H-NMR and ^{13}C-NMR studies were carried out using a Bruker AC300 FTNMR instrument. D-chloroform ($CDCl_3$) was used as the reference solvent for the samples.

5.2.7. CHN elemental analysis

The elemental analysis of the samples was performed by the University of Manchester micro-analytical laboratory.

5.2.8. Mass spectroscopy

The electrospray mass spectra were recorded on a Kratos concept IS instrument, using dichloromethane and DMSO as solvents.

5.2.9. AACVD kit

A home made AACVD kit was used to deposit the thin films. The kit consists of a CARBOLITE furnace, a 2 –necked flask and a Mountain Breeze ultrasonic humidifier with moisture output and humidity level controls.

5.2.10. Ellipsometry

The thickness of the films was measured using the model M220 ellipsometer. The ellipsometer determines the refractive index and the coefficient of extinction of a film by measuring the change in polarization state of the light reflected from the film surface. The film thickness was then determined from these parameters. The measurements were conducted at JASCO International laboratories.

5.3. Preparation of the precursors

The complexes were prepared by following the literature methods. Attempts were made at preparing other complexes by adopting the literature methods and modifying them. Their composition and structures were established using instrumental techniques such as Mass spectroscopy (MS), proton NMR (^{1}H-NMR), CHN analyser, Infrared (IR) and Thermogravimetric Analyser (TGA). Techniques such as ^{13}C-NMR proved insensitive for structural elucidation purposes. Some of these complexes, that were successfully

established, were used as single source molecular precursors for both the deposition of thin films and nanoparticles.

5.3.1. Synthesis of $[Ru(S_2CNEt_2)_3]$ [1a-d, 2, 3]

CS_2 (3.04 mL; 50.62 mmol) was slowly added from a dropping funnel into a mixture of NaOH (2.03 g; 50.62 mmol) and Diethylamine (Et_2NH) (5.24 mL; 50.62 mmol) in 50 mL methanol (MeOH) at 0 °C with constant stirring. A 50 mL MeOH solution of $RuCl_3.nH_2O$ (3.50 g; 16.87 mmol) was prepared and cooled to 0 °C. The cold $Na(S_2CNEt_2)$ solution was slowly reacted with the red-brown metal salt solution. On addition of the ligand a black precipitate formed, the mixture was refrigerated for 24 hr, filtered, washed with MeOH and then Hexane. The product was then dried in air.

Yield: 3.901 g; 47.14 mmol; 42.35 %; mp 244 °C

CHN: Calc (Found): C 33.0 (32.45); H 5.50 (5.29); N 7.71 (7.22)

5.3.2. Synthesis of $[Ru(S_2CNMeHex)_3]$ [1a]

Similar procedure as in 5.3.1 was used for the preparation of this complex the n-methylhexylamine (MeHexNH) was used instead of the Et_2NH. The reagents were measured up as follows:

$RuCl_3.nH_2O$ (3.00 g; 14.46 mmol), NaOH (1.74g; 43.38 mmol), CS_2 (2.61 mL; 43.38 mmol) and MeHexNH (6.58 mL; 43.38 mmol). After the completion of the reaction a black pasty precipitate was obtained after overnight refrigeration. The volume was

reduced and recrystallization attempts were made using hexane and dichloromethane and other organic solvents without success.

CHN: Calc (Found): C 42.77 (20.60); H 7.18 (3.60); N 6.23 (2.72).

5.3.3. Synthesis of $[Rh(S_2CNEt_2)_2]$[4a-c, 5, 6]

CS_2 (0.56 mL; 9.32 mmol) was added into a cold (0 °C) 50 mL MeOH solution of NaOH (0.373g; 9.32 mmol) and Et_2NH (0.96mL; 9.32 mmol) with constant stirring. The yellow $Na(S_2CNEt_2)$ salt solution was slowly reacted with the 50 mL MeOH solution $RhCl_3.nH_2O$ (0.65 g; 3.11 mmol) at 0 °C. An orange precipitate readily evolved in reaction. The orange powdery precipitate was filtered after overnight refrigeration. It was then washed with MeOH, hexane and then dried in air.

Yield: 0.22 g; 0.55 mmol; 30.90 %; mp 256 °C

CHN Calc (found): C 30.07 (30.45); H 5.05 (5.08); 7.01 (6.91)

5.3.4. Synthesis of $[Rh(S_2CNMeHex)_3]$[4a,5]

Standard literature procedure was followed as in the above procedure in 5.3.5. The reagents were used as follows: CS_2 (0.86 mL; 14.34 mmol), NaOH (0.57 g; 14.34 mmol), MeHexNH (2.17 mL; 14.34 mmol) and $RhCl_3.nH_2O$ (1g; 4.78 mmol). The resultant pasty deep orange product was reduced and washed with MeOH followed with hexane and evaporated in air.

CHN Calc (found): C 42.77 (41.45); H 7.18 (6.89); N 6.23 (5.84)

5.3.5. Synthesis of $[Rh_3(S_2CN^iPr_2)_3Cl_6]$[4a,5]

Method 5.3.5 was used for this preparation. The reagents were measured as follows: $RhCl_3.nH_2O$ (0.5 g; 2.39 mmol), NaOH (0.29 g; 7.17 mmol), CS_2 (0.43 mL; 7.17 mmol) and $^iPr_2NH$ (1.01 mL; 7.17 mmol). The orange solution was refrigerated overnight and filtered, washed with MeOH followed with hexane. The pale orange precipitate was dried in air. The resultant product seemed to be contaminated with the free ligand ions. This effect lowered the percentages from the expected value.

Yield: 0.11 g

CHN Calc (found): C 24.01 (21.97); H 4.03 (3.77); 4.00 (1.96)

5.4. Synthesis of nanoparticles

5.4.1. Synthesis of RuS_2 at 300°C

1 g of $[Ru(S_2CNEt_2)_3]$ was dispersed in 10 mL TOP and stirred for 24 hrs. The TOP-precursor mixture was then injected into pre-heated TOPO solution (10 g) at 300 °C in a three necked flask. The dark brown solution slowly turned black on continued heating maintained at 300 °C. 2 mL fractions of the reaction mixture were extracted at 90 and 120 minute time intervals. After 2 hours the reaction was stopped; the solution was then cooled to 70 °C and excess methanol was added. The black precipitate dissolved on addition of methanol.

5.4.2. Synthesis of RuS_2 at 280 °C

A similar method to the one above in 5.4.1 was used with the TOPO substituted with HDA as the capping agent.

Precursor	$[Ru(S_2CNEt_2)_3]$
Precursor amount	0.5 g
Temperature	280°C
Capping agent	HDA (5 g)
Duration	2 hours

After the heating was maintained at 280°C for 2 hours, the reaction was stopped and cooled to 70 °C. A black sticky mixture was obtained and excess methanol was added, centrifugation was done to separate the particles from the by-products. The product was then redispersed in toluene and further analysis was conducted.

5.4.3. Synthesis of RuS_2 at 250 °C

Similar method as above in 5.4.1 was used. TOPO was employed as the capping agent for the nanoparticles.

Precursor	$[Ru(S_2CNEt_2)_3]$
Precursor amount	0.5 g
Temperature	250°C
Capping agent	TOPO (10 g)
Duration	90 min

After the heating was maintained at 250°C for 1½ hours, the reaction was stopped and cooled to 70 °C. A black sticky mixture was obtained and excess methanol was added, centrifugation was done to separate the particles from the by-products.

5.4.4. Synthesis of Rh_2S_3 at 350 °C

0.5 g of $[Rh(S_2CNEt_2)_3]$ was dissolved in 10 mL TOP. The precursor solution was injected into hot TOPO (350 °C). The mixture turned deep orange on injecting, but slowly turned dark brown on continued heating at 350 °C. 2 mL fractions of the solutions were extracted after 90 and 120 minutes of the reaction time. After cooling the mixture to 70 °C, after 2 hours excess methanol was added to the reaction mixture. The mixture dissolved in methanol and centrifugation left only mere traces of the precipitate. The spectra were then conducted in methanol.

5.4.5. Synthesis of Rh_2S_3 at 280 °C

A method similar to that above in 5.4.4 was used, with the capping agent varied.

Precursor	$[Rh(S_2CNEt_2)_2]$
Precursor amount	0.5 g
Temperature	280°C
Capping agent	HDA (5 g)
Duration	2 hours

The orange solution was cooled to 70 °C and excess methanol was added. Centrifugation was done to obtain the orange powdery solid, which was redispersed in toluene and further analysis was conducted.

5.5. Deposition of thin films by Aerosol Assisted Chemical Vapour Deposition (AACVD)

5.5.1. Deposition of RuS_2 at 350 °C

0.2 g of $[Ru(S_2CNEt_2)_3]$ was dissolved in 20 mL toluene in a two-neck round bottom flask. Eight glass substrates (1 x 2.5 cm) were placed in a reactor tube. The tube was then inserted into the furnace and connected with the flask containing the precursor solution. The flask was placed into the water bath above ultrasonic humidifier, where the precursor aerosol was generated. The aerosol was then transferred by the carrier gas (nitrogen) carefully controlled at 200 mL/min using a Platon gauge, into the heated zone. The precursor then subsequently underwent thermally induced reactions (decomposition) leading to the deposition of the thin film on the glass substrate. The reaction was allowed to proceed for 2 hours with the temperature maintained at 350°C. A black shiny film was obtained in low yield. The substrates at both ends of the tube had the minimum growth.

5.5.2. Deposition of RuS_2 at 450 °C

A similar setup as in 5.5.1 was conducted for this preparation. The experiment was setup to the following conditions:

Precursor	$[Ru(S_2CNEt_2)_3]$
Deposition/substrate temperature	450 °C

Carrier gas	Nitrogen
Duration	2 hours
Gas flow rate	200 mL/min
Concentration	0.2 g/ 20 mL toluene

After two hours of deposition at 450 °C, a black shiny adherent thin film was obtained on the glass substrates. The yield was much higher, with more deposition observed in the middle substrates.

5.5.3. Deposition of Rh_2S_3 at 350 °C

$[Rh(S_2CNEt_2)_2]$ (0.2 g) was dissolved into 20 mL toluene in a two-neck round bottom flask. Eight glass substrates, with the dimensions of 1 x 2.5 cm, were inserted into the hot wall zone. The tube was connected with round bottom flask with the precursor solution. The flask was placed into the water bath over the ultrasonic humidifier, where the precursor aerosol was generated. A Platon gauge was used to carefully control the nitrogen carrier gas at 200 mL/min. The gas was then allowed to transfer the precursor solution into the heated zone. On entry into the hot zone the precursor then underwent thermally induced chemical reactions/decomposition leading to the deposition of the film on the glass substrates. The reaction was maintained for 2 hours at this temperature. A black shiny adherent thin film was obtained at the end of the reaction.

5.5.4. Deposition of Rh_2S_3 at 450 °C

The deposition of Rh_2S_3 was done as in reaction 5.5.3. The setup of the conditions was as follows.

Precursor	$[Rh(S_2CNEt_2)_2]$
Deposition/substrate temperature	450 °C
Carrier gas	Nitrogen
Duration	2 hours
Gas flow rate	200 mL/min
Concentration	0.2 g/ 20 mL toluene

After the duration of the reaction, black shiny thin films were obtained at high yields on the glass substrates. Further analysis was then done after cooling to room temperature.

5.6. References

1 (a) Pignolet L.H, *Inorg. Chem.*, 1974, **13**(9), 2051

(b) Duffy D.J. and Pignolet L.H., *Inorg. Chem.*, 1974, **13**(9), 2045

(c) Ratson C.L. and White A.H., *J. Chem. Soc., Dalton trans.*, 1975, 2418

(d) Palazzoto M.C., Duffy D.J., Edgar B.L., Que L. Jr. and Pignolet L.H, *J. Am. Chem. Soc.*, 1973, **95**, 4537

2 Wheeler S.H., Mattson B.M., Meisler G.L. and Pignolet L.H., *Inorg. Chem.*, **17**(2), 1978

3 Que L. Jr. and Pignolet L.H., *ibid.*, 1974, **13**, 351

4 (a) Pandey K.K., Nehete D.T. and Sharma R.B., *Polyhedron*, 1990, **9**(17), 2013

(b) Livingstone S.E., *Quart. Rev.*, 1965, **19**, 386

(c) Baird M.C., *Inorg. Chim. Acta,* 1971, **5**, 46

5 Cotton F.A. and McCleverty J.A., *Inorg. Chem.*, 1964, **3** (10), 1398

6 Bond A.M., Colton R. and Mann D.R., *Inorg. Chem.*, 1989, **28**, 54